



저작자표시-비영리-변경금지 2.0 대한민국

이용자는 아래의 조건을 따르는 경우에 한하여 자유롭게

- 이 저작물을 복제, 배포, 전송, 전시, 공연 및 방송할 수 있습니다.

다음과 같은 조건을 따라야 합니다:



저작자표시. 귀하는 원저작자를 표시하여야 합니다.



비영리. 귀하는 이 저작물을 영리 목적으로 이용할 수 없습니다.



변경금지. 귀하는 이 저작물을 개작, 변형 또는 가공할 수 없습니다.

- 귀하는, 이 저작물의 재이용이나 배포의 경우, 이 저작물에 적용된 이용허락조건을 명확하게 나타내어야 합니다.
- 저작권자로부터 별도의 허가를 받으면 이러한 조건들은 적용되지 않습니다.

저작권법에 따른 이용자의 권리는 위의 내용에 의하여 영향을 받지 않습니다.

이것은 [이용허락규약\(Legal Code\)](#)을 이해하기 쉽게 요약한 것입니다.

[Disclaimer](#)

Abstract

For the last decade, terahertz waves have been the focus of many researches to lead to a diverse range of potential applications, such as bio-medical imaging systems, security inspection systems, material analysis systems, and high-data-rate communications systems. Though many types of terahertz components have been developed, e.g., terahertz antennas, filters, guides, and detectors, realistic terahertz applications remain rare due to the lack of powerful, efficient, practically sized, inexpensive, and stable terahertz sources which would fill the “terahertz gap.” While time-domain spectroscopy (TDS) systems are the main streams of terahertz sources due to the instant spectroscopic capabilities throughout the terahertz range, vacuum electronic devices (VEDs) have also garnered interest due to their high-power capabilities resulting from the high kinetic energy of their convection electrons.

In this dissertation, 0.1 THz coupled cavities backward wave oscillator (CCBWO) is proposed and studied as preliminary research on terahertz VEDs, applying two-step LIGA as well as ultra nano CNC machining. The circuits are fabricated with less tolerance than a micron and the cold measurements are in excellent agreement with numerical simulation. All other components of the 0.1THz CCBWO system such as 12kV, 50mA electron gun, 2800gauss of PPM, 8% of band center frequency transmitting vacuum window, and -9kV depressed collector are designed, fabricated, and experimented and all the results match strongly to the design. All parts are assembled together and with the bias voltage at beam focusing electrode, desired perveance is observed in the beam test.

0.22THz staggered extended interaction oscillator is also investigated, focusing on the strong interaction even with relatively low voltage. In the half π phase shifted double grating resonator, the large fraction of the fundamental TE mode is longitudinally polarized, and it excites the intense plasma-terahertz wave coupling at the shallow

grating, which enables highly efficient RF generation at a relatively low operating voltage. A particle-in-cell (PIC) simulation predicts that the half-period phase-staggered grating resonator generates 0.22 THz wave with output power exceeding 100 W and interaction efficiency of more than 15 % at a low beam acceleration voltage of 5.2 kV.

Keywords: Terahertz, VEDs, coupled cavities, BWO, micro-fabrication, PIC simulation

Student number: 2008-30116

Contents

Abstract.....	i
List of figures.....	vi
List of tables.....	x
1 Introduction.....	1
1.1 Terahertz.....	1
1.1.1 THz gap.....	2
1.1.2 Present THz sources.....	4
1.2 Vacuum Electronic Devices (VEDs)	6
1.3 Terahertz VEDS and problems.....	10
1.4 Motivation and Goal.....	10
1.5 Outline.....	11
Bibliography.....	13
2 Experimental study of 0.1THz Coupled Cavities Backward Wave Oscillator (CCBWO)	19
2.1 Introduction.....	19
2.2 0.1THz CCBWO circuit.....	20
2.2.1 Design of 0.1THz CCBWO circuit.....	20
2.2.1.1 Eigen mode analysis.....	24
2.2.1.2 Time domain analysis.....	28
2.2.1.3 PIC numerical simulation.....	30

2.2.2	Two step LIGA fabrication.....	34
2.2.3	Ultra-Nano machining.....	36
2.2.4	Cold test of 0.1THz CCBWO circuit.....	41
2.3	Electron gun.....	44
2.3.1	Design of electron gun.....	44
2.3.2	Fabrication of electron gun.....	49
2.3.3	Beam-emission test.....	55
2.4	Periodic Permanent Magnet (PPM) focusing.....	57
2.4.1	Design of PPM.....	59
2.4.2	Fabrication of PPM.....	61
2.4.3	Measurement of PPM.....	63
2.5	Wide band width anti-reflecting vacuum window.....	65
2.5.1	Transmission analysis of pillbox window.....	67
2.5.2	Design of broadband width of 0.1THz vacuum window.....	75
2.5.3	Cold test of 0.1THz vacuum window.....	79
2.6	Depressed collector.....	81
2.6.1	Design of depressed collector.....	82
2.6.2	Fabrication of depressed collector.....	84
2.7	System assembly of 0.1THz CCBWO.....	88
2.7.1	RF test of 0.1THz CCBWO.....	95
2.8	Conclusion.....	96
	Bibliography.....	97
3	Theoretical study on 0.22 THz sheet beam staggered Extended Interaction Oscillator (sEIO)	99
3.1	Introduction.....	99

3.2	Design of 0.22THz sEIO.....	100
3.2.1	sEIO – Powerfully modified EIO.....	100
3.3	Particle-In-Cell (PIC) numerical hot test.....	105
3.4	Conclusion.....	115
	Bibliography.....	116
4	Conclusion.....	117
	List of Publications.....	118
	Korean Abstract.....	126
	Acknowledgement.....	128

List of Figures

1.1 Spectrum of electromagnetic wave and THz gap.....	3
1.2 Diagram for historical development of electromagnetic wave devices.....	4
1.3 Schematic of general vacuum electronic devices (VEDs).....	7
1.4 Radiation concepts of vacuum electron devices (VEDs).....	9
2.1 Dispersion relation of CCBWO circuit.....	21
2.2 Schematic of rectangular CCBWO circuit.....	22
2.3 Vacuum structure of CCBWO circuit using MWS code.....	23
2.4 resonant frequency against (a) cavity width, (b) cavity length, (c) cavity height, and (d) gap factor.....	24
2.5 (a) Contour of longitudinal electric field, (b) Vector distribution of electric field and (c) magnetic field.....	26
2.6 Pass band change w.r.t (a) cavity height, (b) gap period, and (c) cavity width.....	27
2.7 Resonant electric field patterns for fundamental cavity mode of coupled-cavity circuit (vacuum simulation model) at (a) 0 (2π)-mode, (b) $\pi/2$ ($3\pi/2$)-mode, (c) π (3π)-mode, and $5/8\pi$ -mode. 12 kV beam line excite the (b) $\pi/2$ (analogous $3\pi/2$, $5\pi/2$)-mode.....	29
2.8 Modeling of 0.1THz CCBWO circuit in MAGIC 3D.....	30
2.9 Simulated output power versus (a) gap length, (b) beam tunnel radius, (c) cavity length.....	31
2.10 Electron beam distribution (a) in xy space, (b) in phase space.....	32
2.11 MAGIC 3D results (a) generated frequency, (b) output power.....	33
2.12 Fabrication process of two step LIGA.....	34
2.13 2step LIGA fabricated circuit.....	35
2.14 Ultra-nano CNC machine.....	35
2.15 Three dimensional conceptual drawing of 0.1THz CCBWO circuit.....	37
2.16 Fabrication process of CCBWO circuit.....	38
2.17 0.1THz CCBWO circuit fabricated using nano CNC-machining.....	39

2.18 (a) coupler structure for cold test of 0.1THz circuit, and (b) Cold test setup.....	41
2.19 S11 measurement of 0.1THz CCBWO circuit. Green dashed line indicates FDTD simulation results, whereas the red line is S11 measurements using W-band vector network analyzer.....	42
2.20 Dispersion measurement of 0.1THz CCBWO circuit.....	43
2.21 Electron gun parameters.....	44
2.22 Final design values for BFE hat size, BFE angle, and distance between cathode and anode.....	46
2.23 Electron beam trajectory of final design, simulated by OPERA 3D.....	47
2.24 BFE vs Cathode misalignment study (a) when cathode is moved 25 μ m from axis and (b) BFE is moved 25 μ m from axis.....	48
2.25 CAD drawing of assembly of 12kV, 50mA electron gun.....	49
2.26 M-type dispenser cathode: (a) cathode with its base-structure, and (b) CAD view with sub-assemblies nomenclature.....	50
2.27 Gun envelope brazing.....	50
2.28 (a) jig design for precise welding of BFE, cathode, and anode (b) careful laser welding of cathode.....	51
2.29 Necessary positions of precise dimension measurement.....	52
2.30 Cathode and anode connection via checking by 3D microscope.....	53
2.31 BFE and cathode after laser welding.....	54
2.32 Experimental setup of E-gun activation.....	55
2.33 Result of beam emission test (a) without bias, (b) with bias 3V.....	56
2.34 Principle of PPM focusing.....	58
2.35 PPM design using EGUN and OPERA3D simulation.....	59
2.36 Electron beam trajectory in the circuit using OPERA 3D.....	60
2.37 Components of PPM.....	61
2.38 PPM brazing using the hanging jig.....	62
2.39 Brazed PPM barrel. All magnets are installed in the figure below.....	62
2.40 Experimental setup to measure the magnetic field inside the PPM barrel.....	63

2.41 Measurement of magnetic field inside PPM barrel. Red solid line indicates simulation result.....	64
2.42 (a) schematic of general pillbox vacuum window, and its cross sectional view in (b) yz plane as well as in (c) xy plane, (d) and its equivalent circuit diagram.....	69
2.43 <i>S</i> ₁₁ calculation versus wavelength for different <i>n</i> defined at (7). In the inset, we plot band gap between two dips near center wavelength and we plot the maximum return loss in the gap. The dashed red line indicates anti-reflecting baseline with -20dB return loss.....	72
2.44 <i>S</i> ₁₁ versus wavelength (a) for the parameter <i>m</i> at (6), and for δ at (7). The dashed red line denotes -20dB return loss baseline.....	73
2.45 (a) 3D modeling of 0.1THz vacuum window for FDTD simulation and (b) <i>S</i> ₂₁ numerical results when dielectric thickness is 2mm.....	77
2.46 (a) fabricated copper parts of 0.1THz window, (b), (c) fabricated alumina disk, (d) brazed 0.1THz window, (e) experimental setup of 0.1THz window coldtest.....	78
2.47 Measurement of <i>S</i> ₁₁ parameter. FDTD simulation and equivalent circuit results are compared.....	80
2.48 Cold test measurement of 0.1 THz CCBWO circuit with and without window...80	
2.49 Circuit diagram of (a) general collector (b) depressed collector.....	82
2.50 (a) electron tracking simulation using EGUN, (b)CST particle studio, and (b) thermal analysis of -9kV depressed collector. Second plot in (a) represents secondary emission.....	83
2.51 Mechanical design of -9kV depressed collector.....	84
2.52 Fabricated parts of depressed collector.....	85
2.53 Brazing step of -9kV depressed collector.....	86
2.54 Completely brazed depressed collector.....	87
2.55 Total assembly of 0.1THz CCBWO system.....	88
2.56 Assembly of Circuit and PPM barrel.....	89
2.57 Circuit and anode assembly.....	90
2.58 Circuit and window assembly.....	91
2.59 Electron gun and circuit assembly.....	92

2.60	Circuit and depressed collector assembly.....	93
2.61	CCBWO body and ion pump connection.....	94
2.62	Complete assembly of 0.1THz CCBWO.....	95
2.63	Experimental setup for RF test	95
3.1	Schematic side view of (a) the sEIO and (b) a conventional EIO, and the Laddertron and a comparison of the vacuum regions of (c) the sEIO and (d) the Laddertron...	102
3.2	2D vector distribution of the E-field of the (a) Laddertron and (b) the sEIO, and 2D scalar distributions of E_z for the (c) the Laddertron, (d) the sEIO.....	104
3.3	(a) Dispersion diagram of the sEIO and (b) discrete dispersions at first three orders. The inset denotes the frequency difference between each mode with respect to the number of periods.....	109
3.4	(a) Beam lines and dispersion relation at $N = 9$ and 17 to sync at the zeroth order mode of the sEIO, and (b) the subsequent available voltage range with respect to the number of gaps N	110
3.5	Output power and interaction efficiency of the 0.22 THz sEIO with respect to (a) the number of gaps N , (b) the beam acceleration voltage.....	111
3.6	(a) the phase spaces: Z vs X (top), energy vs X (middle), Y vs X (bottom), and (b) FFT results at $N=17$, $V=5.2$ kV analyzed using PIC code MAGIC 3D.....	112
3.7	Parametric analysis of the output power and interaction efficiency of the 0.22THz sEIO with respect to (a) the beam current and (b) the external Q factor.....	113
3.8	Electron beam and THz coupling of the finalized 0.22 THz sEIO as obtained from the MAGIC 3D simulation: (a) phase space of Z vs X (top), energy vs X (middle), Y vs X (bottom), and (b) field power versus time with the inset showing the FFT result.....	114

List of Tables

2.1. Finalized parameters of 0.1THz CCBWO.....	32
2.2. Cavity dimensional measurements.....	40
2.3. Calculated electron gun parameters.....	45
2.4. Parameters for 0.1THz, 0.22THz vacuum window.....	76
3.1. Dimension parameters of 0.22 THz Laddertron and sEIO in μm	104

Chapter 1

Introduction

This chapter briefly presents an overview of the research area, discusses the related motivation, goal, issues and previous studies, and the outlines accomplished investigations

1.1. Terahertz

Terahertz band is defined as the portion of the electromagnetic spectrum from 0.3THz to 10THz, i.e., the wavelength of terahertz wave is near or less than one millimeter; therefore, the terahertz band is frequently referred to as the sub millimeter wavelength band especially in the field of astronomy. The equivalent black body temperature spreads between 1.4K and 140K and it corresponds to 0.41meV to 4.1meV energy level. In this frequency range, many interesting, practical scientific behaviors are observed.

First of all, terahertz wave can penetrate wide range of materials such as plastics, semiconductors, paper, ceramics, and many other non-conducting materials that are generally opaque to visible and infrared light. This looks similar to the microwave frequency range, nonetheless, the short wavelength provides much higher resolution of imaging ability than existing microwave or millimeter wave applications [1-3]. Moreover, terahertz radiation is non-ionizing unlike X-rays so that non-harmful see through imaging is available. This is a fascinating property applicable to many bio-medical imaging systems [4-9] as well as security detection [10-13].

Another important property of terahertz wave is that molecular transition energy level is strongly related to terahertz frequency, i.e., the energy level of mode transition between rotational modes of small molecules such as water or ammonia and between vibrational modes of large molecules or weakly bound clusters are in terahertz region [14-16]. The precise measurement of molecular spectroscopy for chemical compounds in terahertz region can be used as a finger print for the specific explosives in security field [10-13] as well as for the paint pigments in art conservation science [17-21]. Above all, the major concern of the molecular response to terahertz is on water. To quote [14], Water is perhaps the most important molecular species, and certainly one of the most pervasive. Most of the samples in bio-medical experiments contain water so that many kinds of researches using strong interaction between water and terahertz such as cancer detection [22-25], hydration water near bio-molecules [26, 27] are ongoing.

Besides, the much higher frequency than present using microwave, oscillating nearly 10^{12} cycles a second, can be adoptable for high data rate future communication [28-31] and terahertz domain is also important to investigate the interstellar medium [32].

1.1.1. Terahertz gap

As seen in previous section, terahertz wave has variety of applications in many kinds of research fields. However, realization of powerful terahertz wave systems have been restricted because of, so called, terahertz gap [33]. The origin of this gap is relevant to the method how we generate electromagnetic waves. For the case of low frequency, quantitatively saying that a photon energy is negligible compared to the background energy, the free electrons in the metal are oscillated to have electro-magnetic radiation. On the other hand, in the high frequency region where a photon energy is a lot greater than circumstance noise, laser technology is generally used to have coherent radiation.

In the terahertz region, however, both technologies reach their limits, and this is terahertz gap as shown in Fig. 1.1.

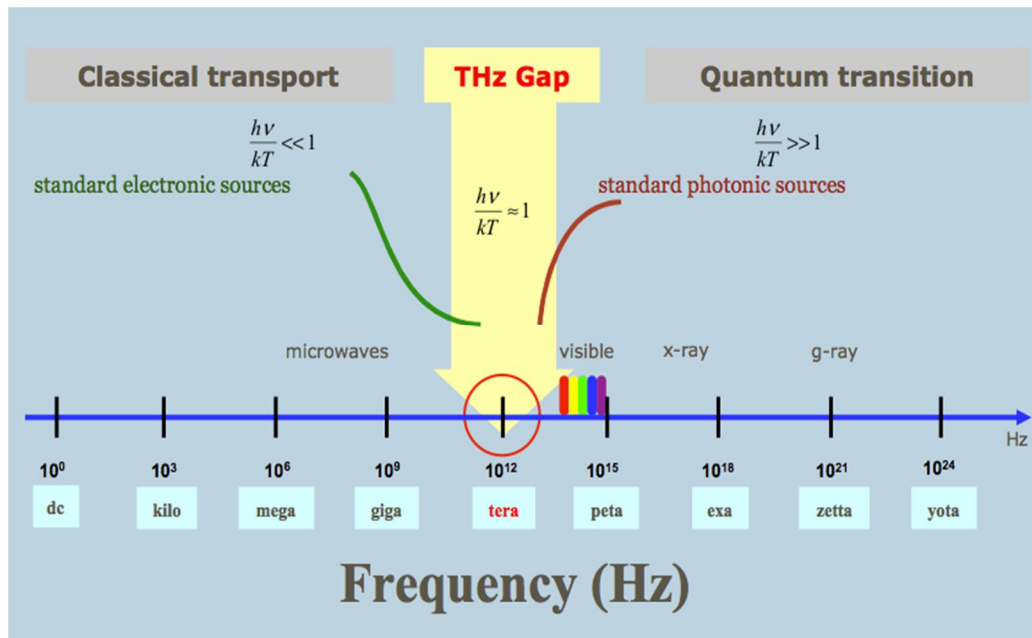


Fig. 1.1. Spectrum of electromagnetic wave and THz gap

In electronic approach, oscillating frequency is decided by the size of resonating structure and the technical limit of fabrication constraints development of high powered terahertz sources. The laser technologies using quantum transition between electron energy band also has limit because of the low photon energy of terahertz. The historical development of electromagnetic applications shown in Fig 1.2 reveals how those technical limit affects the practical applications [11].

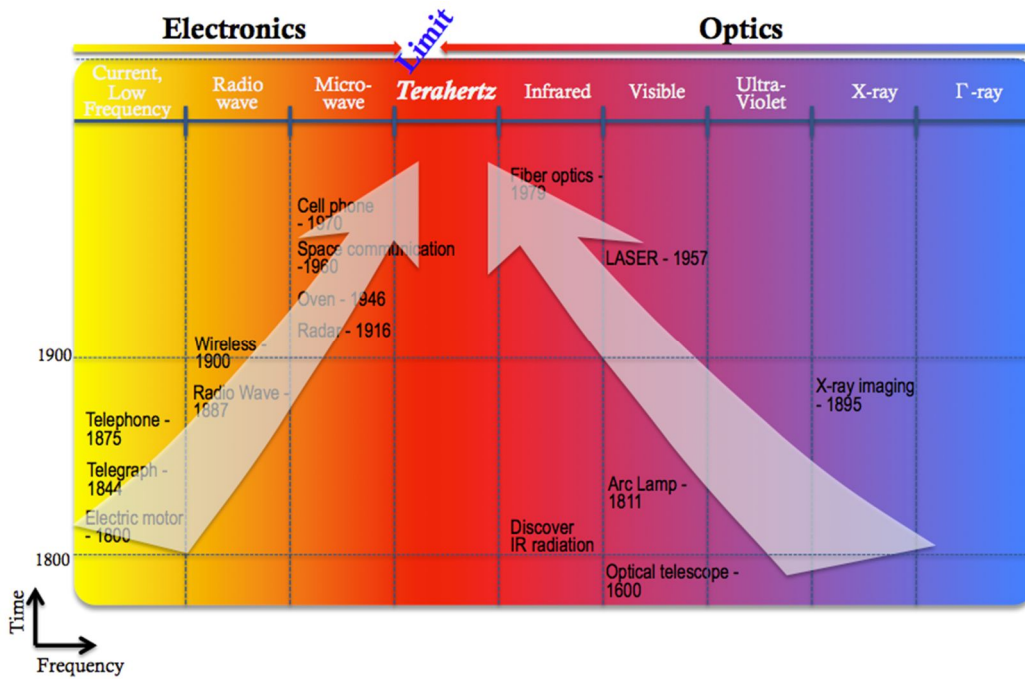


Fig. 1.2 Diagram for historical development of electromagnetic wave devices

1.1.2. Present terahertz sources

Recently, however, various research groups in different field are devoting the development of terahertz devices such as oscillation sources, detectors, filters, etc. Femto-second laser used time domain spectroscopy (TDS) systems are the most popular terahertz radiation and detection system due to the capability of instant broadband analysis. [34-37] The terahertz TDS is powerful for resonant behavior expecting researches, e.g., interaction study between molecular motion of water and terahertz. Nonetheless, the output power of the terahertz pulse is far less than a milli-watt level, so that many potential applications still need much powerful continuous wave (CW) terahertz source. Quantum cascade laser (QCL) is another optics based terahertz source.

Not like the solid state or gas laser, QCL depends on transitions between conduction energy band and valence one of semiconductor composition [39, 40]. However, much lower energy of terahertz photon than normal solid state lasers demand cryogenic circumstance to keep the tiny band structure.

In electronics devices, solid-state electronics devices are mostly under development such as diode oscillators and frequency multipliers [41-45]. These devices utilize the collisional conduction transport of free electrons in the media, i.e., in terahertz region, the low response caused by slow carriers restricts the frequency as well as the output power.

1.2. Vacuum Electronic Devices (VEDs)

Vacuum electron devices (VEDs) are strong candidate to fill the THz gap, because they are naturally born as a high power radiation source which is widely used for communications, plasma heating devices and diagnostics, radar devices, and other applications, after the Second World War. The origin of the strong output power of the VEDs is the convection electrons, which carry strong electronic energy without any collision. The schematic of general VEDs is shown at Fig. 1.3. VEDs consist of electron gun, interaction circuit, electron beam focusing magnet, collector, and vacuum window. The electron gun is the energy source of VEDs, which emits the electrons with desired energy, shape, and density. High voltage power supply is always necessary to make high kinetic energy of convection electrons. The interaction circuit is the key part where the electron coupled with the designed mode so that the kinetic energy of electrons transferred to electromagnetic energy with the frequency we want. The strong magnet devices suppress the electrons from making excursion by the repulsive force each other when the electrons interact with the circuit. Collector gathers the electrons to the ground not only for the safety but also for keeping them from coming back to the circuit. The electromagnetic energy generated in the interaction circuit can radiate through the vacuum window. It prevents the air from percolating in the VEDs, transmitting the electromagnetic wave through it.

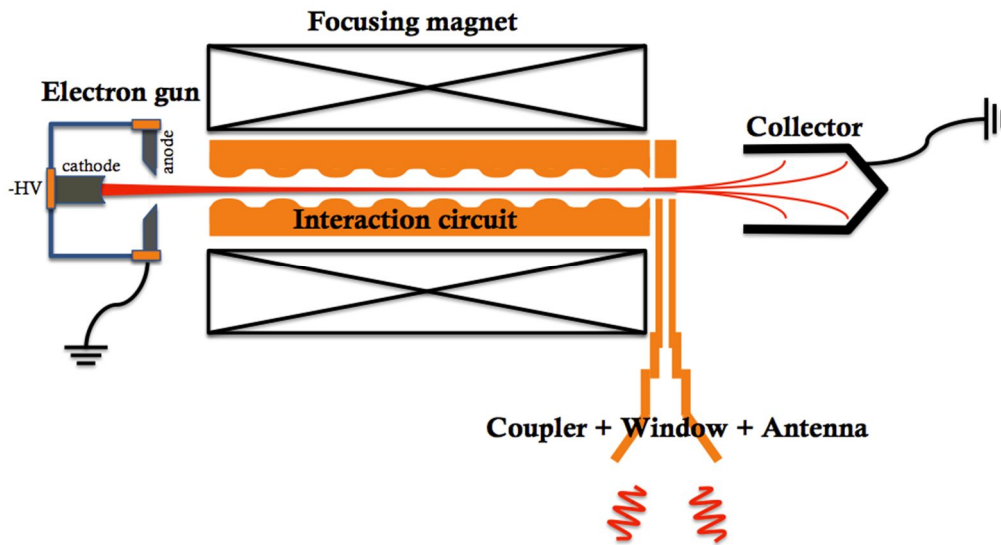


Fig. 1.3. Schematic of general vacuum electronic devices (VEDs)

In accordance to the mechanism how electro-magnetic (EM) radiation arising from high density of electrons, VEDs are classified as Bremsstrahlung radiation or Cherenkov radiation devices. The former one is produced when electrons periodically circling or wiggling in waveguide structure with the frequency synchronized to the specific waveguide modes. As depicted in dispersion relation of Fig. 1.4 cited from [46], it is termed fast-wave interaction because the synchronization point where beam line and the circuit modes tangentially meet is above the light line. Bremsstrahlung radiation applied VEDs such as gyrotrons and free electron lasers generally are promising high power even compared to other VEDs as well as those are frequency unlimited if strong magnetic field is applied [47-51]. Nevertheless, their bulky size and the astronomical costs are big minus considering the wavelength of the radiation is less than a millimeter, generally nearly a hundred micrometer.

On the contrary, for the case of Cherenkov radiation, EM radiation occurs when charged particles are faster than the EM wave in the media. For example, relativistic electrons passing through high permittivity dielectric medium would bring coherent radiation. In reality, however, periodic conducting surfaces are used instead of real dielectric material to have effectively slow the phase velocity of the EM wave in the beam direction. Therefore, it is termed slow wave interaction and the circuit modes and the electron beam line encounter tangentially below light line in synchronizing condition. Traveling wave tube (TWT) [52, 53] and klystron [54, 55] are the representatives and these devices are more suitable than Bremsstrahlung radiation sources for high frequency applications thanks to the linear motion of electrons, which minimizes the necessary volume for the beam tunnel of the interaction circuit.

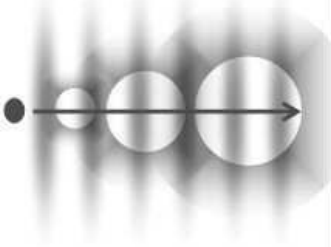
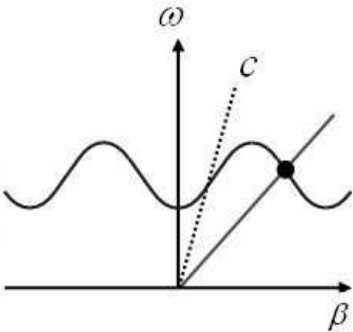
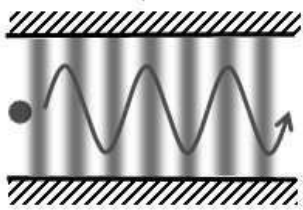
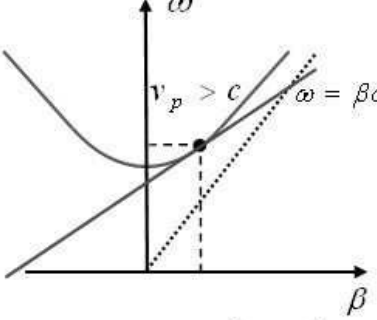
Type	Scheme	Synchronism
Cherenkov	<p data-bbox="580 450 868 488">Slow Wave Medium</p> 	 <p data-bbox="991 770 1118 808">$\omega = \beta v_b$</p>
Bremsstrahlung	<p data-bbox="635 864 804 902">Waveguide</p> 	 <p data-bbox="959 1182 1246 1272">$\omega = \beta v_z + n \left(\frac{eB_0}{\gamma m_e} \right)$</p>

Fig. 1. 4 Radiation concepts of vacuum electron devices (VEDs)

1.3. Terahertz VEDs and problems

However, we still have the fundamental size problems to achieve terahertz VEDs. Using conventional computer numeric control (CNC) machining, more than 20 μ m tolerance is inevitable even operated by good technician. Supposing less than 1% of wavelength scale is acceptable when designing interaction circuits of VEDs, manufacturing more than 0.2THz of cavity is not allowed. Practically saying, the Q factor of the cavity is less than 100 so that the electron beam and terahertz wave cannot interact each other sufficiently. The rough surface compared to the wavelength cause another critical problem. Free electrons on the cavity wall would experience much larger resistance and the short skin depth on rough surface can't keep terahertz wave reflecting perfectly. Consequently, for terahertz VEDs, scale down conversion of existing VEDs doesn't work due to the technical limit.

1.4. Motivation and Goal

To overcome the low interaction between electrons and terahertz waves, I can summarize that there are two main approaches. One is applying advanced fabrication technology, so called, "micro-fabrication", the other is focusing on other parameters such as electron beams, circuit type, etc.

Lately, many VED researching groups have been applied microfabrication technologies such as LIGA (German acronym for Lithographie, Galvanoformung Abformung; deep etch x-ray lithography, electroplating, and molding) or DRIE (Deep Reactive Ion Etching) to achieve terahertz vacuum tubes [56-61]. In our group, we have chosen to use LIGA process thanks to the high aspect ratio and we reported two step LIGA fabricated circuits since 2004 [62, 63]. Repeating the X-ray LIGA process twice, three-

dimensional formation of the beam tunnel is available. However, there have been great advance in technology of mechanical machining, either. Lately developed ultra-nano CNC machine can be operated less than a micron.

In this dissertation, I present the development of 0.1THz planer coupled cavities backward wave oscillator (CCBWO) to enhance the output power from the folded waveguide circuit. As a micro-fabrication method, I applied two-step LIGA fabrication method as well as ultra-nano CNC machining and the detail fabrication method and the results are presented. Moreover, whole system of 0.1THz CCBWO is constructed and all the experimental procedures are demonstrated.

As another try to develop compact high powered THz VEDs, staggered double grating applied extended interaction oscillator (EIO) is presented. Not like the typical EIO, fundamental TE₁₀ like field are spread along the grating surface, so that much enhanced interaction between the convection electron and the mode is demonstrated.

1.5. Outline

This dissertation includes both theoretical and experimental studies of 0.1THz coupled cavities backward wave oscillator along with the theoretical analysis on 0.22THz staggered EIO.

In chapter 2, 0.1 THz coupled cavities backward wave oscillator (CCBWO) is proposed and studied as preliminary research on terahertz VEDs, applying two-step LIGA as well as ultra nano CNC machining. The circuits are fabricated with less tolerance than a micron and the cold measurements are in excellent agreement with numerical simulation. All other components of the 0.1THz CCBWO system such as 12kV, 50mA electron gun, 2800gauss of PPM, 8% of band center frequency transmitting vacuum window, and -

9kV depressed collector are designed, fabricated, and experimented and all the results match strongly to the design. All parts are assembled together and with the bias voltage at beam focusing electrode, desired perveance is observed in the beam test.

In chapter 3, 0.22THz staggered extended interaction oscillator is investigated, focusing on the strong interaction even with relatively low voltage. In the half π phase shifted double grating resonator, the large fraction of the fundamental TE mode is longitudinally polarized, and it excites the intense plasma-terahertz wave coupling at the shallow grating, which enables highly efficient RF generation at a relatively low operating voltage. A particle-in-cell (PIC) simulation predicts that the half-period phase-staggered grating resonator generates 0.22 THz wave with output power exceeding 100 W and interaction efficiency of more than 15 % at a low beam acceleration voltage of 5.2 kV.

Bibliography

- [1] B. Ferguson, and X. Zhang, "Materials for terahertz science and technology," *Nature Materials*, vol. 1, no. 1, pp.26-33 (2002)
- [2] P. H. Siegel, "Terahertz technology," *IEEE Trans. Microwave Theory Tech.*, vol. 50, pp. 910-928, Mar. 2002.
- [3] J. C. Wiltse, "Introduction and overview of millimeter waves," in *Infrared and Millimeter Waves*, K. J. Button, Ed. New York: Academic, 1981, vol. 4, ch. 1.
- [4] P. H. Siegel, "Terahertz Technology in Biology and Medicine," *IEEE Trans. Microwave Theory Tech.*, vol. 52, no. 10, pp. 2438–2447, 2004.
- [5] T. W. Crowe, T. Globus, D. L. Woolard, and J. L. Hesler, "Terahertz sources and detectors and their application to biological sensing," *Phil. Trans. R.Soc. Lond. A*, vol. 362, no. 1815, pp. 365–377, 2004.
- [6] P. H. Bolivar, M. Nagel, F. Richter, M. Brucherseifer, H. Kurz, A. Bosserhoff, and R. Buttner, "Label-free THz sensing of genetic sequences: towards THz biochips," *Phil. Trans. R. Soc. Lond. A*, vol. 362, no. 1815, pp. 323–335, 2004.
- [7] T. Globus, D. Woolard, M. Bykhovskaia, B. Gelmont, L. Werbos, and A. Samuels, "THz-frequency spectroscopic sensing of DNA and related biological materials," *International Journal of High Speed Electronics and Systems*, vol. 13, no. 4, pp. 903–936, 2003.
- [8] M. R. Scarfi, M. Romano, R. Dipietro, O. Zeni, A. Doria, G. P. Gallerano, E. Giovenale, G. Messina, A. Lai, G. Campurra, D. Coniglio, and M. D'Arienzo, "THz Exposure of Whole Blood for the Study of Biological Effects on Human Lymphocytes," *J. Biol. Phys.*, vol. 29, pp. 171–175, 2003. 143
- [9] S. W. Smye, J. M. Chamberlain, A. J. Fitzgerald, and E. Berry, "The interaction between terahertz radiation and biological tissue," *Phys. Med. Biol.*, vol. 46, pp. R101–R112, 2001.

- [10] N. Karpowicz, H. Zhong, C. Zhang, K.-I. Lin, J.-S. Hwang, J. Xu, and X.-C. Zhang, "Compact continuous-wave subterahertz system for inspection applications," *Appl. Phys. Lett.*, vol. 86, no. 5, pp. 54 105–3, 2005.
- [11] M. K. Choi, A. Bettermann, and D. W. Van Der Weide, "Potential for detection of explosive and biological hazards with electronic terahertz systems," *Phil. Trans. R. Soc. Lond. A*, vol. 362, no. 1815, pp. 337–349, 2004.
- [12] M. C. Kemp, P. F. Taday, B. E. Cole, J. A. Cluff, A. J. Fitzgerald, and W. R. Tribe, "Security applications of terahertz technology," in *The Proceedings of SPIE Conference*, vol. 5070, August 2003, pp. 44–52. 145
- [13] D. Woolard, R. Kaul, R. Suenram, A. Hight Walker, T. Globus, and A. Samuels, "Terahertz Electronics for Chemical and Biological Warfare Agent Detection," in *IEEE MTT-S Int. Microwave Symp. Dig.*, 1999, pp. 925–928.
- [14] M. C. Nuss, "Chemistry is right for T-ray imaging," *IEEE Circuits and Devices Mag.*, vol. 12, no. 2, pp. 25-30, Mar. 1996.
- [15] T.F. Giesen, S. Brunken, M. Caris, P. Neubauer-Guenther, U. Fuchs, and F. Lewen, "Terahertz rotational spectroscopy", *Proceeding of the international Astronomical union*, vol 1, ch. S231, pp. 87-96 (2005)
- [16] S. Lee, D. Hauser, O. Lakhmanskaya, S. Spieler, E. S. Endres, K. Geistlinger, S. S. Kumar, and R. Wester, "Terahertz-visible two photon rotational spectroscopy of cold OD", *Phys. Rev. A*, vol. 93, 032513 (2016)
- [17] K. Fukunaga, Y. Ogawa, S. Hayashi, and I. Hosaka, "Terahertz Spectroscopy for art conservation," *IEICE Elec- tron. Express*, vol. 4, pp. 258-263 (2007)
- [18] K. Fukunaga, Y. Ogawa, S. Hayashi, and I. Hosaka, "Application of terahertz spectroscopy for character recog- nition in a medieval manuscript," *IEICE Electron. Express*, vol. 5, pp. 223-228 (2008)
- [19] J.-M. Manceau, A. Nevin, C. Fotakis, and S. Tzortzakis, "Terahertz time domain spectroscopy for the analysis of cultural heritage related materials," *Appl. Phys. B*, vol. 90, pp. 365-368 (2008)
- [20] W. Kohler, M. Panzner, U. Klotzbach, E. Beyer S. Winnerl, M. Helm, F. Rutz, C. Jordens, M. Koch, and H. Leitner, "Non-Destructive Investigation of Paintings with

- THz-Radiation,” 9th European Conference on Non- Destructive Testing, Sept. 2006, Berlin, Germany
- [21] Aurele J. L. Adam, Paul C. M. Planken, S. Meloni, and J. Dik, “Terahertz imaging of hidden paint layers on canvas”, *Opt. Exp.*, vol. 17, no. 5, pp. 3407-3416 (2009)
- [22] E. Pickwell, B. E. Cole, A. J. Fitzgerald, M. Pepper, and V. PWallace, “In vivo study of human skin using pulsed terahertz radiation,” *Phys. Med. Biol.*, vol. 49, pp. 1595–1607, 2004.
- [23] V. P. Wallace, A. J. Fitzgerald, S. Shankar, N. Flanagan, R. Pye, J. Cluff, and D. D. Arnone, “Terahertz pulsed imaging of basal cell carcinoma ex vivo and in vivo,” *Brit. J. Dermatol.*, vol. 151, pp. 424–432, 2004.
- [24] R. M. Woodward, V. P. Wallace, R. J. Pye, B. E. Cole, D. D. Arnone, E. H. Linfield, and M. Pepper, “Terahertz Pulse Imaging of ex vivo Basal Cell Carcinoma,” *The Journal of Investigative Dermatology*, vol. 120, no. 1, pp.72–78, January 2003.
- [25] J.-I. Nishizawa, T. Sasaki, K. Suto, T. Yamada, T. Tanabe, T. Tanno, T. Sawai, and Y. Miura, “THz imaging of nucleobases and cancerous tissue using a GaP THz-wave generator,” *Opt. Commun.*, vol. 244, no. 1-6, pp. 469–474, 2005.
- [26] H. Son, D.H. Choi, S. Jung, J. Park, and G. S. Park, “Dielectric relaxation of hydration water in the Dickerson-Drew duplex solution probed by THz spectroscopy”, *Chem. Phys. Lett.*, vol. 627, pp. 134-139 (2015)
- [27] D. H. Choi, H. Son, J. Y. Jeong, and G. S. Park, “Correlation between salt-induced change in water structure and lipid structure of multi-lamellar vesicles observed by terahertz time-domain spectroscopy”, *Chem. Phys. Lett.* vol. 659, pp. 164-168 (2016)
- [28] T. Nagatsuma, “Millimeter-Wave Photonic Technologies for Communications and Sensor Applications,” in *New Photonics Technologies for the Information Age: The Dream of Ubiquitous Services*, pp. 193–212, ed. by S. Sudo and K. Okamoto (Artech House, 2004).
- [29] C. M. Mann, “Towards Terahertz Communications Systems,” in *Terahertz Sources and Systems*, pp. 261–267, ed. by R. E. Miles, P. Harrison, and D. Lippens (Kluwer Academic Publisher, Printed in the Netherlands, 2001).

- [30] A. Hirata, H. Ishii, and T. Nagatsuma, "Design and characterization of a 120-GHz millimeter-wave antenna for integrated photonic transmitters," The Proceedings of International Topical Meeting on Microwave/Photonics, pp. 229–232, 2000.
- [31] D. Steer, G. Dolman, and P. Row, "Radio system design for broadband residential access," in IEEE Radio and Wireless Conference, Aug. 1999, pp. 31–34.
- [32] A. G. G. M. Tielens, "The molecular universe" *Rev. Mod. Phys.* 85, 1021 (2013)
- [33] C. Sirtori, "Applied physics: Bridge for the Terahertz gap," *Nature*, vol. 417, issue. 6885, pp. 132-133 (2002)
- [34] Auston, D. H., Cheung, K. P., Valdmanis, J. A. & Kleinman, D. A. Cherenkov radiation from femtosecond optical pulses in electro-optic media. *Phys. Rev. Lett.*, vol. 53, pp. 1555–1558 (1984). [35] Fattinger, Ch. & Grischkowsky, D. Point source terahertz optics. *Appl. Phys. Lett.*, vol. 53, pp. 1480–1482 (1988).
- [36] K. Kawase, J. Shikata, and I. Ito, "Terahertz wave parametric source," *J. Phys. D*, vol. 34, pp. R1–R14 (2001).
- [37] D. J. Cook, and R. M. Hochstrasser, "Intense terahertz pulses by four-wave rectification in air," *Opt. Lett.*, vol. 25, pp. 1210–1212 (2000).
- [38] Jerome Faist, Federico Capasso, Deborah L. Sivco, Carlo Sirtori, Albert L. Hutchinson, Alfred Y. Cho, "Quantum cascade laser", *science*, vol. 264, pp553-556, (1994)
- [39] B. S. Williams, H. Callebaut, S. Kumar, and J, L. Reno, "3.4 THz Quantum Cascade Laser based on Longitudinal-Optical-Phonon Scattering for Depopulation," *Appl. Phys. Lett.*, vol. 82, no.7, pp. 1015-1017 (2003).
- [40] R. Kohler, A. Tredicucci, F. Beltram, and F. Rossi, "Terahertz Semiconductor-Hetrostructure Laser," *Nature*, vol. 417, no. 6885, pp. 156-159 (2002).
- [41] H. Ito, F. Nakajima, T. Furuta, and T. Ishibashi, "Continuous THz-wave generation using antenna-integrated uni-travelling-carrier photodiodes," *Semicond. Sci. Technol.* vol. 20, pp. S191–S198 (2005).
- [42] T. W. Crowe, T.C. Grein, and P. Zimmermann, "Progress Towards Solid-State Local Oscillator at 1 THz," *IEEE Microwave and Guided Wave Letters*, vol. 6, no. 5, pp. 207-208 (1996).

- [43] H. Eisele, "Recent Advances in the Performance of InP Gunn Devices and GaAs TUNNETT diodes for the 100 – 300GHz Frequency Range and Above," *IEEE Trans. Micro. Theo. Tech.*, vol. 48, pp. 626 (2000)
- [44] D. W. Porterfield, T. W. Crowe, R. F. Bradley, and N. R. Erickson, "A High-Power Fixed-Tuned Millimeter-Wave Balanced Frequency Doubler," *IEEE Trans. Microwave Theory Techniques*, vol. 47, no. 4, pp. 149-425 (1999).
- [45] F. Maiwald, et al., "Terahertz Frequency Multiplier Chains Based on Planar Schottky Diodes," *Proc. SPIE. Soc. Opt. Eng.* 4855, 447 (2003)
- [46] Young-Min Shin, "Study on high power millimeter/submillimeter wave generation from counter-streaming electron beams in two step LIGA fabricated circuits", Ph. D Thesis, Department of Phys., Seoul Nat'l Univ. (2006)
- [47] J. L. Hirshfield and J. M. Wachtell, "Electron Cyclotron Maser," *Phys. Rev. Lett.*, vol. 12, pp. 533 (1964)
- [48] V. S. Bajaj, et al., "Dynamic Nuclear Polarization at 9 Tesla using a Novel 250GHz Gyrotron Microwave Source," *J. Magn. Resonance*, vol. 160, 85 (2003)
- [49] G. R. Neil, and L. Merminga, "Technical Approaches for High-Average-Power Free Electron Lasers," *Rev. Modern Phys.*, vol. 74, pp. 685 (2002)
- [50] P. G. O'shea and H. P. Freud, "Free-Electron Lasers: Status and Applications," *Science*, vol. 292, pp. 1853 (2001)
- [51] Y. U. Jeong, et al., "First Lasing of the KAERI Compact Far-Infrared Free-Electron Laser Driven by a Magnetron-Based Microtron," *Nucl. Inst. Meth. A*, vol. 475, pp. 4750 (2001)
- [52] P. M. Goebel, R. R. Liou, W. L. Menninger, X. Zhai, and E. A. Adler, "Development of Linear Traveling Wave Tubes for Telecommunications," *IEEE Trans. Elec. Dev.*, vol. 48, pp. 7481 (2001)
- [53] D. R. Dibb, and R. H. Le Borgue, "45GHz TWT - Recent Advances," in *Int. Vac. Elec. Conf.*, Monterey, CA., 2000
- [54] R. S. Symons, B. Arfin, R. E. Boesenberg, P. E. Ferguson, M. Kirshner, and J. R. M. Vaughn, "An Experimental Clustered Cavity Klystron," in *Int. Elec. Dev. Meeting Dig. 15* Washington D.C., 153, 1987

- [55] E. A. Gelvich, L. M. Borisov, Y. V. Zhary, A. D. Zakudayev, A. S. Pobedonostev, and V. I. Poognin, "The New Generation of High Power Multi-Beam Klystrons," IEEE Trans. Microwave Theory Tech., vol. 41, no. 15 (1993)
- [56] R. Lawrence Ives, "Microfabrication of High-Frequency Vacuum Electron Devices," IEEE Trans. Plas. Sci. vol. 32, pp. 1277 (2004)
- [57] Wolfgang Ehrfeld, Andreas Schmidt, J. Vac. Sci. Technol. B, vol. 16, no. 6, pp. 3526, (1998)
- [58] R. Ruhmann, K. Pfeiffer, M. Falenski, F. Reuther, R Engelke, and G. Grutzner, Polym. MEMS, vol. 45 (2002)
- [59] D. W. Johnson, A. Jeffries, D. W. Minsek, R. J. Hurditch, J. Photopolymer Sci. Technol., vol. 14, no. 5, pp. 689 (2001)
- [60] J. Bhardwaj, J. Ashraf, A. MacQuarrie, in Symp. Microstructures and Micro fabricated Systems, Electrochemical Soc. (1997)
- [61] G. J. O'Brien, D. J. Monk, K. Najafi, in Device and Process Technologies for MEMS and Microelectronics II, J. -C. Chiao, Ed., vol. 4592, Proc. SPIE, 315 (2001)
- [62] Seong-Tae Han, Jin-Kyu So, Kyu-Ha Jang, Young-Min Shin, Jong-Hyun Kim, Suk-Sang Chang, Ryskin, N. M., and Gun-Sik Park, IEEE Trans. Elec. Dev., vol. 52, no. 5, pp. 702 (2005)
- [63] Seong-Tae Han, Seok-Gy Jeon, Young-Min Shin, Kyu-Ha Jang, Jin-Kyu So, Jong-Hyun Kim, Suk-Sang Chang, Gun-Sik Park, IEEE Trans. Plas. Sci., vol. 33, no. 2, pp. 679 (2005)

Chapter 2

Experimental study of 0.1THz Coupled Cavities Backward Wave Oscillator (CCBWO)

2.1. Introduction

As a preliminary research on terahertz VEDs, 0.1THz CCBWO has been developed applying micro-fabrication technology, which generally stands on the basis of lithography so that precise planer layered structure is capable. Therefore, rectangular shape of cavity or waveguide like structure used circuit is chosen, i.e., we decided to use planer folded waveguide that bends periodically so that, at the middle of the structure, vertical direction of waveguides are arrayed horizontally. Folded waveguide has many advantages such as its moderate bandwidth (>10%) and high power-handling capability at higher frequencies, and simple coupling mechanism. [1-3]. Compatibility with MEMS technologies, as is already mentioned several times, which draws an attention to develop a miniaturized radiation sources in sub-terahertz and terahertz wave regions [4-6]. The interaction circuit of 0.1THz CCBWO designed here is the minor modified version of folded waveguide circuit. Instead of the natural curve at the rapid change sections, rectangular parallelepiped like structure is replaced in order to enhance the interaction strength between the electron beam and the field in the guide by adding cavity effect.

In the paper, I report not only the design of the 0.1THz CCBWO circuit but also the cold measurement of the real circuits fabricated respectively using 2 step LIGA process and using ultra-nano CNC machining.

All the other parts of 0.1THz CCBWO system, such as the electron gun that injects 12kV, 50mA, 0.36mm diameter of pencil electron beam into the circuit, beam focusing magnet, the THz window transferring wide band of THz signal to the air without significant loss, depressed collector gathering the electrons to the ground are also developed in parallel. All the engineering parts of assembling total 0.1THz CCBWO system are demonstrated in this paper.

2.2. 0.1THz CCBWO circuit

2.2.1. Design of 0.1THz CCBWO circuit

As mentioned earlier, the CCBWO circuit we have developed is kind of conversion of the folded waveguide circuit. As shown in Fig 2.2, basic structure and principle of the operation is identical to the folded waveguide one. [7] Therefore, the dispersion of the CCBWO circuit is expressed by

$$\omega^2 = \omega_c^2 + \frac{c^2}{1+hp} \left(\beta_m - \frac{2m+1}{p} \pi \right)^2 \quad (2.1)$$

where ω is the frequency multiplied by 2π , ω_c cutoff frequency, p the period of the unit circuit, m the harmonic number, β_m the wavenumber in beam passing direction, c the speed of light, and h the distance of two vertically adjacent cavities. As shown at Fig 2.1, the dispersion of the mode of the CCBWO circuit is periodically formed. Because the

adjacent gap has basically half π phase difference due to the waveguide folding, the mode frequency is maximum at $k_z = 0$. Therefore, for the backward wave interaction, the wavenumber where beam and wave synchronization occurs should be in the range between $2m\pi$ to $2(m+1)\pi$. We have chosen the 1st order of spatial harmonic $m = 1$, to avoid the burden of extremely high acceleration voltage.

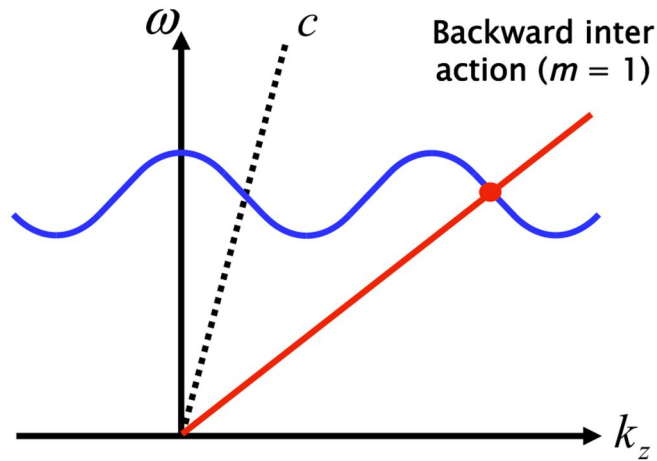


Fig. 2.1. Dispersion relation of CCBWO circuit.

As a first part of the circuit design, I set up several important parameters. At first, I determine the operation frequency band to include 0.094-0.1 THz frequency region not only because the lowest band in THz frequency range but because that frequency band is included in atmospheric window. Many researching group based on electronics are paying great attention on that frequency. The next important parameter to decide the circuit dimension is electron beams' kinetic energy, from which we know the necessary period of CCBWO circuit. In our group, we have used 12kV beam acceleration voltage, 50mA beam current emitting electron gun for a decade and 12kV is more than all right to use as our electron beam's speed because it is practically available as well as the necessary period of circuit with the beam energy is more than 0.2mm which is one of the threshold to fabricate the circuit as you will see in the

parameter calculation followed. From the beam's kinetic energy, i.e., 12kV, we can easily calculate the electron's velocity.

$$v_e = c \sqrt{1 - \frac{1}{\gamma^2}} \quad (2.2)$$

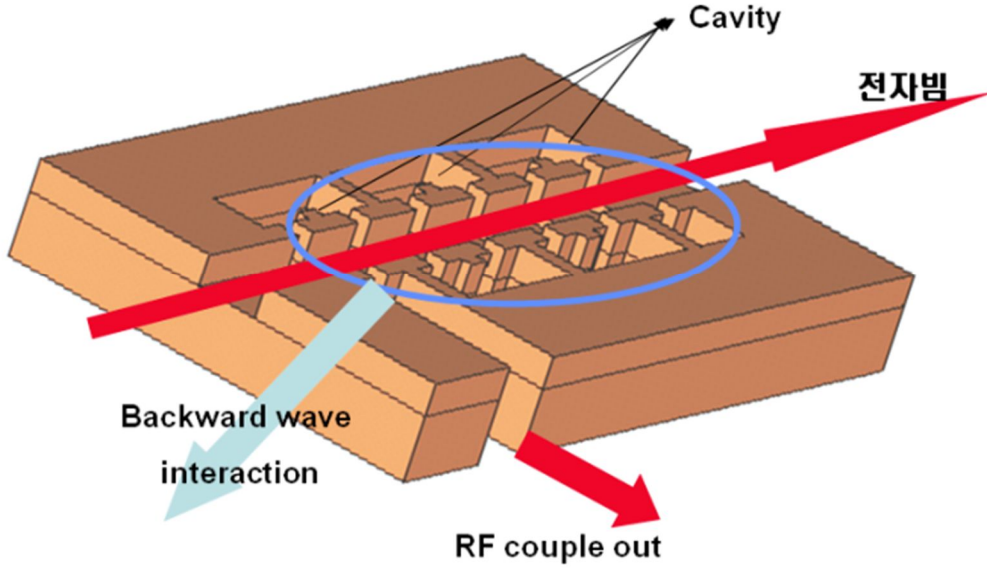


Fig. 2.2. Schematic of rectangular CCBWO circuit.

where γ is the Lorentz factor defined as $\gamma = eV / m_e c^2 + 1$. In result, $v_e = 6.385 \times 10^7$ m/s. Then the coupled wavenumber of the 0.095THz, (representative frequency among the operation frequency) should be

$$k_{z, 95GHz} = \frac{2\pi(95GHz)}{v_e} = 9.84 \times 10^3 \text{ m/s}. \quad (2.3)$$

Then, we can obtain the period of gaps in the CCBWO circuit applying the phase change in unit cell to be 2.5π , i.e., $d = 2.5\pi / k_{z, 95GHz} = 1.84$ mm. Another important parameter to be decided here is the width of the cavity. Assuming the circuit as a folded

waveguide, the width of the waveguide can be decided from the cutoff frequency of fundamental TE₁₀ mode of the rectangular guide,

$$f_{10} = \frac{c}{2a} \leq 94\text{GHz} \quad (2.4)$$

where a is the width of the coupled cavities, and $a \geq 1.59\text{mm}$.

Setting those parameters to be default, the detail design of the CCBWO circuit is achieved following 3 steps. At first, I checked the available eigen modes in the circuit by use of finite difference time domain (FDTD) simulation tool, CST Microwave Studio (MWS). [8] Changing parameters, looking for the best R over Q promising dimension is the main purpose. Secondly, adding the coupler structure at the circuit, we perform the cold test simulation starting from the dimension obtained at first step.

In the process, we can manipulate the pass band to quadrature the dispersion as required. As a final step of circuit design, we simulate the hot test using the particle in cell (PIC) simulation MAGIC 3D [9], from which we can observe the interaction between electron beam and the wave at the circuit as well as the THz generation in the circuit. An important check point of the CCBWO circuit design is the enhancement of output power comparing to previously developed folded waveguide.

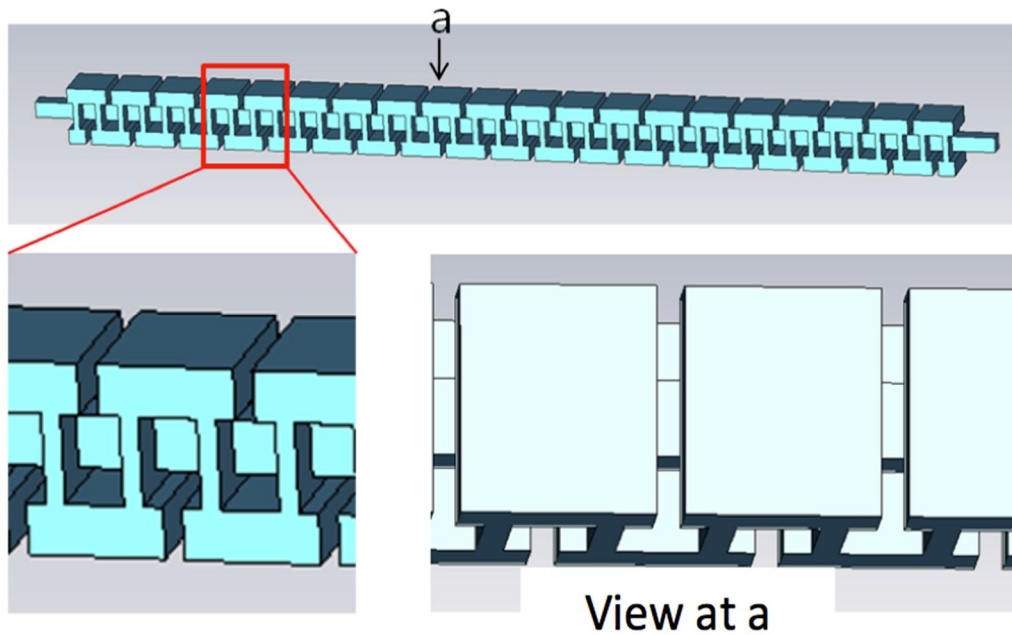


Fig. 2.3. Vacuum structure of CCBWO circuit using MWS code.

2.2.1.1. Eigen mode analysis

Changing all the parameters such as cavity size, beam tunnel size, and gap dimension, we observed the frequency as well as the R over Q. Modeling the vacuum structure of the cavity is shown in Fig. 2.3. Bounding the structure inside conducting media, closed standing wave modes are obtained. Frequency behavior against some dimensions is shown at following Fig.. The most sensitive parameter is the cavity width because the mode formed inside circuit is TE₁₀ based mode. Other parameters such as cavity height and cavity length slightly change the resonant frequency because they are related to the effective length of the periodic unit.

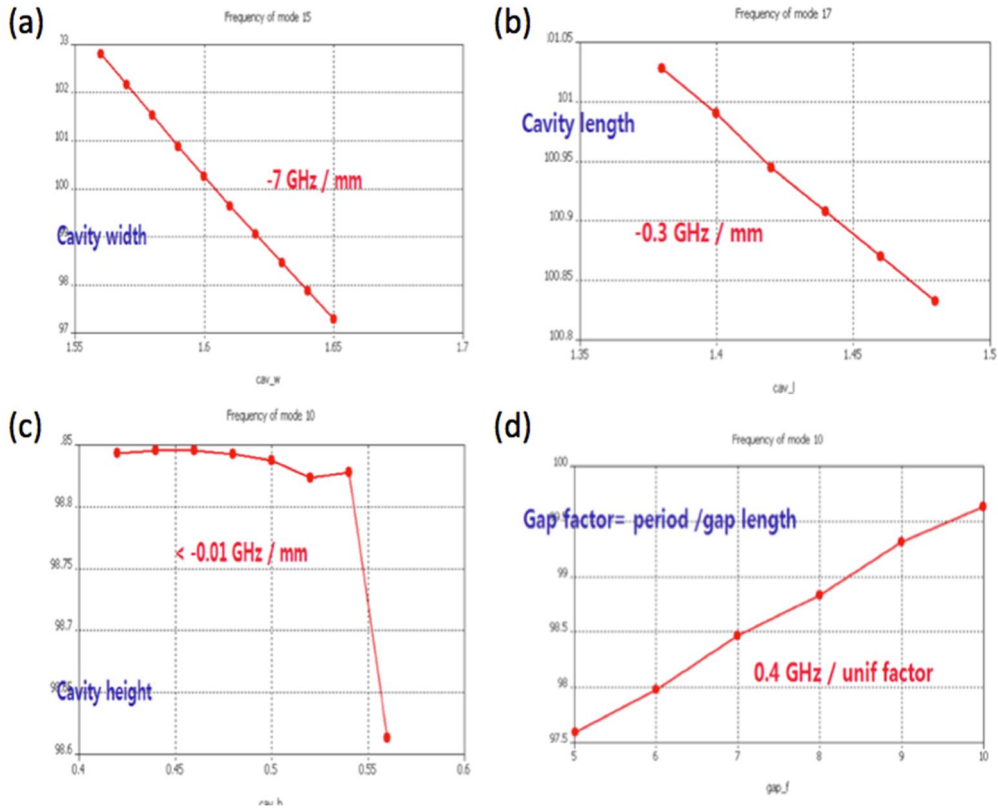


Fig. 2.4. resonant frequency against (a) cavity width, (b) cavity length, (c) cavity height, and (d) gap factor

Gap factor is defined as period over gap length and it determines that how long the electron beam interact with the circuit field when it passes a period of the circuit. It is directly related to the coupling coefficient M is written,

$$M = \frac{\int_{-\infty}^{\infty} E_z e^{i\beta_e z} dz}{\int_{-\infty}^{\infty} E_z dz} = \frac{V_{eff}}{V_1} \quad (2.5)$$

In the definition, M is equal to the convolution of the longitudinal electric field with the exponential $e^{i\beta_e z}$ (the effective voltage), divided by the voltage across the gap. The time variant term $e^{i\beta_e z}$ makes the numerator smaller as the gap length becomes longer. Therefore, the longer gap length, the smaller gap factor, and we have the smaller

coupling coefficient. Nevertheless, the gap length should be long enough to interact strongly with the electrons. Another important parameter R over Q is defined,

$$R/Q = \frac{\left(\int_{-\infty}^{\infty} |E_z| dz \right)^2}{2\omega U} = \frac{|V|^2}{2\omega U} \quad (2.6)$$

R over Q represents the coupling intensity while the electrons are passing the gap so the bigger R over Q we have, the stronger interaction between the gap field and the electrons we expect. In general, it is known that the adequate gap factor is in the range 3-4. We observed that in that range, the R over Q and coupling coefficient doesn't change drastically. The realistic effect on output power will be shown in hot test section. The field distribution of the CCBWO circuit is shown at Fig. 2.5. From the vector of the electric and magnetic field, we see that TE10 field is propagating following the folded waveguide like structure as expected.

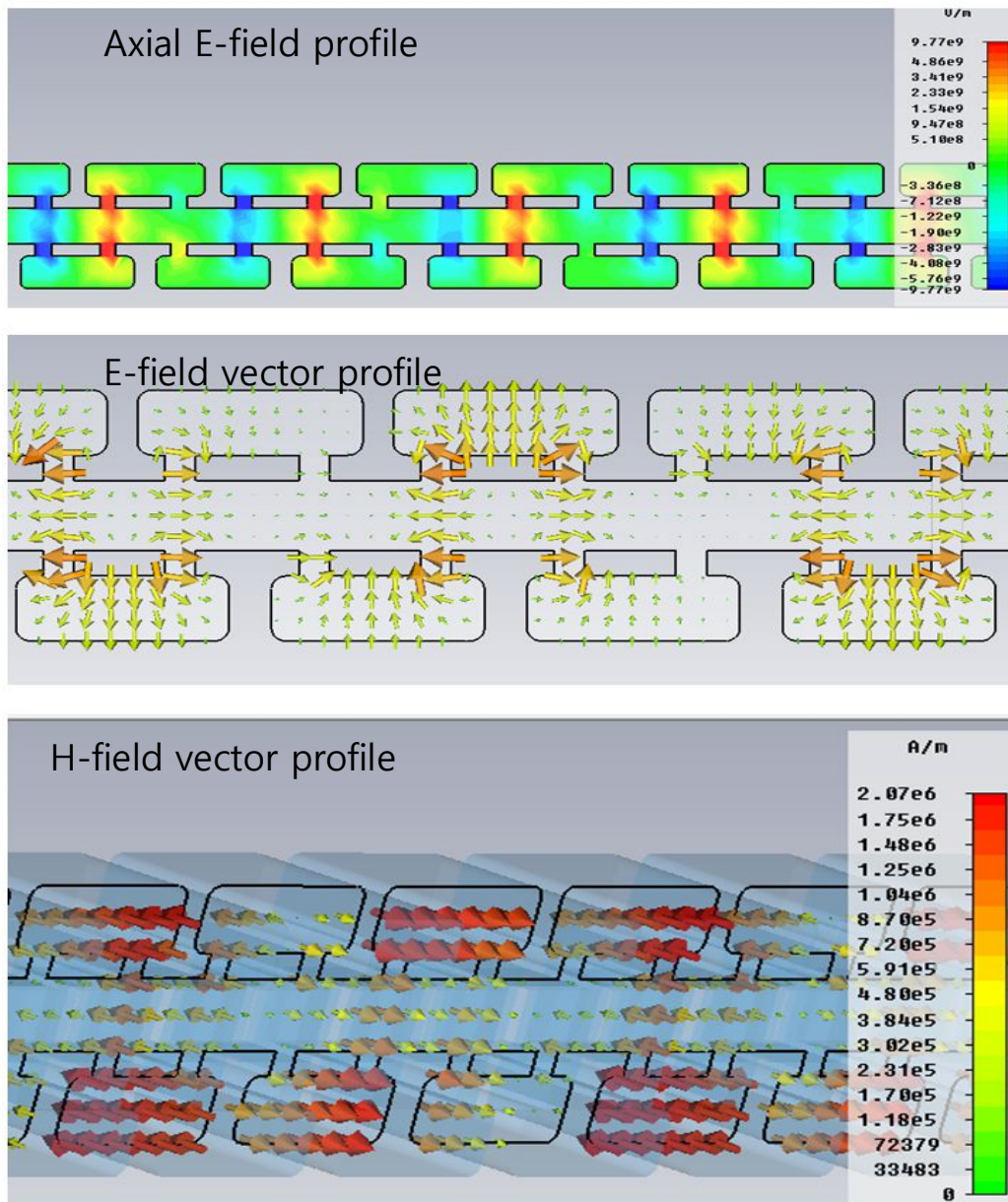


Fig. 2.5. (a) Contour of longitudinal electric field, (b) Vector distribution of electric field and (c) magnetic field.

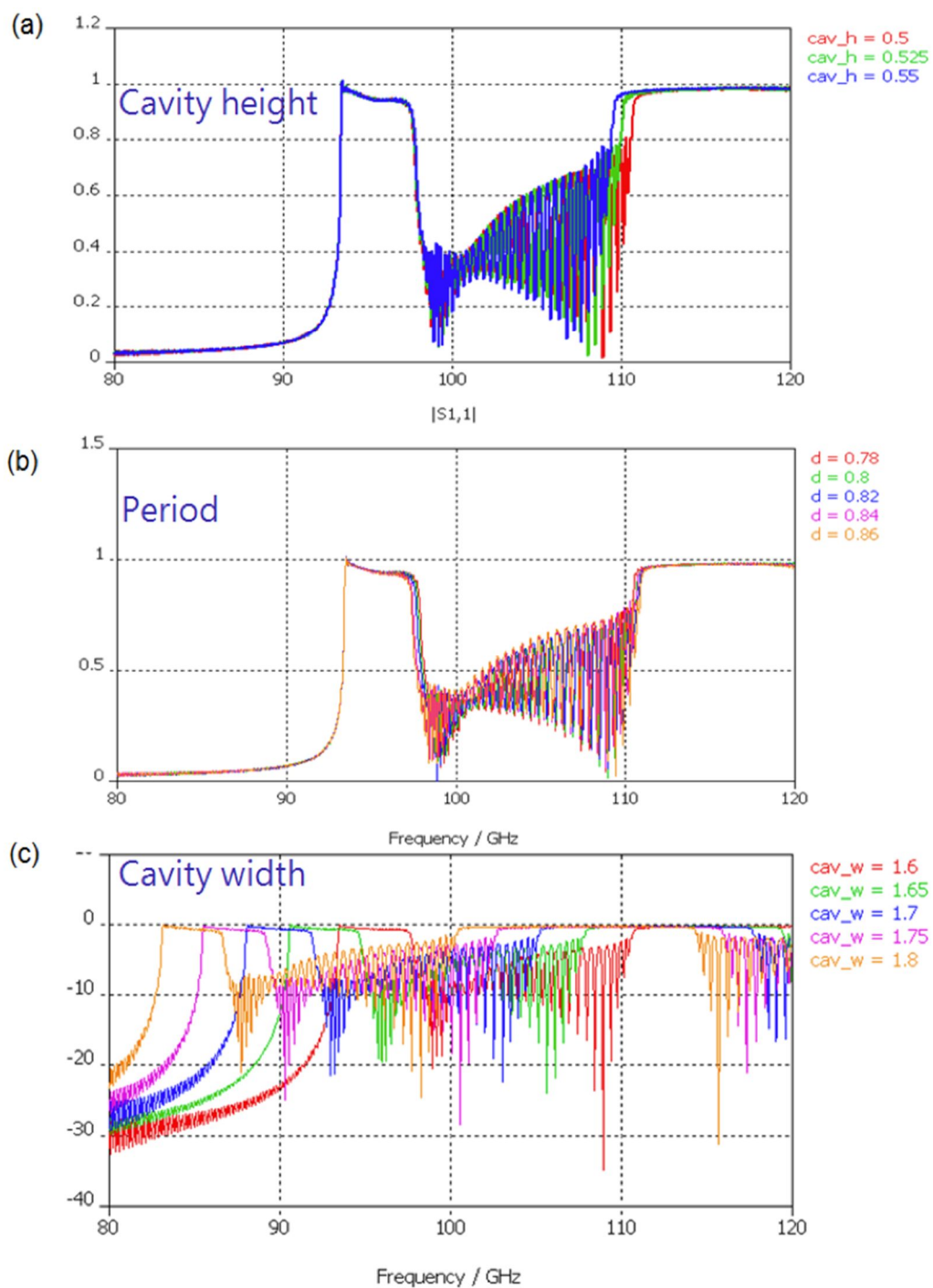


Fig. 2.6. Pass band change w.r.t (a) cavity height, (b) gap period, and (c) cavity width

2.2.1.2. Time domain analysis

Next, we added realistic coupler to the basic cavity structure to see that the right frequency of desired mode is resonant in the circuit if we inject wide frequency band including pulse through the coupler. The principle of the analysis is identical to use the vector network analyzer (VNA). In the simulation, we measure the S11 to see the response of the circuit. Fig. 2.6 shows the numerical S11 results by changing some important parameters. Pass band shrinks slightly if we increase slightly the cavity height, whereas the period doesn't affect the pass band seriously at all. As we see in the eigen mode analysis, the cavity width critically moves the pass band almost -7GHz per 0.1mm.

In the pass band, the circuit can have many different modes resulting from the phase difference between adjacent gaps, which spreads from π to 2π . Periodic number N_0 determines the number of the modes. If N_0 is infinite, we can expect that we can generate all the frequency of wave within the pass band. Fig. 2.7 shows examples of the mode in the circuit w.r.t the phase difference between the gaps.

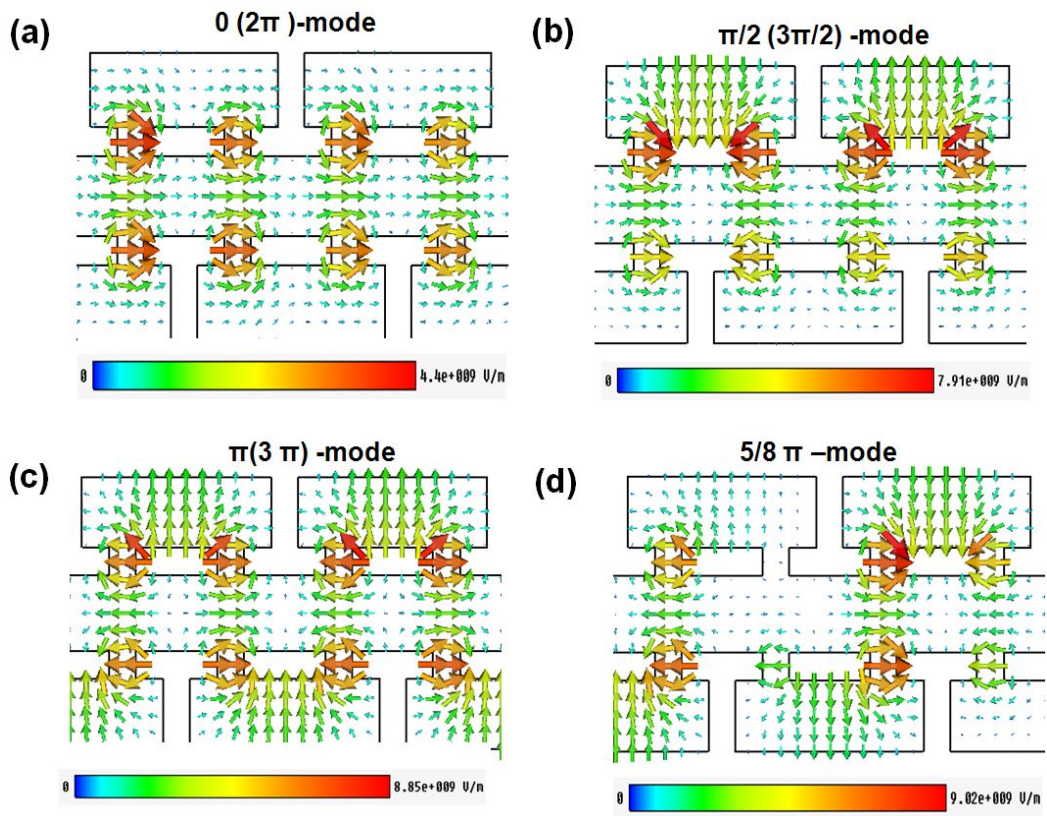


Fig. 2.7. Resonant electric field patterns for fundamental cavity mode of coupled-cavity circuit (vacuum simulation model) at (a) $0 (2\pi)$ -mode, (b) $\pi/2 (3\pi/2)$ -mode, (c) $\pi (3\pi)$ -mode, and $5/8\pi$ -mode. 12 kV beam line excite the (b) $\pi/2$ (analogous $3\pi/2, 5\pi/2$)-mode.

2.2.1.3. PIC numerical simulation

As a final step of the circuit design, we do the hot test numerically using MAGIC 3D. In the simulation, we inject the designed electron beams through the beam tunnel just like we want to do in reality. Then we check the electron and the electromagnetic wave interaction in real time even it changes in picosecond scale. If we put adequate coupling structure as show in Fig. 2.8 we can measure the output power of the designed CCBWO. Thus, the final step of the design is just directly measuring the output power w.r.t parameters.

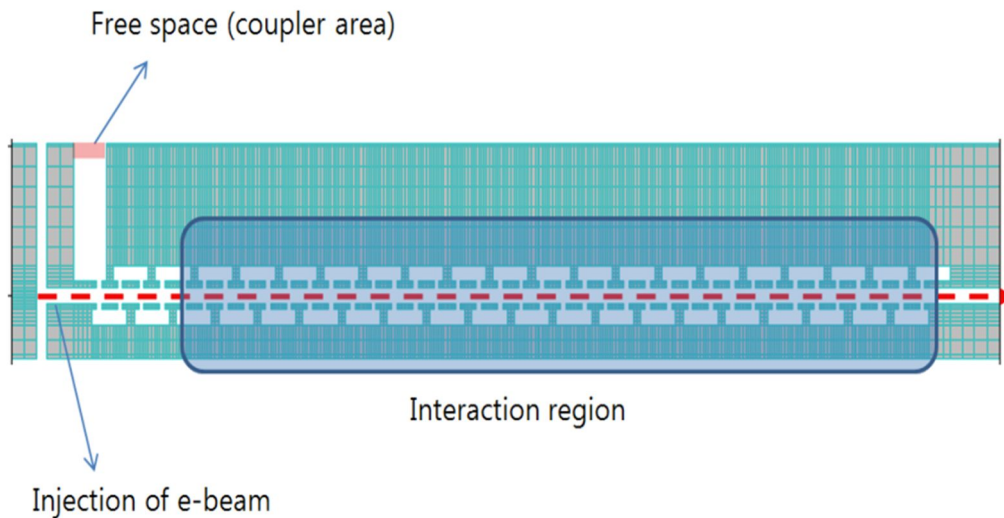


Fig. 2.8. Modeling of 0.1THz CCBWO circuit in MAGIC 3D

Although we have chosen the parameters after careful consideration, the output power changes sensitively as the parameters slightly have different values. Fig. 2.9 shows the relation between the output power and gap length, beam tunnel radius, and cavity length as examples. The injected beam in the simulation has 12kV kinetic energy and the beam current is 50mA. The simulated tolerance to keep the performance is below ± 10 micrometers.

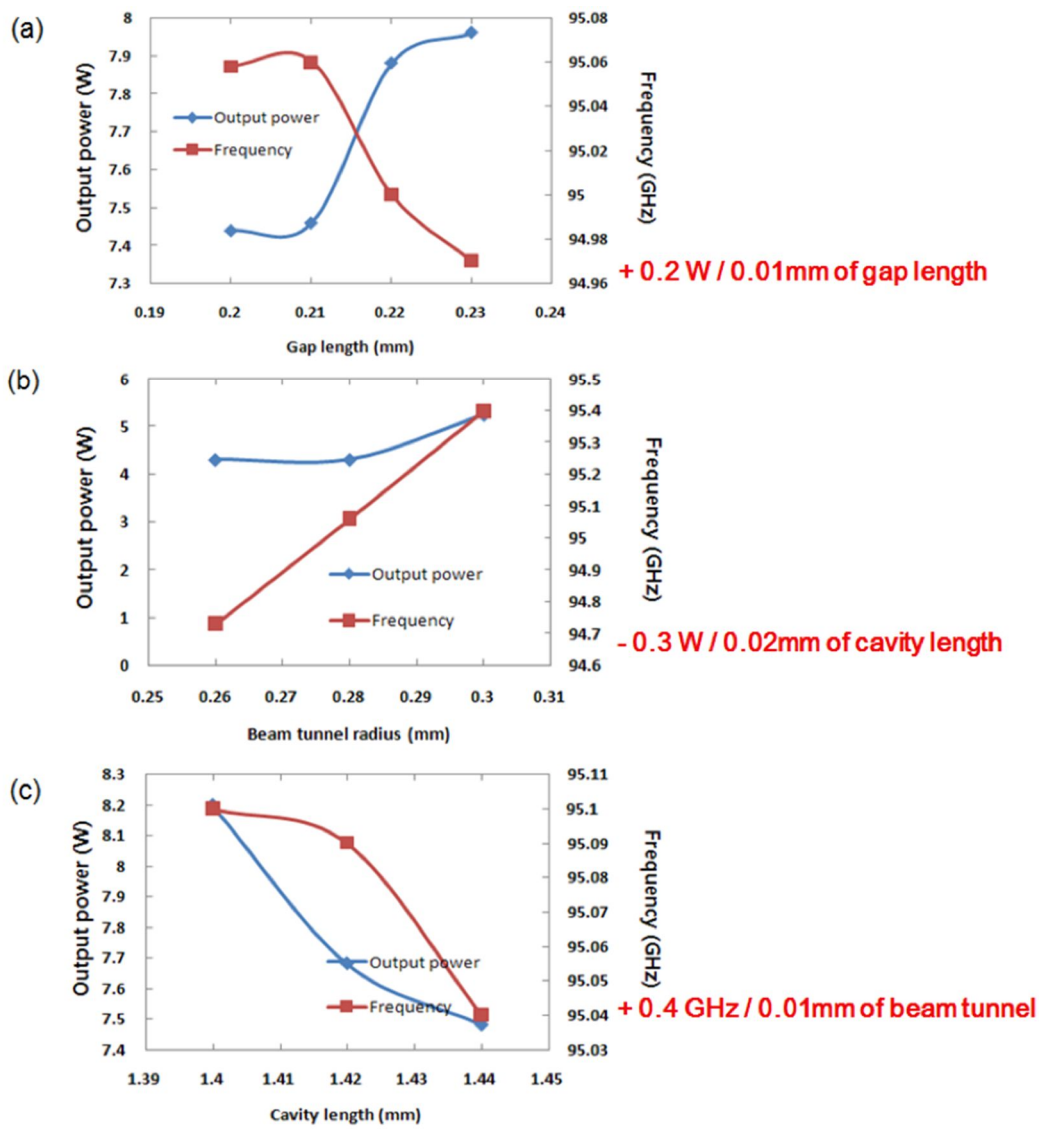


Fig. 2.9. Simulated output power versus (a) gap length, (b) beam tunnel radius, (c) cavity length

Table 2.1. Finalized parameters of 0.1THz CCBWO

Position	designed value (mm)
cavity length	1.42
gap length	0.21
period	0.84
2*period	1.68
tunnel height	0.56
cavity height	0.53
gap height	0.96
tunnel depth	0.28
cavity depth	0.84

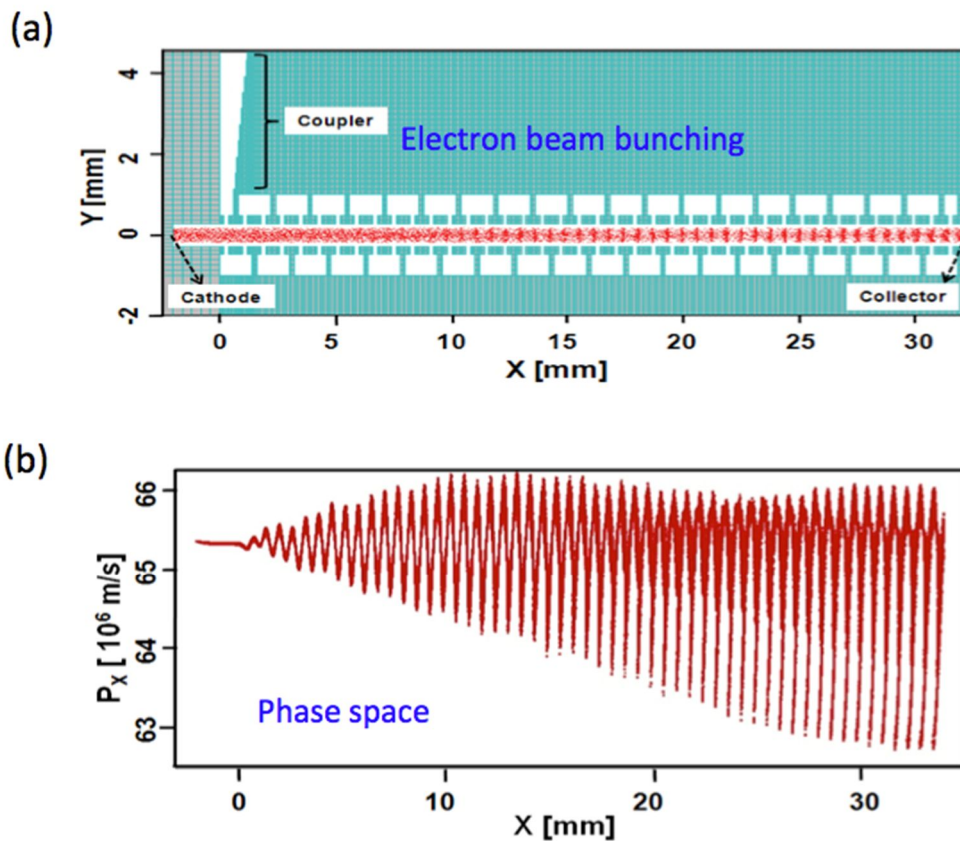


Fig. 2.10. Electron beam distribution (a) in xy space, (b) in phase space.

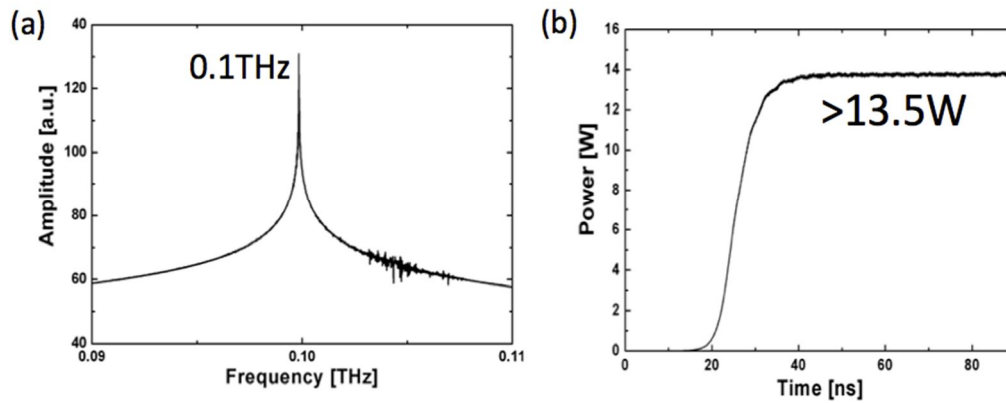


Fig. 2.11. MAGIC 3D results (a) generated frequency, (b) output power

Final optimized dimension is listed in table 2.1. With the final dimension, we observed strong beam bunching as seen in Fig. 10. As the electron beams pass through the beam tunnel, the electrons gradually gather periodically and the accumulated beams again become unfastened at the end of the beam tunnel. Fig. 10. (b) shows the beams' energy is spread about 5% in a bunched beam. The expected output power at 0.1THz is more than 13.5W, 10times higher than the output power of the 0.1THz FWBWO developed in our laboratory before. The coupled cavities strengthen the interaction between the gap field and the electrons successfully.

2.2.2. 2 step LIGA fabrication [10]

At first, we fabricate the 0.1THz CCBWO circuit using two-step LIGA process. The two-step LIGA process is repeating entire LIGA procedures such as x-ray exposure, development, electroplating, lapping, and so on, including additional alignment between the 1st and the 2nd layers. 1st layer contains coupled cavities only and the depth of the layer is same to half cavity height subtracted by half of beam tunnel height. The two-step LIGA procedure is briefly explained in Fig. 2.12

I followed the standardized procedure in Pohang Accelerator Laboratory (PAL), which is written in detail at the section 3-2 of Young-Min Shin's ph. D thesis [10]

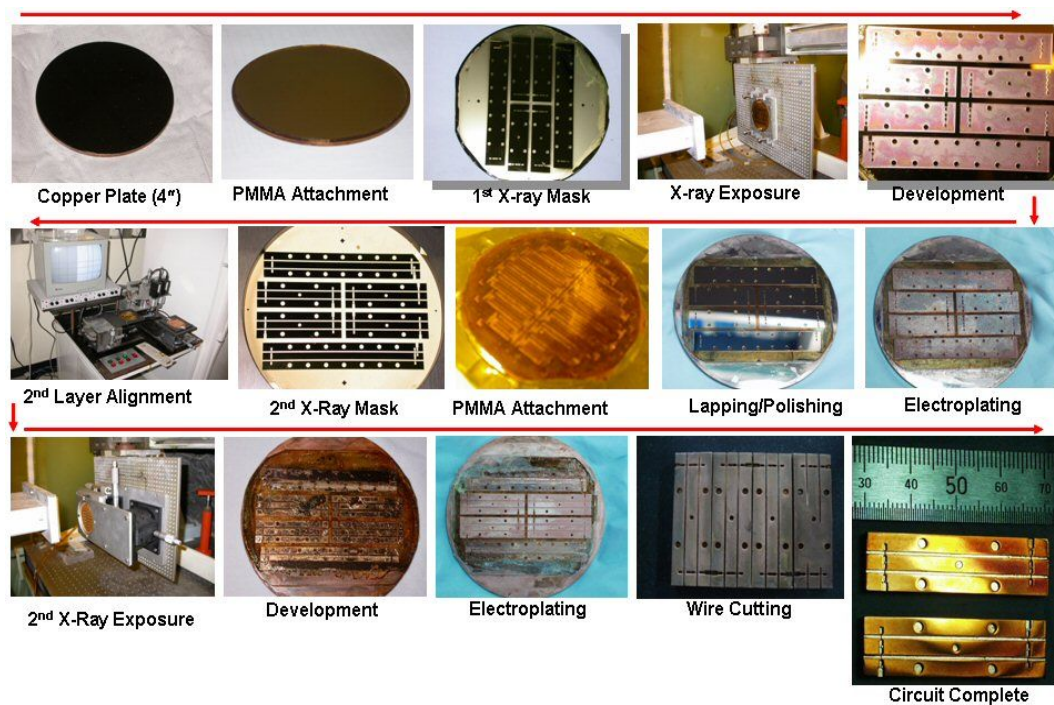


Fig. 2.12. Fabrication process of two step LIGA

The resultant photo mask and the circuit are shown at Fig. 2.13. Though it looks fancy, small defect is observed at the middle of the circuit, which would critically weaken the coupling of beam and wave. Moreover, the success rate of precise alignment of each step is less than 30% so far. Therefore, we used ultra-nano machining before the next beam line is available.

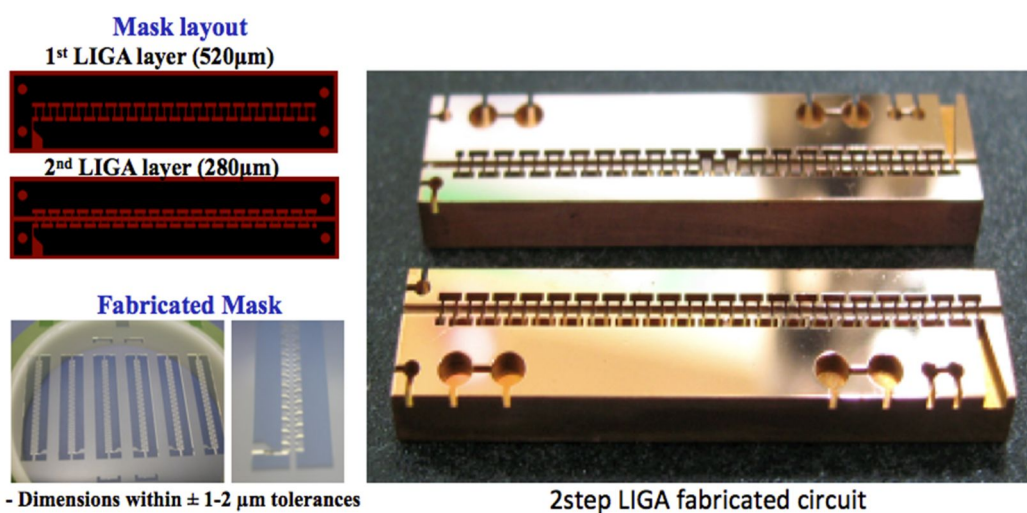


Fig. 2.13. 2step LIGA fabricated circuit.

2.2.3. Ultra-Nano machining

Ultra-nano machining is advanced technology of conventional machining. Most of the CNC milling machines can operate with at most 1-20,000 rpm. It is not enough to drill safely out small but high aspect ratio of sample like our CCBWO circuit because the necessary end mil to dig out 0.2mm width and 0.8mm depth of copper should be very thin and long thus it easily get broken while machining. The ultra-nano CNC milling machine, however, can work with much higher speed, up to 50,000 rpm so that we could minimize the number of necessary end mills, e.g., only two end mills were used making a half of the 0.1THz CCBWO circuit.

Holding and releasing the sample is another important factor to cause a big tolerance when we conventionally machined it. As the needed precision level is higher, the general holding method is not enough to maintain the sample position relative to the end mil. The ultra nano CNC milling machine use the strong magnet to fix the sample instead of simple chuck, so that the oscillation or shape conversion is minimized while operation.



Fig. 2.14. Ultra-nano CNC machine

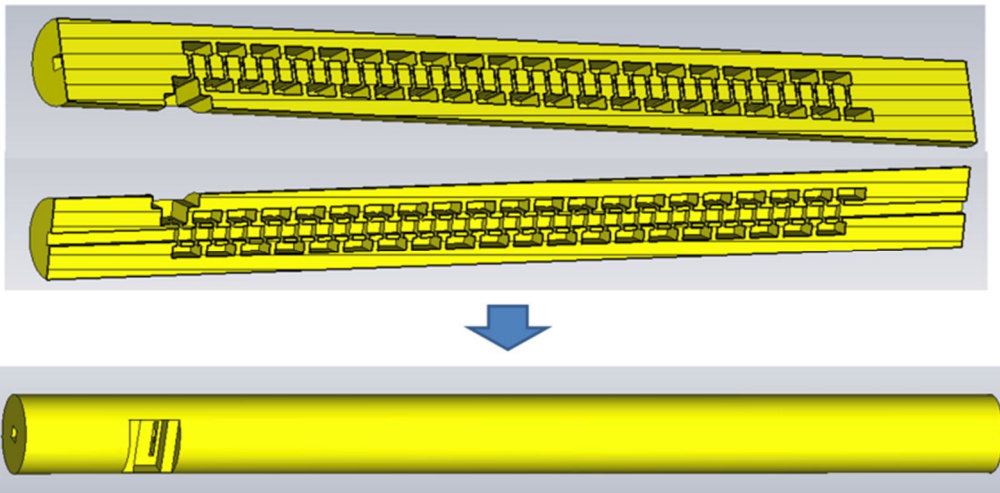
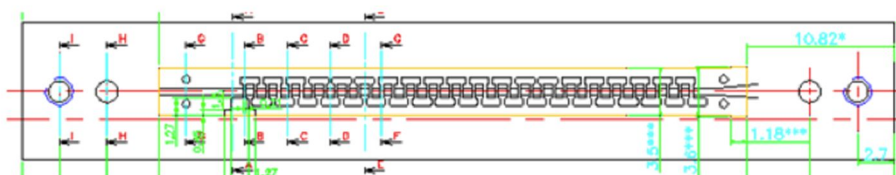


Fig. 2.15. Three dimensional conceptual drawing of 0.1THz CCBWO circuit

Considering using nano machining as the fabrication method of 0.1THz CCBWO circuit, I newly designed mechanical design of it. Manufacturing the circuit using general machining, though specialized machine is used, has strong benefit, that is, it is easy to achieve curved structure. Therefore, I adopt cylindrical body to make it easy to align with other components such as anode, collector, and especially with the outer body filled with focusing magnet. Fig2.15 denotes the conceptual design of new circuit. To accomplish the coupled cavities inside the cylindrical body, the order of the fabrication is very important. Fig. 2.16 explains briefly the fabrication process of the circuit. At first, prepare the big rectangular piece of copper and grind the surface as much as possible. Then, we make the key pattern of coupled cavities using nano-CNC milling machine, with 35000 rpm of end mil speed. Next, we combine two half circuits together using align pin and we make the circuit cylindrical body via lathe processing.

Additional defect on the surface of circuit is made by wire cutting to enlarge the vacuuming area. The ultra-nano machined 0.1THz CCBWO circuit is seen in the Fig. 2.17. The measurement in table 2.2 shows that the tolerance of the circuit is at most $1\mu\text{m}$, factor of 20 to 30 times better than the previously machined circuit by normal milling machine.

1. Patterning by milling



2. Making cylinder type by lathe process



3. Making hole for vacuuming

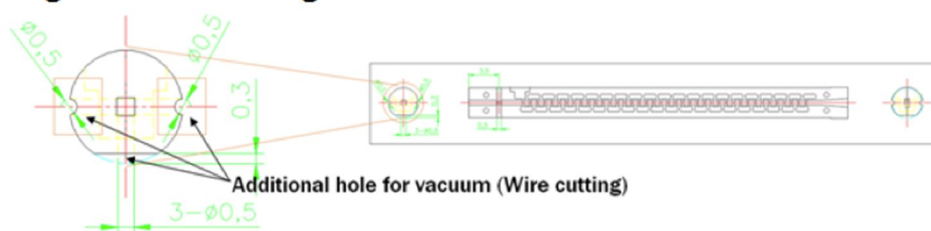


Fig. 2.16. Fabrication process of CCBWO circuit

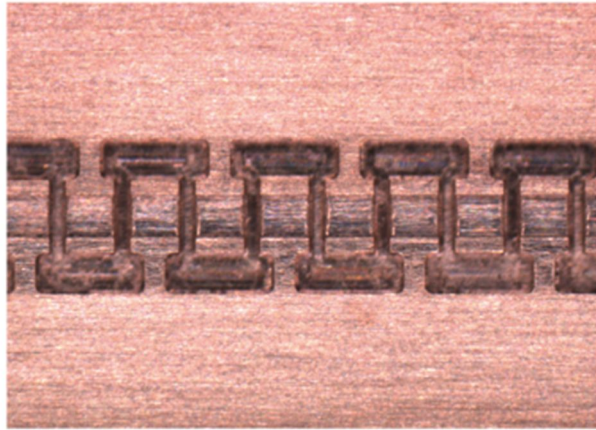
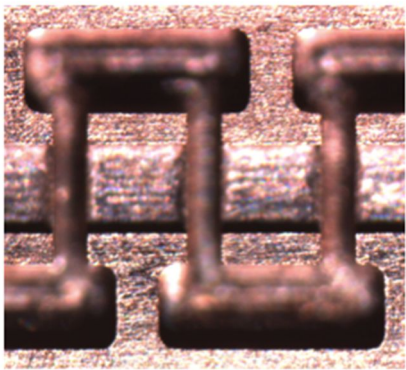
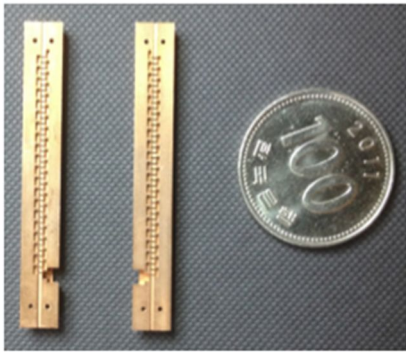


Fig. 2.17. 0.1THz CCBWO circuit fabricated using nano CNC-machining

Table 2.2. Cavity dimensional measurements

	Position	designed value (mm)	Maximum deviation (mm)
1	cavity length	1.42	0.0057
2	gap length	0.21	0.0047
3	period	0.84	0.0048
4	2*period	1.68	0.0053
5	tunnel height	0.56	0.005
6	cavity height	0.53	0.0032
7	gap height	0.96	0.0053
8	tunnel depth	0.28	0.0051
9	cavity depth	0.84	0.0099

2.2.4. Cold test of 0.1THz CCBWO circuit

I measured the S11 scattering parameter using W-band extended Vector Network Analyzer (VNA) system. I made a special waveguide to fit in the circuit coupler. One end of the guide is connected to WR-10 waveguide flange as shown in Fig. 2.18 (a) and we connect the flange directly to the port of VNA like Fig. 2.18(b).

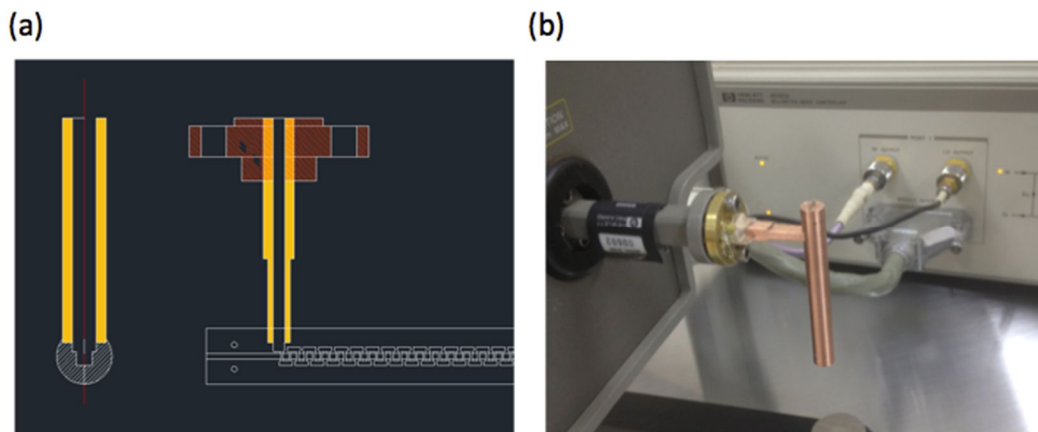


Fig. 2.18. (a) coupler structure for cold test of 0.1THz circuit, and (b) Cold test setup

Fig.2.19 denotes the S11 measurements of two circuits made in same method. We can observe the excellent agreement between FDTD simulation results and measurements. The dispersion relation obtained from the S11 measurement perfectly matches with both eigen analysis and time domain simulation.

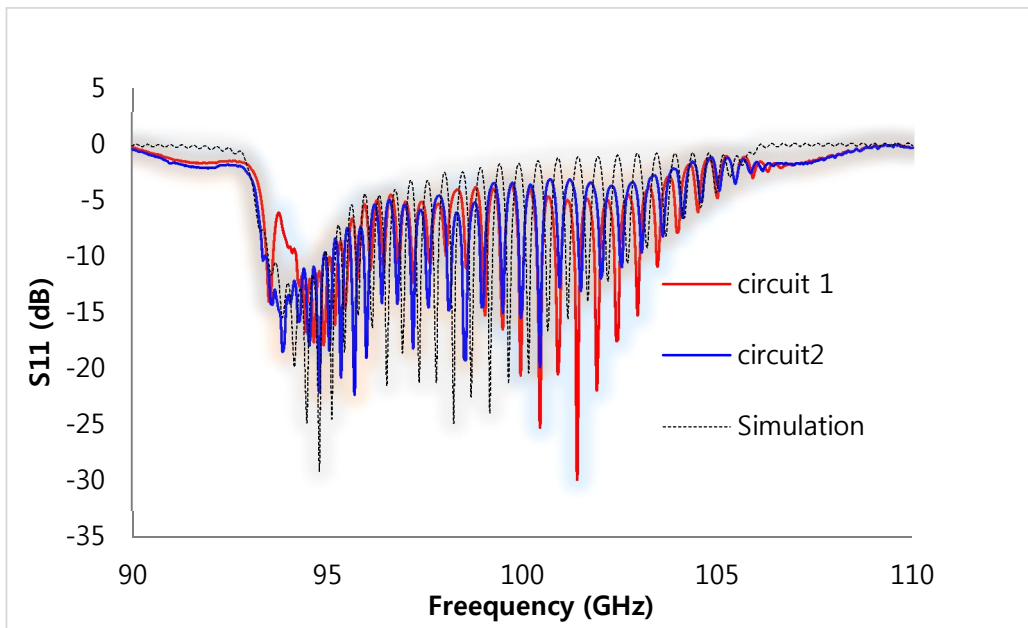


Fig. 2.19. S11 measurement of 0.1THz CCBWO circuit. Green dashed line indicates FDTD simulation results, whereas the red line is S11 measurements using W-band vector network analyzer.

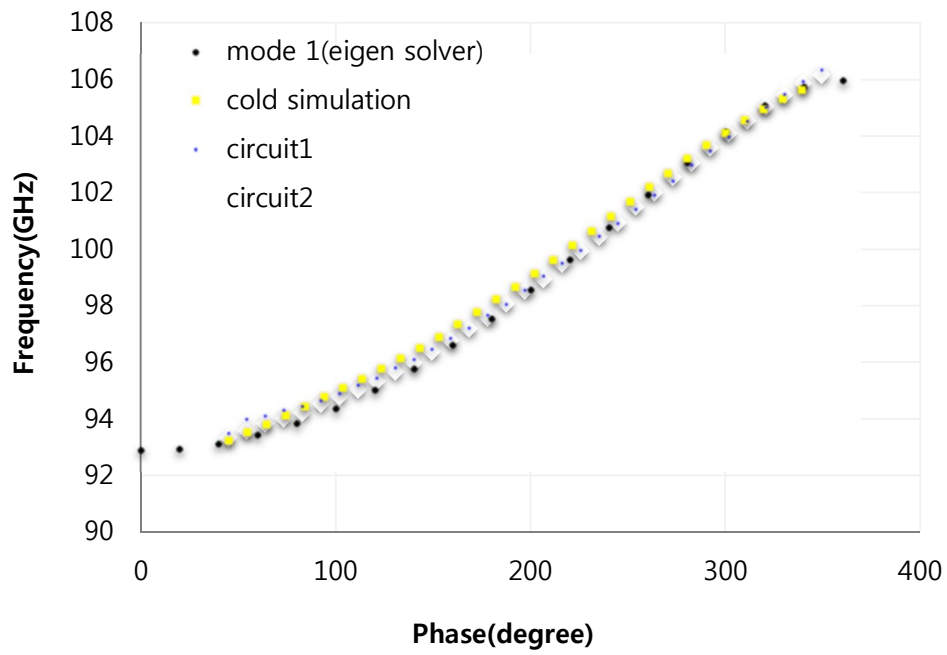


Fig. 2.20. Dispersion measurement of 0.1THz CCBWO circuit.

2.3. Electron gun

As mentioned earlier, we have used our lab's historical design of electron gun, the main specifications of which are 12kV acceleration voltage, 50mA beam current, and 0.36mm beam diameter. Because the detail design of the electron gun is well explained in previous researches, I simply present the updated design. Instead of the electric design, however, mechanical design is a lot improved. Details will be followed.

2.3.1. Design of electron gun

We followed the typical Pierce-gun for our 0.1THz CCBWO electron gun design [11]. At first, basic parameters of the electron gun are calculated following Vauhan's iteration method. Secondly, EGUN simulation is used to optimize the parameters precisely. As a final step, we validate the design by 3 dimensional tracking using OPERA 3D simulator [12].

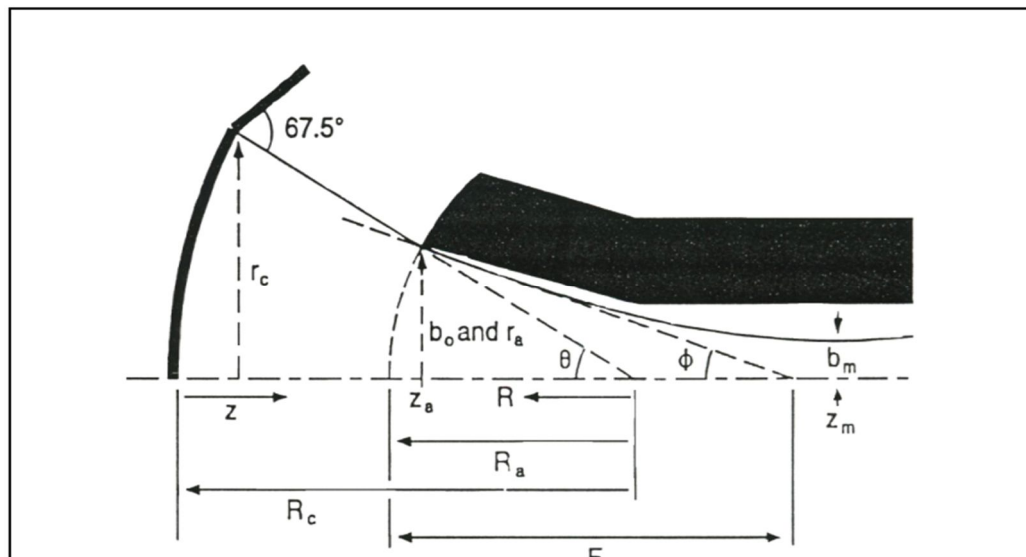


Fig. 2.21. Electron gun parameters [13]

Table 2.3. Calculated electron gun parameters.

Parameters Name	Synthesized Parameters (mm)
Cathode radius of curvature (R_c)	10.13
Anode radius of curvature (R_a)	4.27
Cathode disk radius (r_c)	0.8
Anode aperture radius (r_a)	0.4
BFE angle (Pierce magic angle)	67.5 ⁰
Cathode-to-anode aperture distance (z_a)	5.88
Beam waist position (z_m)	16.19
Beam micro-Perveance (Perv)	0.038

Fig. 2.21 is cited from [13], which indicates the design parameter to use at Vaughan approach. We've already calculated results, which are seen in table 2.3. Additional important parameters are found by OPERA 3D and they are beam focusing electrode (BFE) angle, head size of the BFE, and the distance between cathode and anode. In Fig. 2.22, the final value is found in the drawing. [14] The electron beams trajectory of finally designed electron gun is seen in Fig. 2.23. We obtained 51.99mA beam current, 18mm beam waist position, and <0.18mm beam radius when we apply -12kV at cathode.

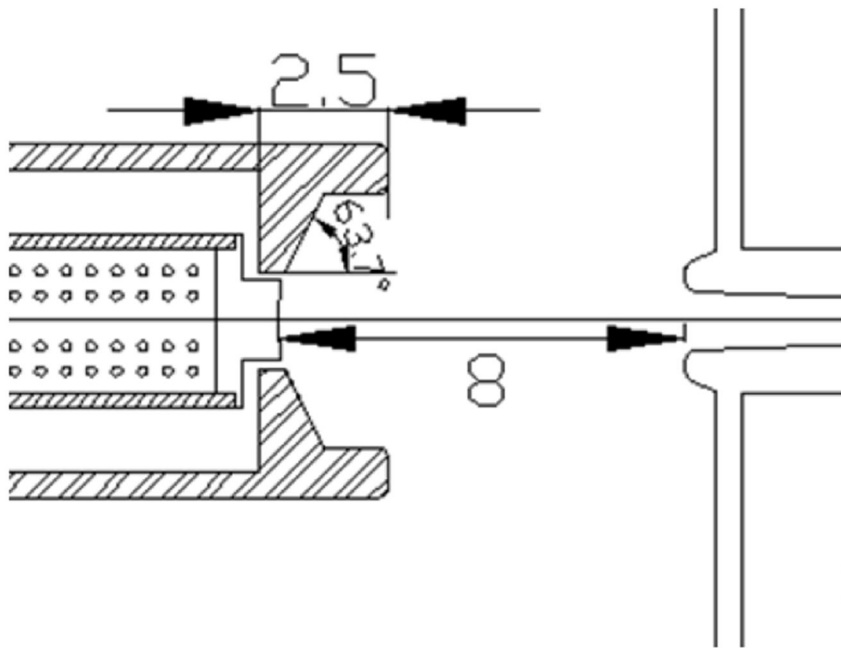


Fig. 2.22. Final design values for BFE hat size, BFE angle, and distance between cathode and anode. [14]

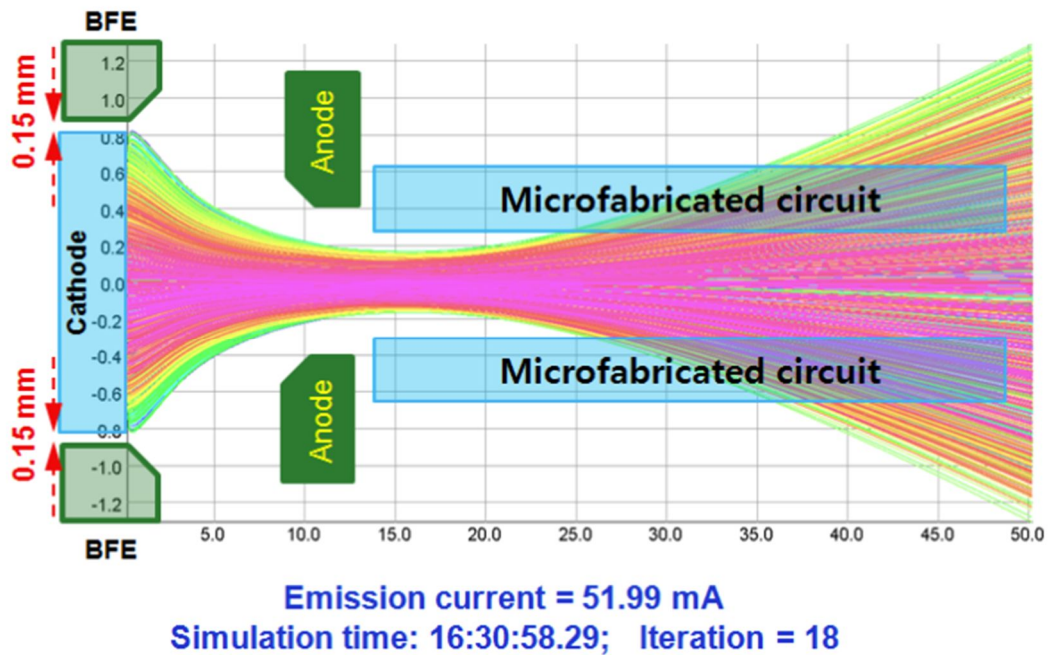


Fig. 2.23. Electron beam trajectory of final design, simulated by OPERA 3D

Until now, I just briefly summarized the design process of electron gun, by which several electron guns are made already in our lab. However, performing the electron gun fabrication several time, I found that the reproducibility is very low. Therefore, we checked the necessary tolerance of the key components of electron gun. It is obvious that the most important thing deciding the beam specification critically is the potential line between the cathode and anode. The alignment of cathode and BFE is thought to be a critical factor to get proper beam current and the trajectory. Therefore, we simulate the tracking solver of OPERA 3D, changing the position of BFE's axis slightly as shown in Fig. 2.24 (a). The other case that cathode is moved from its axis while fixing other components is also studied and it is shown at Fig. 2.24 (b). In result, 25 μ m is the maximum tolerance acceptable for the stable beam current.

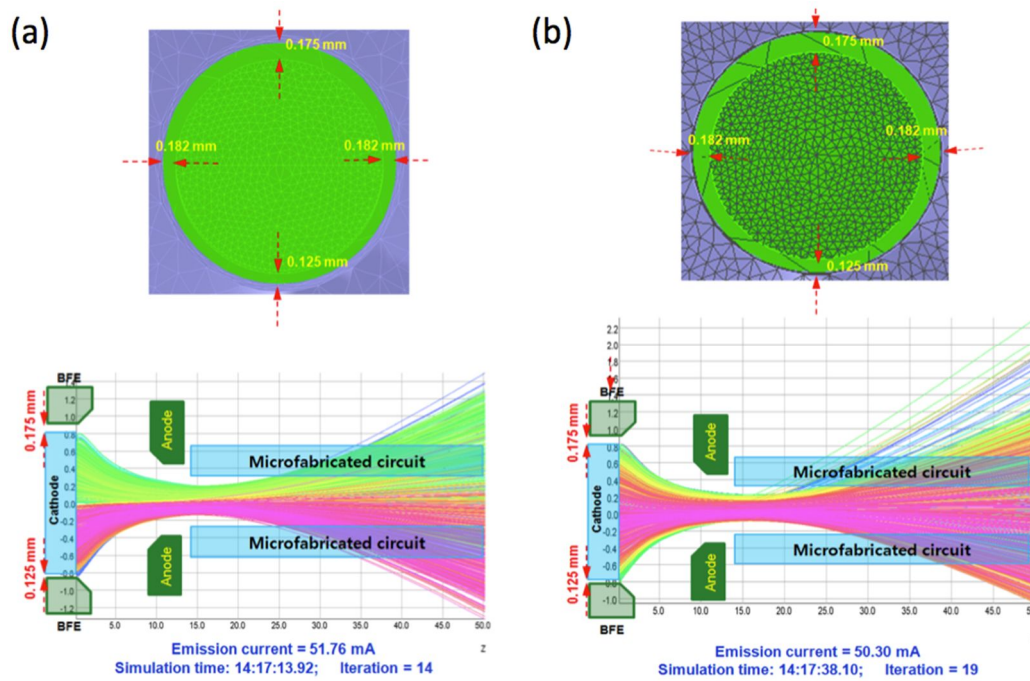


Fig. 2.24. BFE vs Cathode misalignment study (a) when cathode is moved 25 μ m from axis and (b) BFE is moved 25 μ m from axis.

2.3.2. Fabrication of electron gun

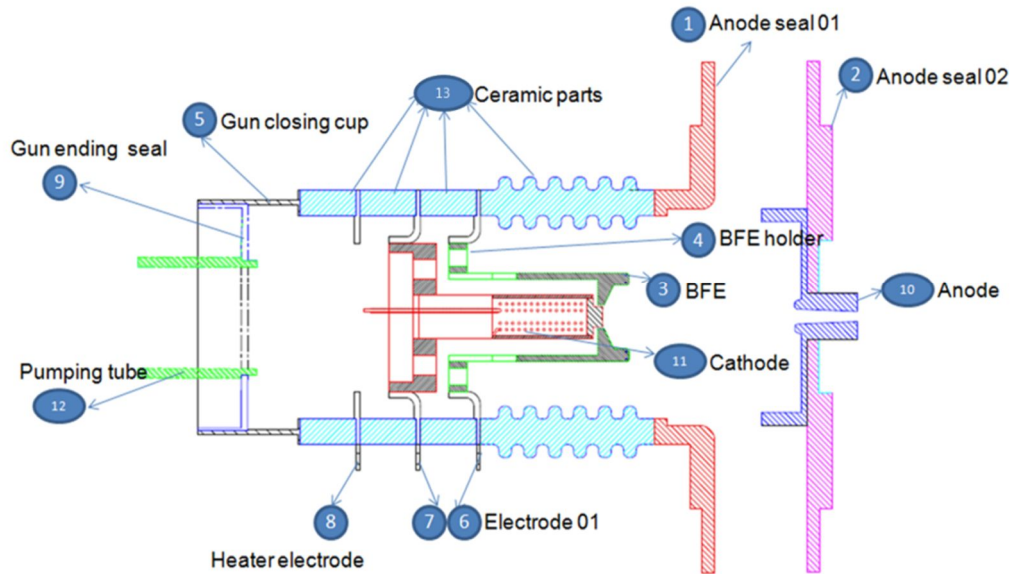


Fig. 2.25. CAD drawing of assembly of 12kV, 50mA electron gun.

Fig. 2.25 represents the composition of engineer designed electron gun. The key issues to design the electron gun is summarized as electric isolation, Alignment of cathode, BFE, and anode. I followed most of the design from previous researches in our lab. [14] 96% alumina is used as electric isolating material, and all the electrodes are made of Kovar, which has similar thermal expansion rate to ceramic so that the e-gun envelope should be kept stable even in the circumstance of brazing or baking. Molybdenum is used for anode and BFE, which should be strong enough resisting the high energy electron beams. Fig. 2.26 shows the M type cathode and its drawing and Fig. 2.27 shows the brazed gun envelope as well as the jigs used while brazing.

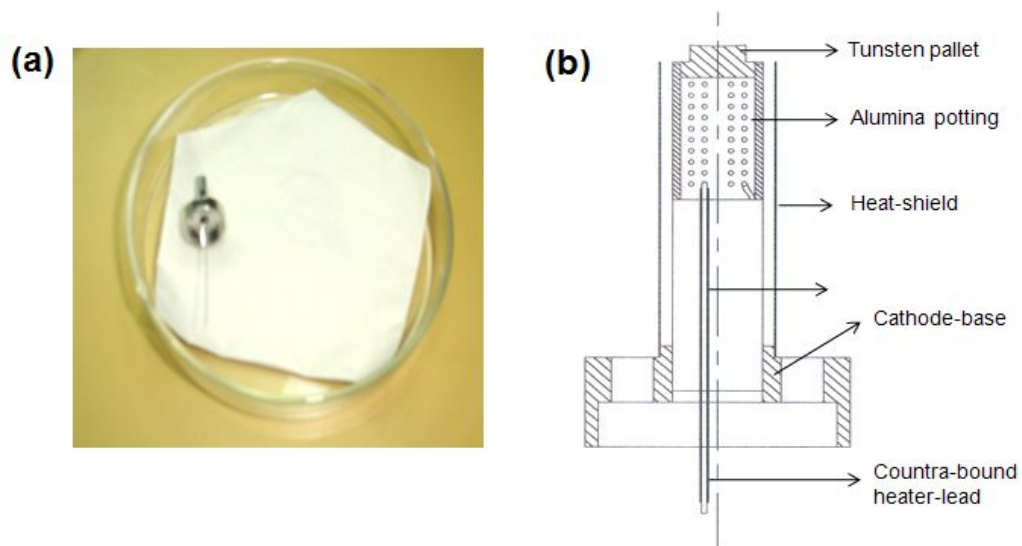


Fig. 2.26. M-type dispenser cathode: (a) cathode with its base-structure, and (b) CAD view with sub-assemblies nomenclature [14]



Fig. 2.27. Gun envelope brazing [14]

The next step is welding the BFE and cathode to the gun envelope and it is most critical not only because the major potential line is determined by the welding process but also because cathode gets open in the air while laser welding even heated by the laser. Therefore, the welding process should be done very quickly as well as very precisely in very clean circumstance.

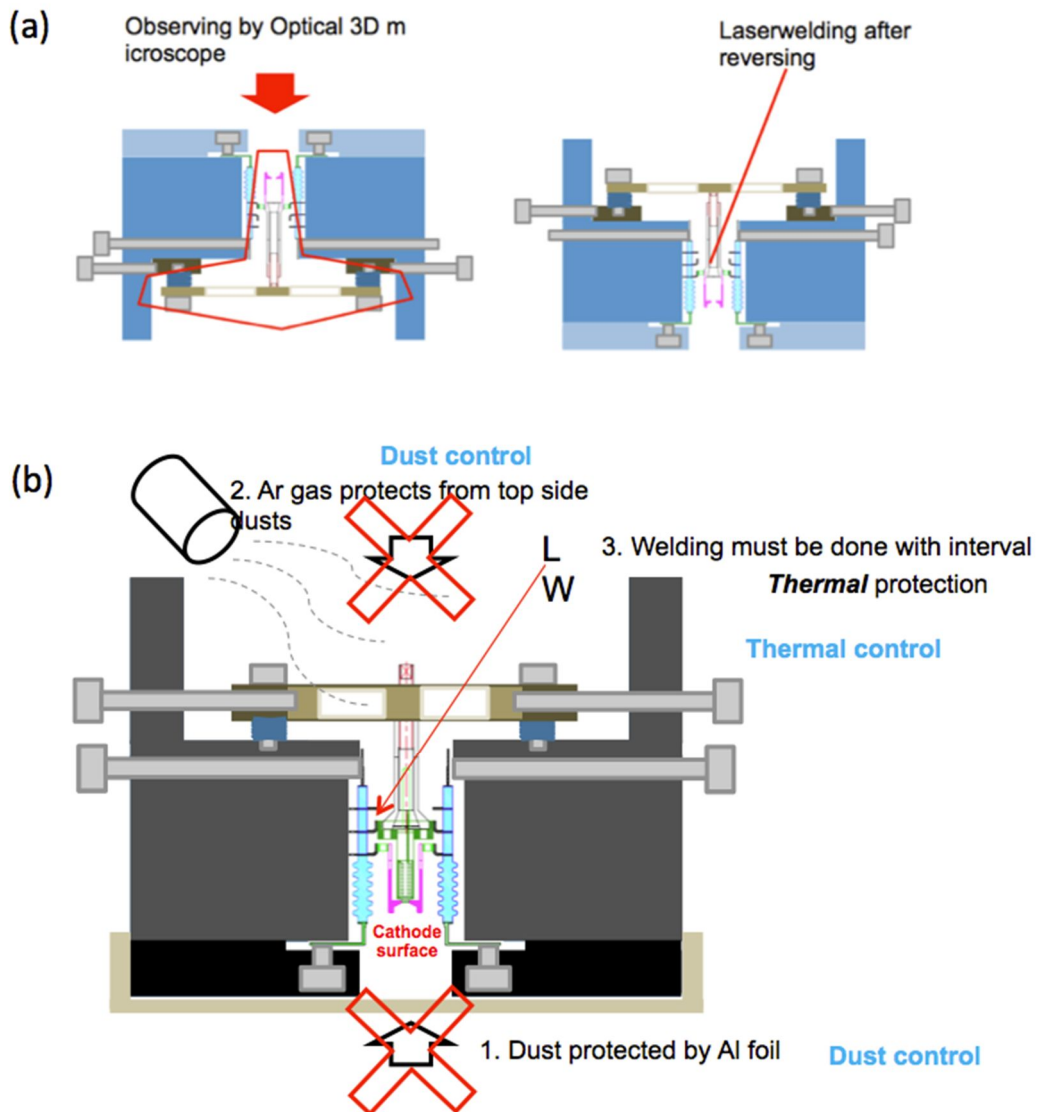


Fig. 2.28. (a) jig design for precise welding of BFE, cathode, and anode (b) careful laser welding of cathode.

Therefore, I designed new concept of welding jig by which we can precisely weld BFE, cathode, and anode while observing the position using 3D optical microscope. As shown in Fig. 2.28(a), Fig. 2.30, observing the position of the component, we can fix strongly using screws, then laser welding should be done after overturning the jig. Fig. 30 has other snaps about the jig. The welded cathode is seen in Fig. 2.31

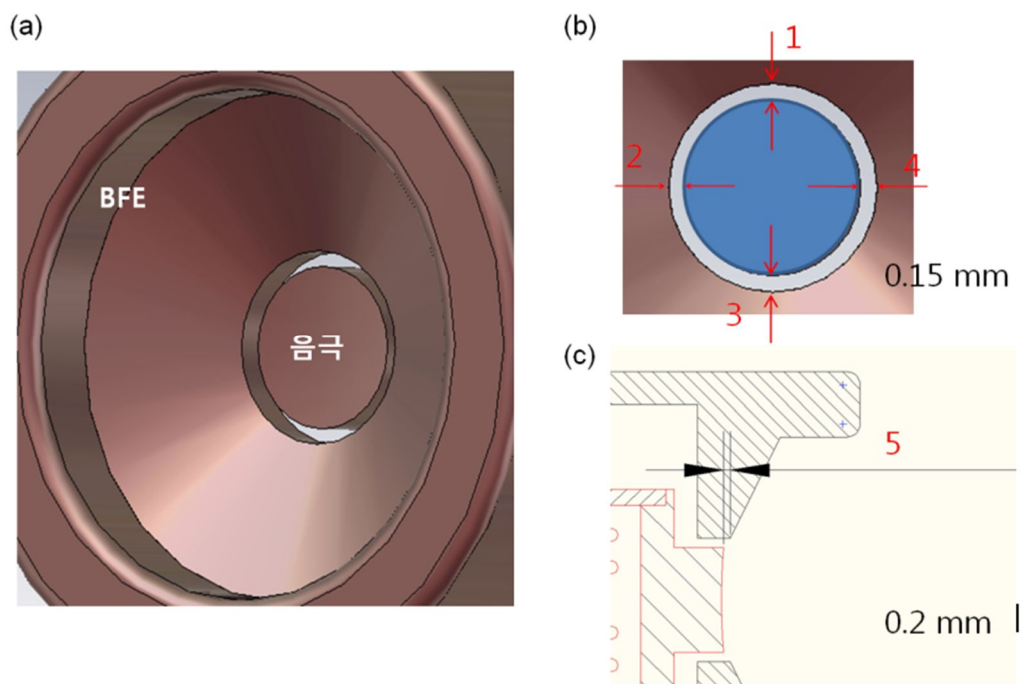
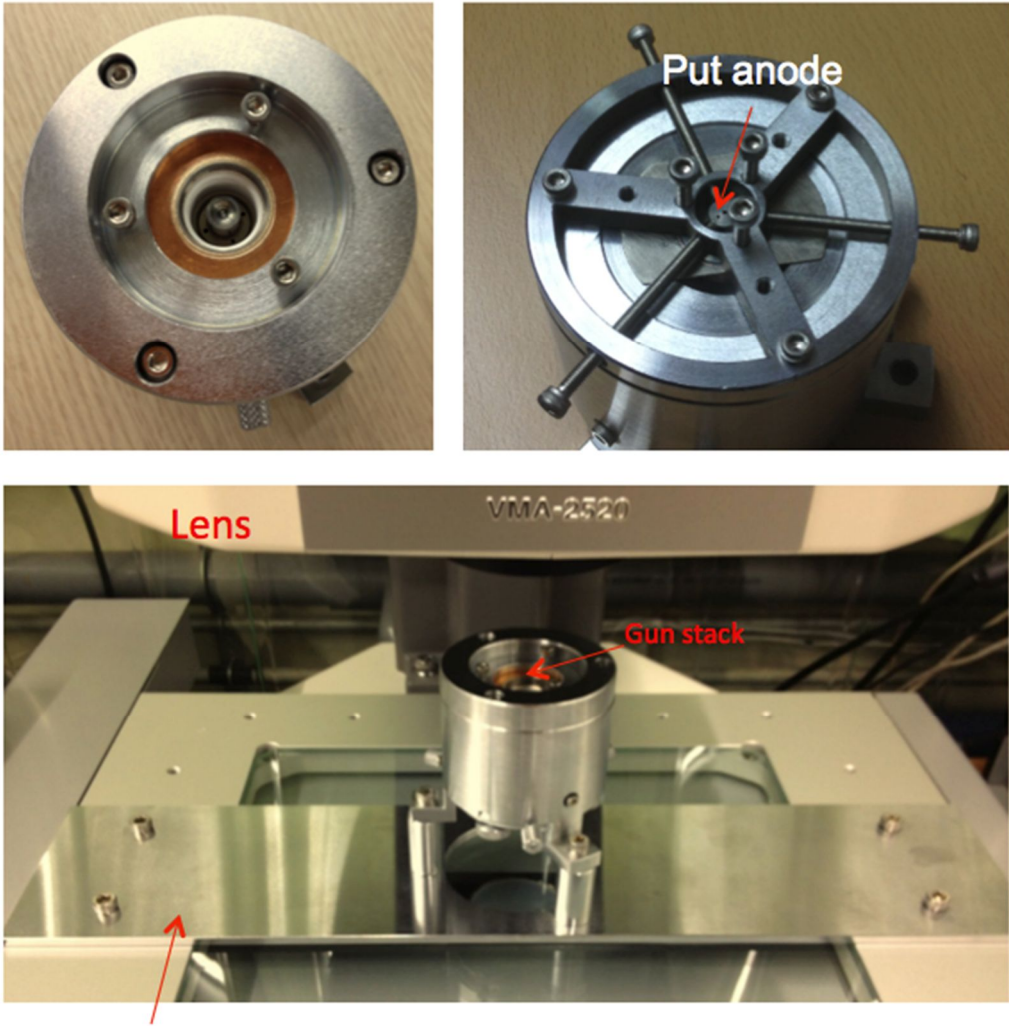


Fig. 2.29. Necessary positions of precise dimension measurement



Mounting stand: to adjust jig to microscope

Fig. 2.30. Cathode and anode connection via checking by 3D microscope

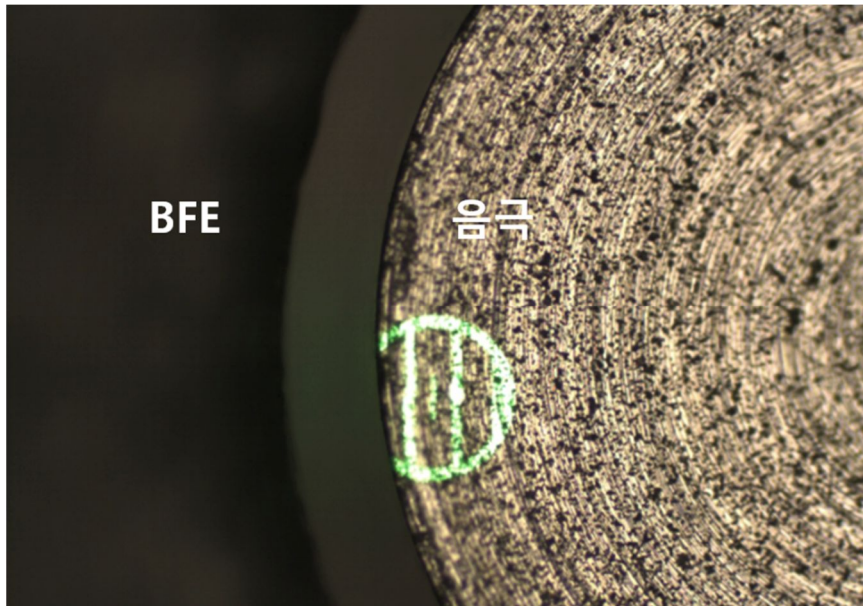


Fig. 2.29. BFE and cathode after laser welding

2.3.3. Beam-emission test

Beam emission test is performed after assembling all the system to prevent the cathode from contamination. Fig. 2.32 represents the schematic of experimental setup, and the results are shown in Fig. 2.33. What is interesting here is that we could get desired perveance via biasing 3V at BFE though it was lower than the design initially.

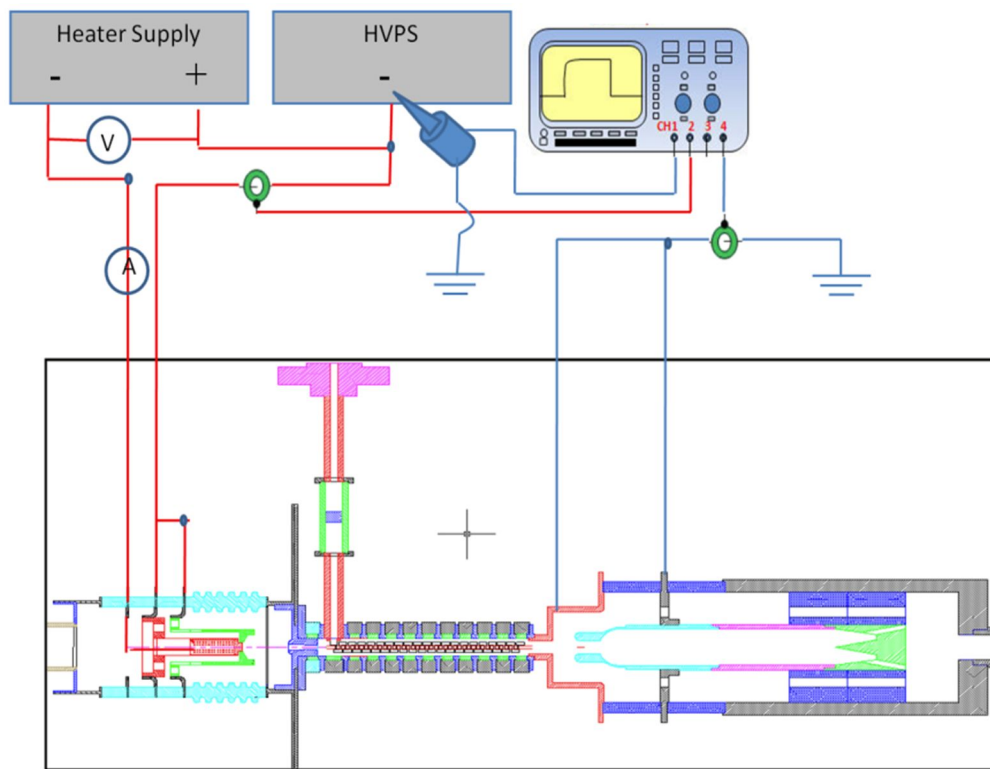


Fig. 2.32. Experimental setup of E-gun activation

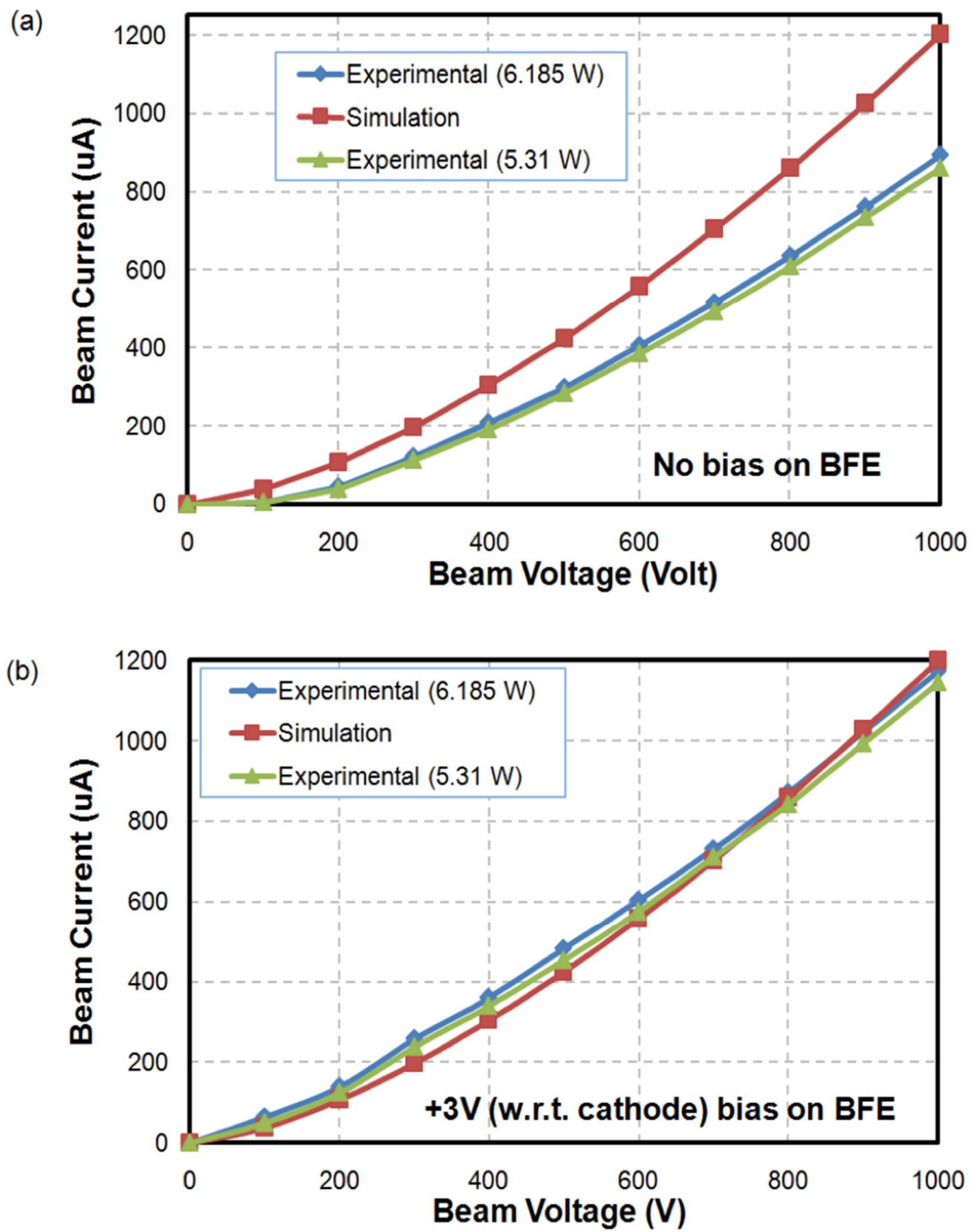


Fig. 2.33. Result of beam emission test (a) without bias, (b) with bias 3V

2.4. Periodic Permanent Magnet (PPM) focusing

We adopt PPM focusing, which is well used for the compact VEDs because it guarantees 10^2 times volume reduction comparing to solenoid focusing device. The brief principle of PPM is shown at Fig. 2.34. PPM consists of semi-circular permanent magnets, pole pieces, and spaces. The pole pieces and spacers strengthen the magnetic field inside the circuit as well as they fix the strongly magnetized circular magnets.

The axial magnetic field of PPM is generally given as,

$$B_z = B_p \cos \frac{2\pi z}{L} \quad (2.7)$$

where B_p is amplitude of magnetic field, L is the period of PPM. Then we can calculate the Brillouin flow,

$$a = \frac{1}{\omega_L} \left(\frac{\eta I}{2\pi\epsilon_0 u_0} \right)^{1/2} = \frac{2}{\eta B} \left(\frac{\eta I}{2\pi\epsilon_0 u_0} \right)^{1/2}$$

$$B_B = \frac{2}{a} \left(\frac{I}{2\pi\epsilon_0 \mu_0} \right)^{1/2} = 0.83 \times 10^{-3} \frac{I^{1/2}}{a V^{1/4}} (T) = 985 (Gauss) \quad (2.8)$$

where a is beam radius, ω_L is cyclotron frequency, η the charge to mass ratio of electron, u_0 axial beam velocity, and I is beam current. The amplitude of the magnetic field is, then,

$$B_p = \sqrt{2} B_B = 1393 \text{ Gauss. If we consider the confined flow, } B_c = 2800 \text{ Gauss.}$$

Characteristic of PPM focusing

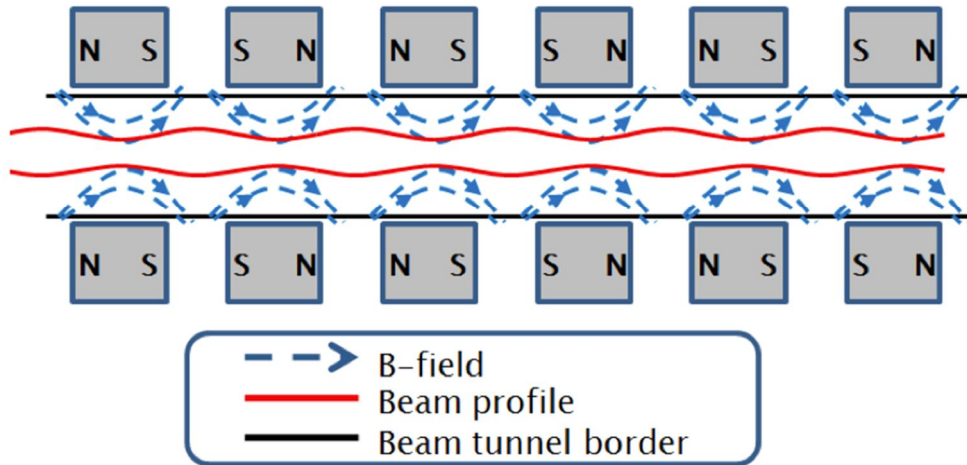


Fig. 2.34. Principle of PPM focusing

2.4.1. Design of PPM

The design process of PPM is similar to electron gun. At first, we need to calculate the maximum axial field as in previous section. Then 2D EGUN simulation and 3D OPERA 3D simulation optimization are followed. Considering the pole piece material as iron, we simulated 2D EGUN as well as OPERA 3D and we obtain the necessary field of each magnet as shown in Fig. 2.35. The necessary magnetic field calculated in OPERA3D is slightly bigger than the one obtained EGUN. In realistic case, the coupler region we cannot use full circled magnet but we have to use “U” shape magnet, which causes big magnetic loss at very important position of PPM. Therefore, the necessary magnetization should be more powerful than 2D polar symmetric simulation’s result.

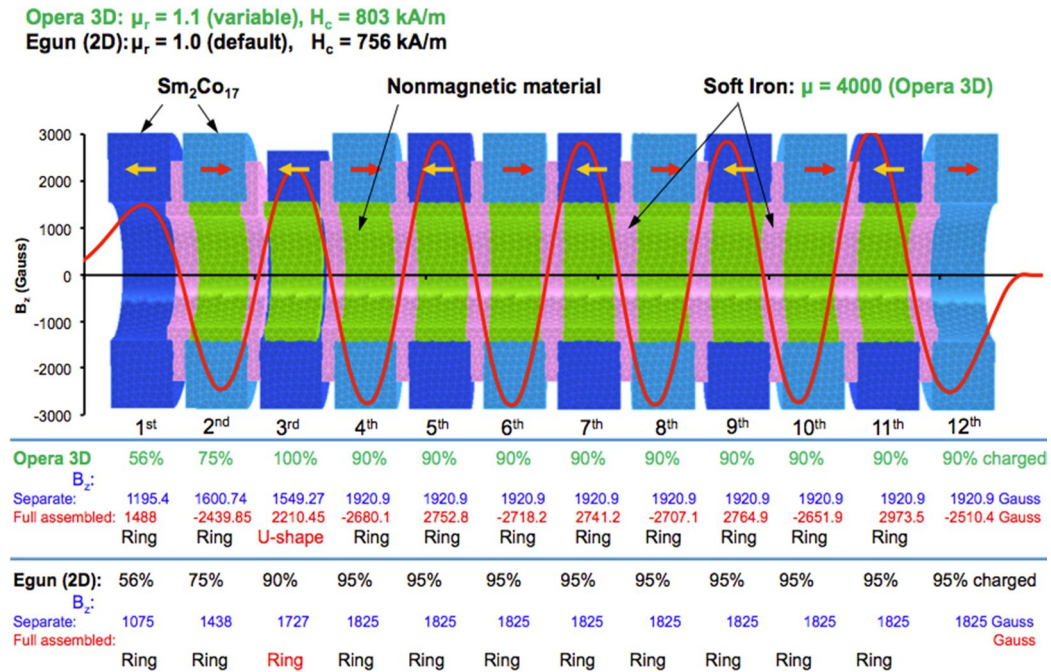


Fig. 2.35. PPM design using EGUN and OPERA3D simulation.

Using the result in Fig2.35, we successfully achieved full transmission of electrons through 0.56mm*0.56mm square of beam tunnel as shown at Fig. 2.36.

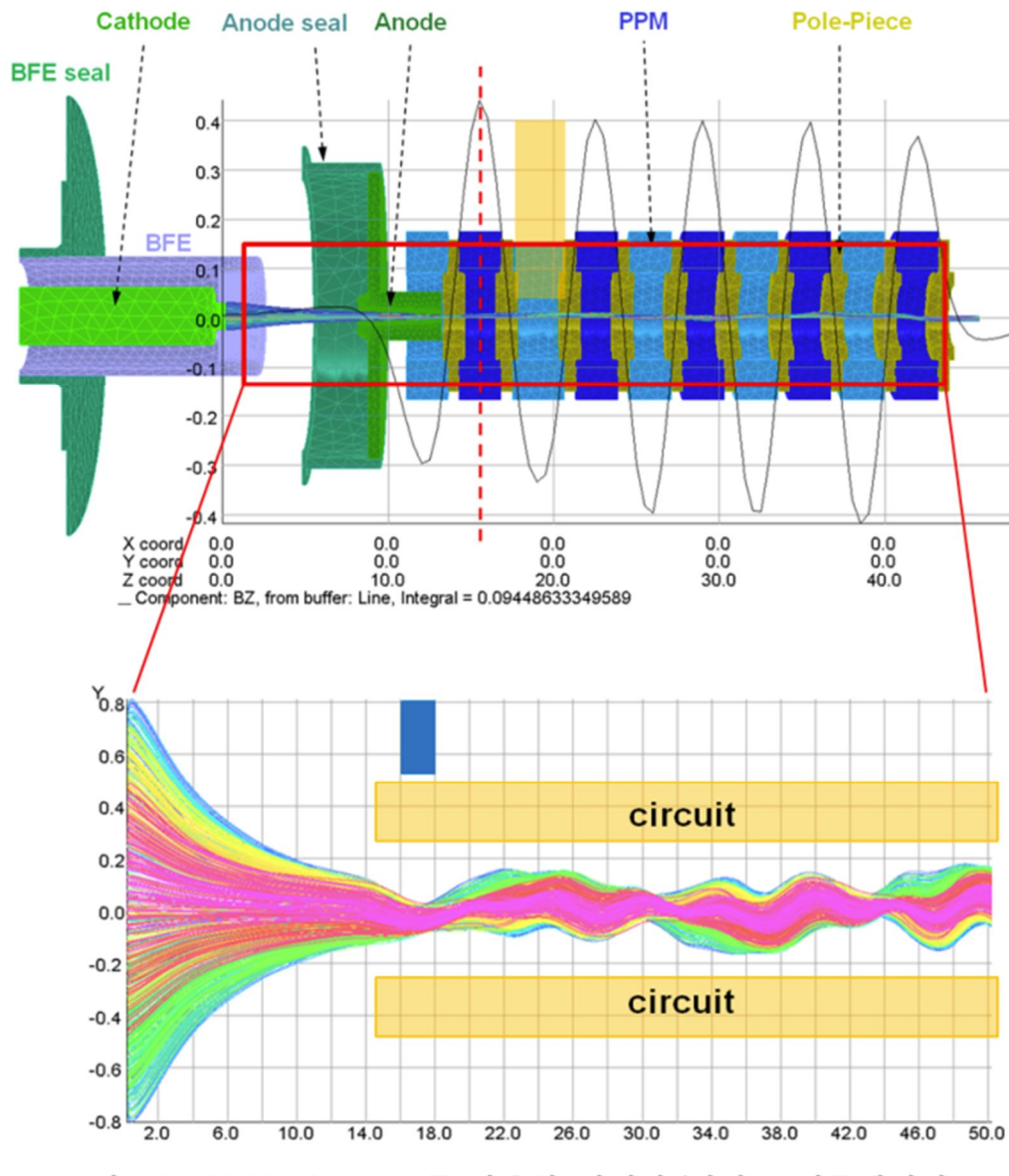


Fig. 2.36. Electron beam trajectory in the circuit using OPERA 3D

2.4.2. Fabrication of PPM

The mechanical design is not quite different from the 3D simulated parts. Fig. 2.37 indicates how the PPM components are composed. The red colored parts are iron pole pieces and the yellow parts are the spacers decided to be made of Monel404, one of the nonmagnetic Nickel alloy.

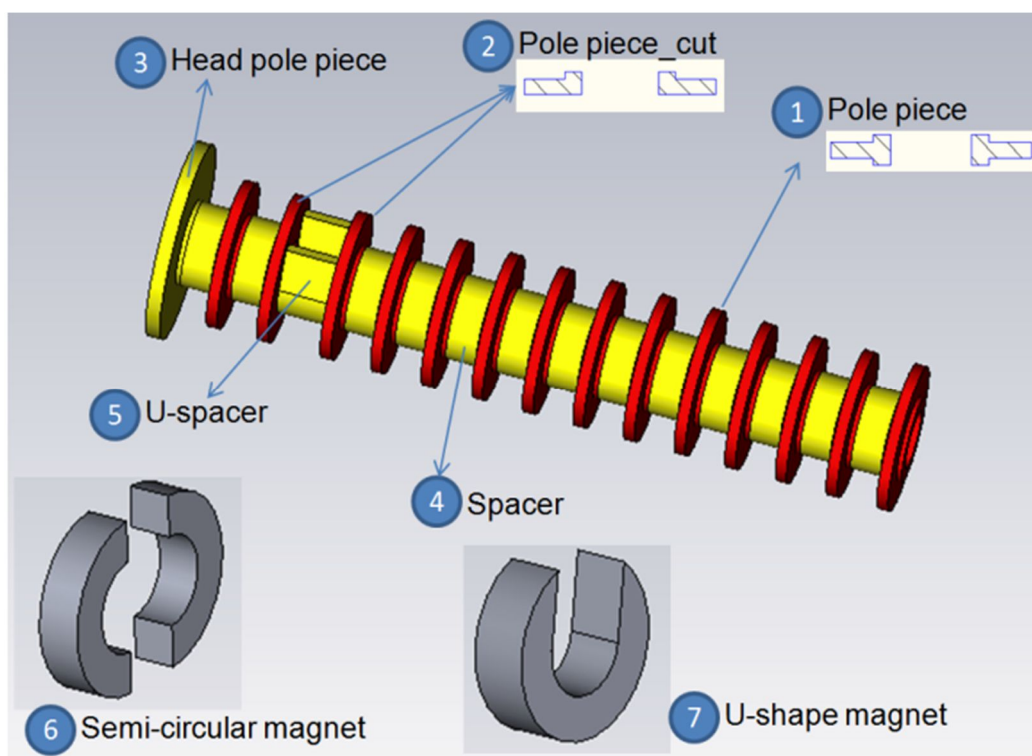


Fig. 2.37. Components of PPM.

To braze the whole round pieces concentrically is very tricky. 28 iron pole pieces and the same number of monel 404 spacers should be brazed at the same time. We made many thin circular rings as brazing alloy by cutting out from 50 μ m OFC sheet, then we insert the rings between every parts using the brazing jig shown at Fig. 2.39.

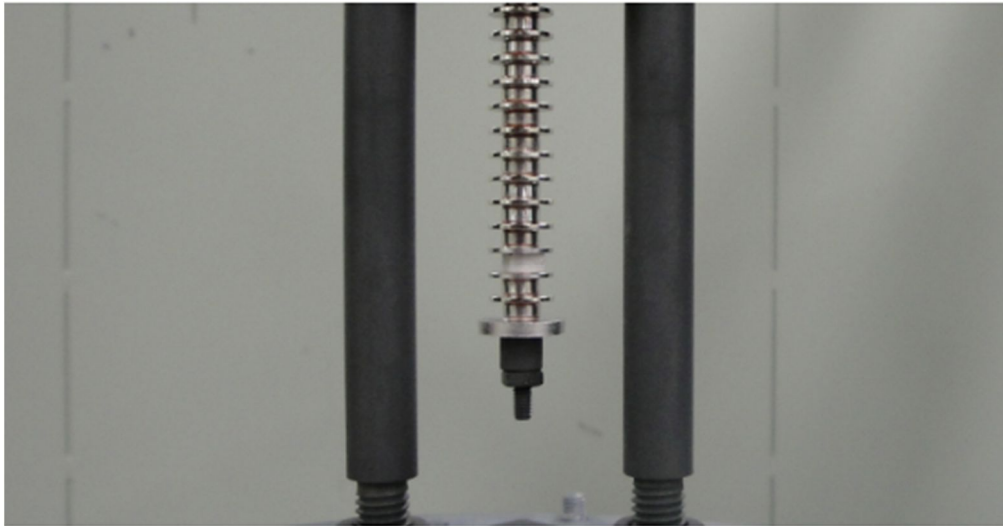
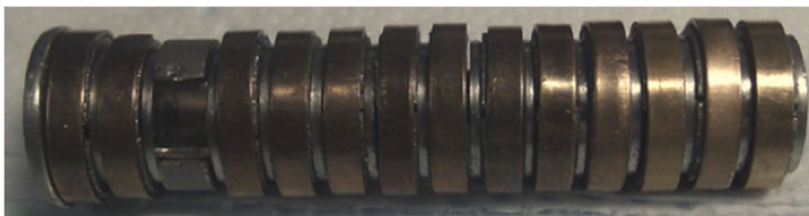


Fig. 2.38. PPM brazing using the hanging jig.



PPM Barrel



PPM (magnet included)

Fig. 2.39. Brazed PPM barrel. All magnets are installed in the figure below.

2.4.3. Measurement of PPM

To measure the magnetic field inside barrel after combining all the magnets, we prepared a gaussmeter with axial probe, 3D motorized stage, and programmed Labview code to enable computer control. Schematic of the experimental setup is seen at Fig. 2.40 and the measurement plot is shown at Fig. 2.41. The measurement shows good agreement with simulation result.

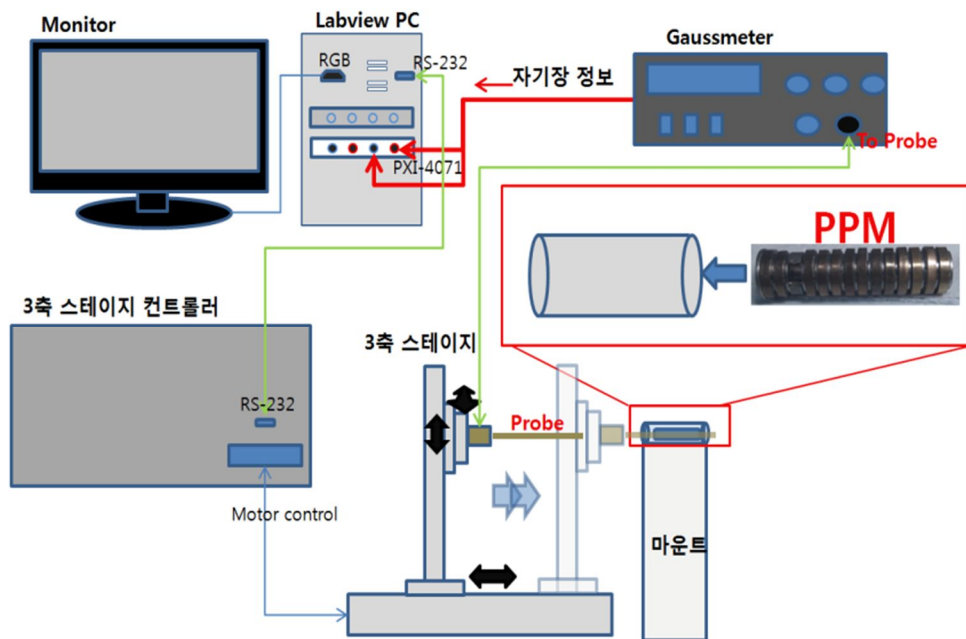


Fig. 2.40. Experimental setup to measure the magnetic field inside the PPM barrel

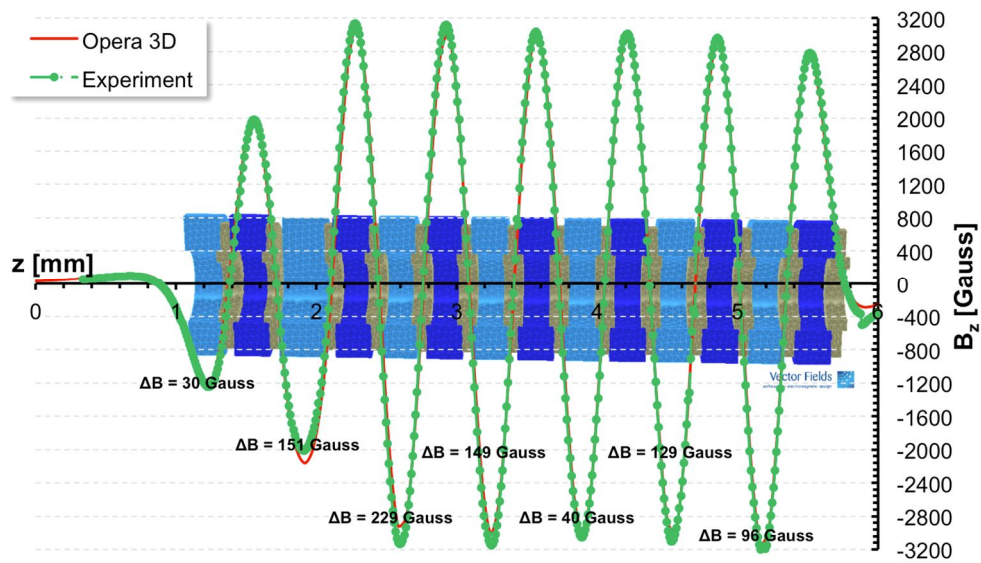


Fig. 2.41. Measurement of magnetic field inside PPM barrel. Red solid line indicates simulation result.

2.5. Wide band width anti-reflecting vacuum window

As the diverse terahertz (THz) vacuum electronic devices (VEDs) are developed with a wide variety of output power and with a different bandwidth, the technology to transmit the THz wave from the vacuum to the air without harmful reflection, which causes the undesired oscillation in the circuit or electric breakdown, has become much critical. In many cases, the wide bandwidth operation is originally included in the VEDs, for instance, travelling wave tubes (TWTs) generally have 10~20% bandwidth of the center frequency and more than 20% for the case of the backward wave oscillators (BWOs). The broad band operational vacuum window is, thus, essential for those VEDs but is terribly complex to achieve in THz frequency range, if we insist typical designs of vacuum windows. Firstly, the resonance type of vacuum window, which comprises of rectangular waveguide that is brazed with the dielectric slab whose thickness is the half-wavelength in the dielectric guide, has narrow bandwidth originally and the broadband transmission has been achieved by shaping the dielectric for the direct matching of impedance as in tapered cone structure and stepped structure, or by deploying separate matching sections near the dielectric. However, fabrication of precise arrays of those complex matching pieces are hardly achievable but also the brazing the rectangular shapes of dielectric and metal edges is no more reliable in THz range. On the contrary, the pillbox type of window has been widely used due to the advanced stability in brazing as well as the wide band property. The cylindrical pillbox brazed with thin dielectric disk works as a half-wavelength transformer so that both brazing reliability and broadband transmission are accomplished. In THz frequency region, however, the necessary thickness of the dielectric disk, that generally has high permittivity, is near or less than several tens of microns, which cause insufficient mechanical stability and which makes vacuum copular part vulnerable to the heat. Thus, highly firm diamonds or sapphires have been used in many cases to overcome the mechanical defects in

several groups. Nevertheless, it is difficult to be popularized owing to the difficulties facing high costs, micron size handling technology, etc. If the sufficiently thick dielectric is available for the pillbox type of window, most of the problems such as fabrication, mechanical stability, and high cost, etc. can be solved. However, the thick dielectric disk of pillbox type window has not been researched considerably as the trapped mode inside the thick dielectric disk, so called ghost mode, interferes the transmission near operation frequency, and as the property of the half-wavelength transformer does not hold anymore due to the increase of the effective length of the pillbox.

In this paper, we suggest hybrid of existing two methods for the broadband operational THz vacuum window. Sufficiently long pillbox brazed with multiple half-wavelengths of dielectric disk can be regarded as 3 layers of dielectric resonator. Broadband THz transmission is observed when the layers are arrayed with the specific multiple of the half-wavelength respectively in the circular guide. 0.1THz and 0.22THz vacuum window are designed based on the equivalent circuit analysis and finite difference time domain (FDTD) simulation and especially, 0.1THz window is fabricated and tested, which confirms the broadband operation of this practical THz vacuum window.

2.5.1. Transmission analysis of pillbox window

As a first part of designing wide bandwidth of THz vacuum window, we have developed an analytical way applying transmission line theory as well as the equivalent circuit theory so that we can immediately obtain the reflection coefficient of pillbox window if we just input the dimensions and impedance information of each component. The general pillbox window consists of a pillbox with a dielectric disk inside, typically in center of it, and rectangular waveguides at both ends which is schematically shown at Fig. 2.42 (a). Iris structure can be added for frequency tuning at the junctions between rectangular waveguides and pillbox, nonetheless, it is not considered in this paper on purpose because what we aimed here is non-serious design, which is not difficult at all so that we might not have to tune for adjustment of required frequency.

As mentioned earlier, the thickness of the dielectric disk of the typical pillbox window should be in general much less than the target wavelength so that it is analyzed as a simple susceptance when we apply equivalent circuit theory. Supposing the dielectric thickness is about wavelength scale or more than that, which is strongly recommended in THz range, however, the dielectric layer can be regarded as an independent transmission line section with its own characteristic impedance. Applying these conditions, the equivalent circuit of pillbox window should be like Fig. 2.42 (d). The rectangular waveguide section, pillbox empty sections, and the dielectric section are interpreted as transmission lines with characteristic admittance Y_r , Y_p , and Y_c respectively. We supposed that TE₁₀ mode propagate only in rectangular waveguide, and TE₁₁ mode in empty pillbox region as well as in the dielectric disk. The guide wavelength in each section is set respectively λ_{g_r} , λ_{g_p} , and λ_{g_c} . The most difficult part to apply the equivalent circuit theory for the pillbox vacuum window is to find the adequate susceptance that occurs at the junctions between rectangular waveguide and cylindrical pillbox. In the junction, the wave

experiences transverse phase change so that infinite number of different modes can absorb energy from the fundamental mode, which prevents the wave from perfect transmission through it. Gary B. Eastham, et al. analyzed the susceptance of the rectangular aperture in transverse plane of a circular waveguide using modal expansion. [15] We assumed that the susceptance of the junction between those two different types of waveguides would be half of one of the rectangular aperture in circular waveguide. Therefore, the susceptance B is

$$B = -\frac{\lambda_g R^2 \left[(p'_{11})^2 - 1 \right] J_1^2(k_c R)}{2\alpha_m (p'_{11})^2} \left(1 - \frac{\lambda_c^2}{\lambda^2} \right). \quad (2.9)$$

where λ_g is the wavelength in the circular waveguide, that is, empty pillbox region, R is the radius of pillbox, λ_c is the cutoff wavelength of the rectangular waveguide, k_c its wavenumber, p'_{11} is the first root of derivative of the Bessel function $J_1'(k_c r) = 0$, and α_m is magnetic polarizability of the rectangular entrance of waveguide that is defined as $\alpha_m = 0.132b^3 \ln(1 + 0.66(b/a))$ where a represents the longer side of rectangular waveguide, and b the shorter one as shown in the cross sectional view at Fig. 2.42(c). [16]

In transmission line theory, the input admittance Y_{in} at the distance l from the joint with different characteristic impedance region is known as

$$Y_{in} = Y_0 \frac{Y + iY_0 \tan(\beta l)}{Y_0 + iY \tan(\beta l)}. \quad (2.10)$$

where Y and Y_0 are load admittance and characteristic impedance of the transmission line respectively, and β is the guide wave number. Then, the reflection coefficient Γ is

Using (2.10), (2.11) the total admittance of pillbox window Y_{tot} can be obtained by consequent algebra and we have

$$Y_{tot} = \frac{A + iG}{C + iD}. \quad (2.12)$$

$$A = Y_r Y_p^2 Y_c (1 - \tan^2(\beta l)) - (Y_r Y_p (Y_c^2 + Y_p^2) - B Y_r Y_c^2) \tan(\beta_c d) \tan(\beta l) - 2B Y_r Y_p Y_c \tan(\beta l)$$

$$G = 2B \left[Y_p^2 Y_c (1 - \tan^2(\beta l)) - Y_p (Y_c^2 + Y_p^2) \tan(\beta_c d) \tan(\beta l) \right] + 2Y_p Y_c (Y_p^2 - B^2) \tan(\beta l) + Y_p^2 (Y_c^2 - B^2) \tan(\beta_c d) + (B^2 Y_c^2 - Y_p^4) \tan(\beta_c d) \tan^2(\beta l)$$

$$C = \frac{A}{Y_r} = Y_p^2 Y_c (1 - \tan^2(\beta l)) - (Y_p (Y_c^2 + Y_p^2) - B Y_c^2) \tan(\beta_c d) \tan(\beta l) - 2B Y_p Y_c \tan(\beta l)$$

$$D = Y_r \left[2Y_p Y_c \tan(\beta l) + \tan(\beta_c d) (Y_p^2 - Y_c^2 \tan^2(\beta l)) \right]$$

Therefore, we have the reflection coefficient of pillbox window as,

$$\Gamma_{tot} = \frac{Y_r - Y_0}{Y_r + Y_0} = \frac{M + iN}{O + iP}. \quad (2.13)$$

$$M = 0$$

$$N = 2Y_p Y_c (Y_r^2 + B^2 - Y_p^2) \tan(\beta l) + (Y_r^2 + B^2 - Y_c^2) Y_p^2 \tan(\beta_c d) - 2B Y_p^2 Y_c (1 - \tan^2(\beta l)) + 2B Y_p (Y_c^2 + Y_p^2) \tan(\beta_c d) \tan(\beta l)$$

$$\begin{aligned}
O &= 2Y_r Y_p \left[Y_p Y_c (1 - \tan^2(\beta l)) - (Y_c^2 + Y_p^2) \tan(\beta_c d) \tan(\beta l) \right] \\
&\quad - 2B Y_r \left[2Y_p Y_c \tan(\beta l) + \tan(\beta_c d) (Y_p^2 - Y_c^2 \tan^2(\beta l)) \right] \\
P &= 2Y_p Y_c (Y_r^2 - B^2 + Y_p^2) \tan(\beta l) + (Y_r^2 - B^2 + Y_c^2) Y_p^2 \tan(\beta_c d) \\
&\quad + 2B Y_p^2 Y_c (1 - \tan^2(\beta l)) - 2B Y_p (Y_c^2 + Y_p^2) \tan(\beta_c d) \tan(\beta l)
\end{aligned}$$

Though the final analytical result is still long and complex, we can instantly obtain reflection coefficient in the moment we input the waveguide dimension and operation frequency. In addition, it is available to intuitively guess the starting parameters for anti-reflecting desired frequency of wave. As a first important guess, I assume that the default length of each sections should be multiple of half of guide wavelength of center frequency at each section so that total structure acts like a combination of half wave transformers, which enables at least the aimed frequency of wave to transmit the pillbox window properly. Then, it is necessary to apply additional phase change at the junctions between rectangular waveguides and cylindrical waveguides. Consequently, empty sections of pillbox must be slightly different from the multiple of half guide wavelength. i.e., the phase change in the section would be

$$\beta l = m\pi + \delta. \quad (2.14)$$

where m is an integer number, δ denotes slight phase change caused by waveguide conversion. Nonetheless, the dielectric inside pillbox doesn't affect the phase in ideal condition where the inner diameter of pillbox is exactly same to dielectric disk's outer diameter. The discontinuity at dielectric surface only changes real number of the impedance so that the dielectric length can be kept as multiple of half wavelength, i.e., we can assume

$$\beta_c d = n\pi . \quad (2.15)$$

where n is integer. From this assumption, I have swept the parameters n , m , and δ in (5) and we obtained important relationships for broadband transmitting pillbox window.

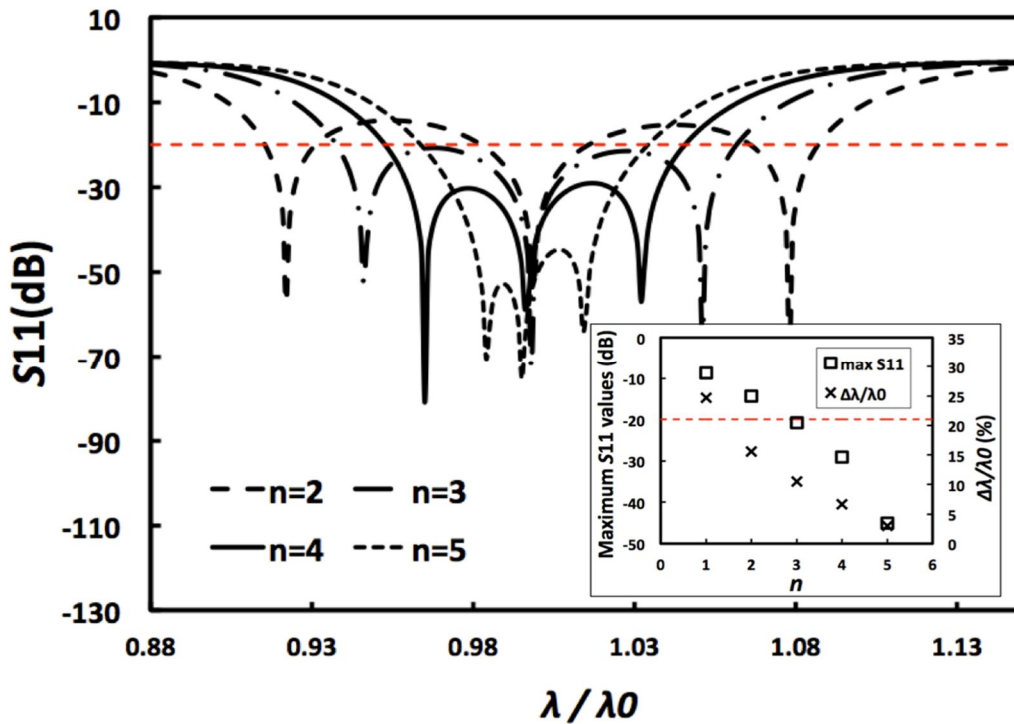


Fig. 2.43. S_{11} calculation versus wavelength for different n defined at (7). In the inset, we plot band gap between two dips near center wavelength and we plot the maximum return loss in the gap. The dashed red line indicates anti-reflecting baseline with -20dB return loss.

First, changing the integer number n in (7), we can manipulate the dips near the operation frequency, which means that it is available to gather those dips near the operation frequency as well as is possible to apart them from each other. Fig 2.43 shows how the parameter n affects the pass band of pillbox window. If $n < 3$, the

neighbored dips are far away so that we have big reflection at the frequency between the dips, on the contrary, in case of $n > 4$, the low extremes are too close, resultantly, it is not feasible to have broadband operation. When $n = 3$ or 4 , however, 3 close dips are distributed within 10% range of center wavelength and we can get strong transmission near and between the gaps. 7% bandwidth to center wavelength achieved when $n = 4$, and more than 10% when $n = 3$.

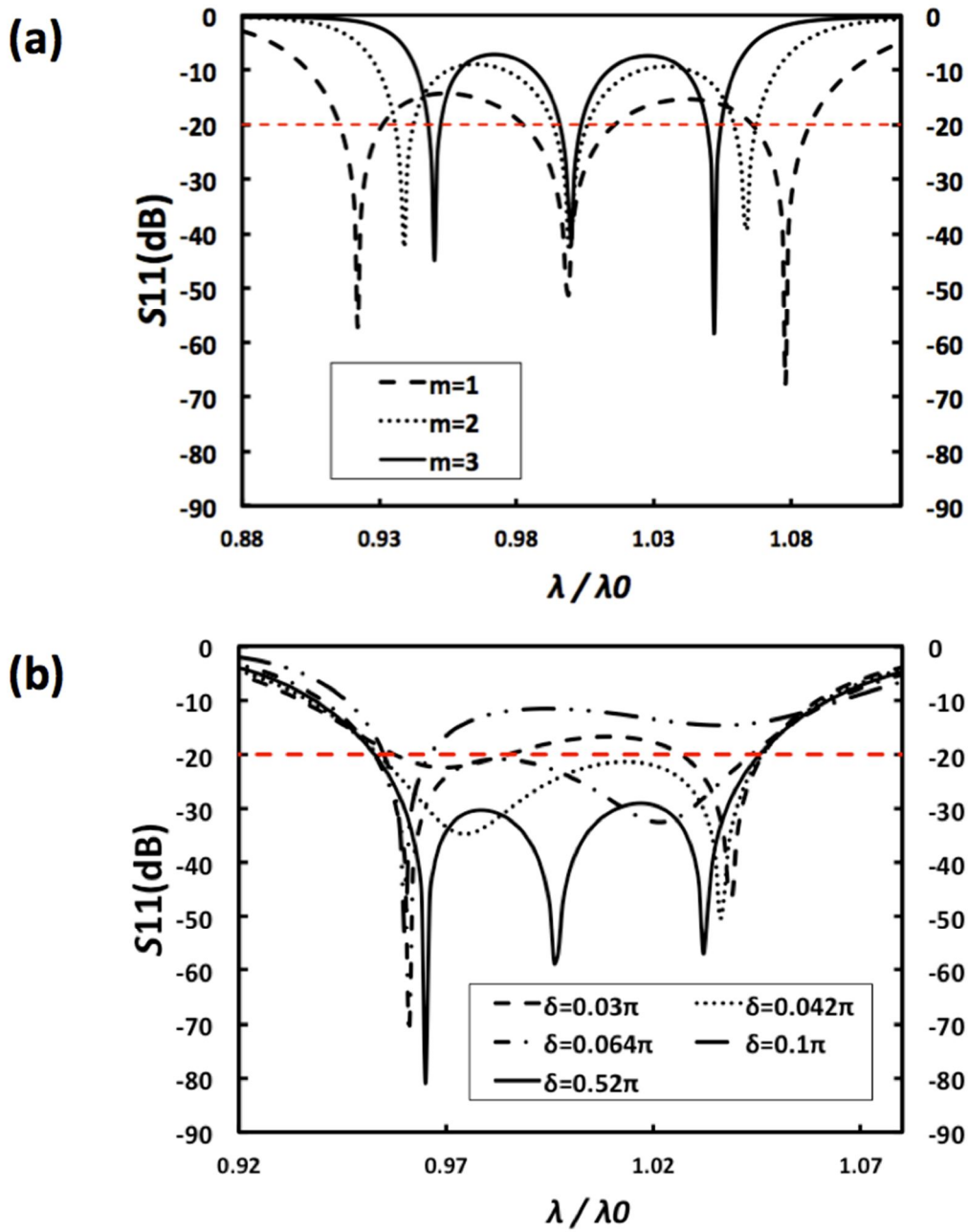


Fig. 2.44. S_{11} versus wavelength (a) for the parameter m at (6), and for δ at (7). The dashed red line denotes -20dB return loss baseline

The parameter m also affects the dips, though its effect is less than n 's. The S11 behavior w.r.t m is shown at Fig. 2.44 (a) As m is increased, the dips near the center frequency get closer slightly but the dips become sharper, which prevents the pass band from combining together, i.e., the operating band width gets narrower, which is not shown in case of n . We, therefore, can conclude that the optimum value of m should be 1.

δ is another important parameter that is directly related to the pillbox length L . This phase correction would compensate the transverse phase change at the waveguide junction, if we choose the right value. In Fig. 2.44 (b), we demonstrated that the return loss is kept below -20dB with maximal range of wavelength when the phase correction is in the range $0.042-0.064\pi$. This range would decide the fabrication tolerance of pillbox window for chosen frequency.

2.5.2. Design of broadband width of 0.1THz vacuum window

To verify how precisely the analysis works, we have designed realistic THz windows, the operation frequency of which are 0.1THz, 0.22THz respectively. Many VEDs are under development to work at those frequencies due to the low atmospheric absorption. We have chosen WR-10 (2.54mm *1.27mm) and WR-4 (1.0922mm*0.5461mm) standard wave guides for 0.1THz and 0.22THz respectively. The pillbox diameter is decided to be the same to the diagonal of each waveguide. We select Al₂O₃ 99.8% as the material of a dielectric disk due to the mechanical stability and feasibility as well as relatively low cost. (c.f. diamond and sapphire are mostly used in THz range) Applying the results written in section A, most of the parameters are decided and we have confirmed our design using well known 3 dimensional (3D) finite difference time domain (FDTD) tool, CST Microwave Studio (MWS). (reference) Fig.2.45. show that the analytical results applying equivalent circuit theory match quite well within few percent of difference error in frequency from the FDTD MWS results in both 0.1THz window and 0.22THz one. In the simulation, we found that if we adjust the phase correction parameter δ , i.e., the pillbox length slightly bigger from the analytically calculated value, e.g. 50mm for the case of 0.1THz, the reflection behavior against frequency matches surprisingly. Conclusively, in the design of 0.1 THz pillbox window, we obtained 0.091- 0.104 THz pass band when $n = 3$, and 0.093-0.101 THz when $n = 4$, and for the case of 0.22THz one, 0.207-0.235 THz when $n = 3$, 0.211-0.231 THz when $n = 4$. Considering the decline during the fabrication, we decided the parameter n to be 4 to have stable <-20 dB return loss. We list the finalized optimum parameters of both 0.1THz and 0.22 THz pillbox window in table 1. In both cases, we have broad pass band exceeding 10% of center frequency through those windows. We list the important parameters in table 2.4

Another important results here other than the wide bandwidth of operation pass band is that we can design these vacuum windows with realizable tolerance level using conventional machining even in THz range. As shown in Fig 47, the pass band remains stable even though the dips sensitively move if we keep the pillbox length l within 30 micrometer tolerance in case of 0.1 THz window. We have demonstrated this experimentally in next chapter.

TABLE 2.4. PARAMETERS FOR 0.1THZ, 0.22THZ VACUUM WINDOW

Parameter	Note / unit	0.1THz	0.22THz
a	width of rectangular waveguide / mm	2.54	1.0922
b	height of rectangular waveguide / mm	1.27	0.5461
R	radius of pillbox / mm	1.42	0.61
R_c	radius of dielectric / mm	1.42	0.61
L	Pillbox length / mm	2.12	0.95
d	Length of dielectric / mm	2	0.89
ϵ	Relative dielectric constant	9.88	9.88

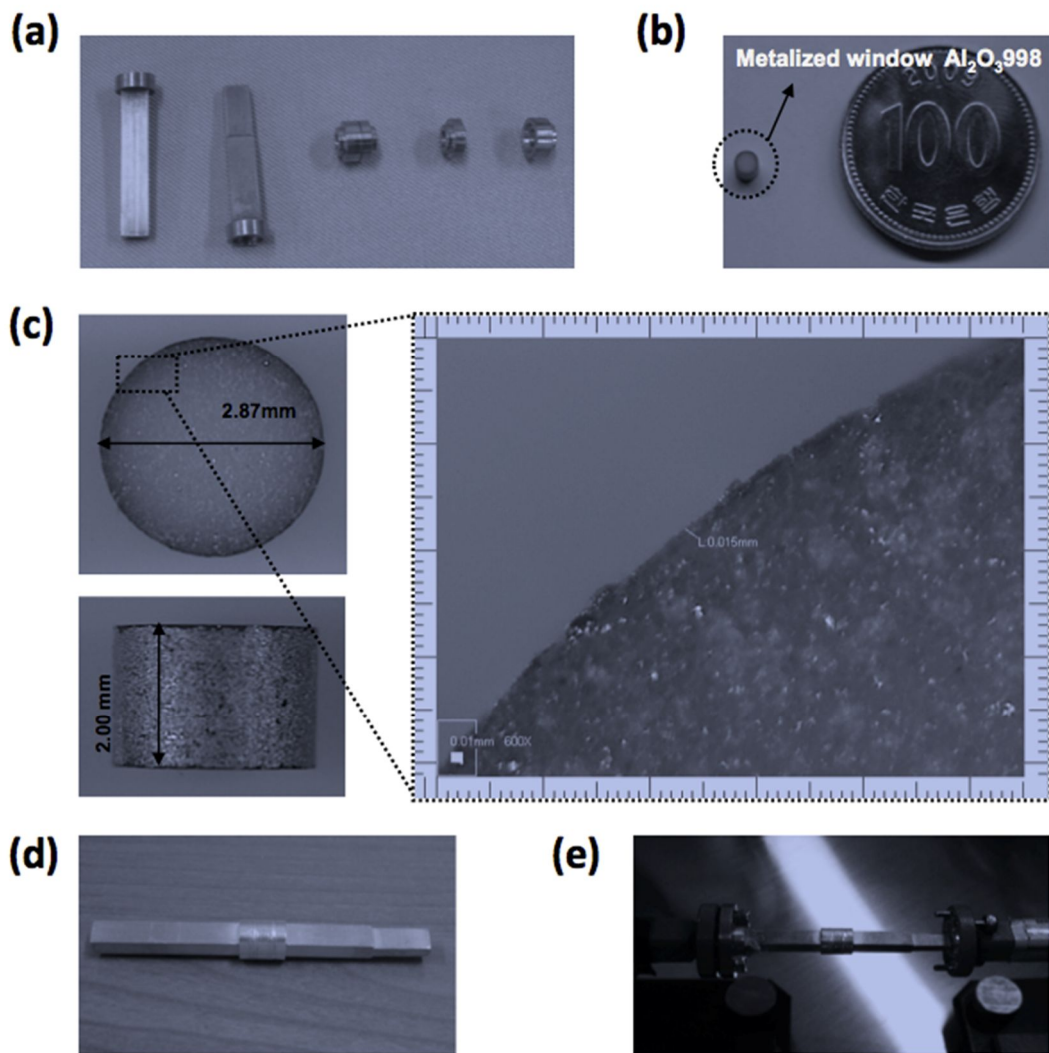


Fig. 2.45. FDTD simulation results for 0.1 THz window

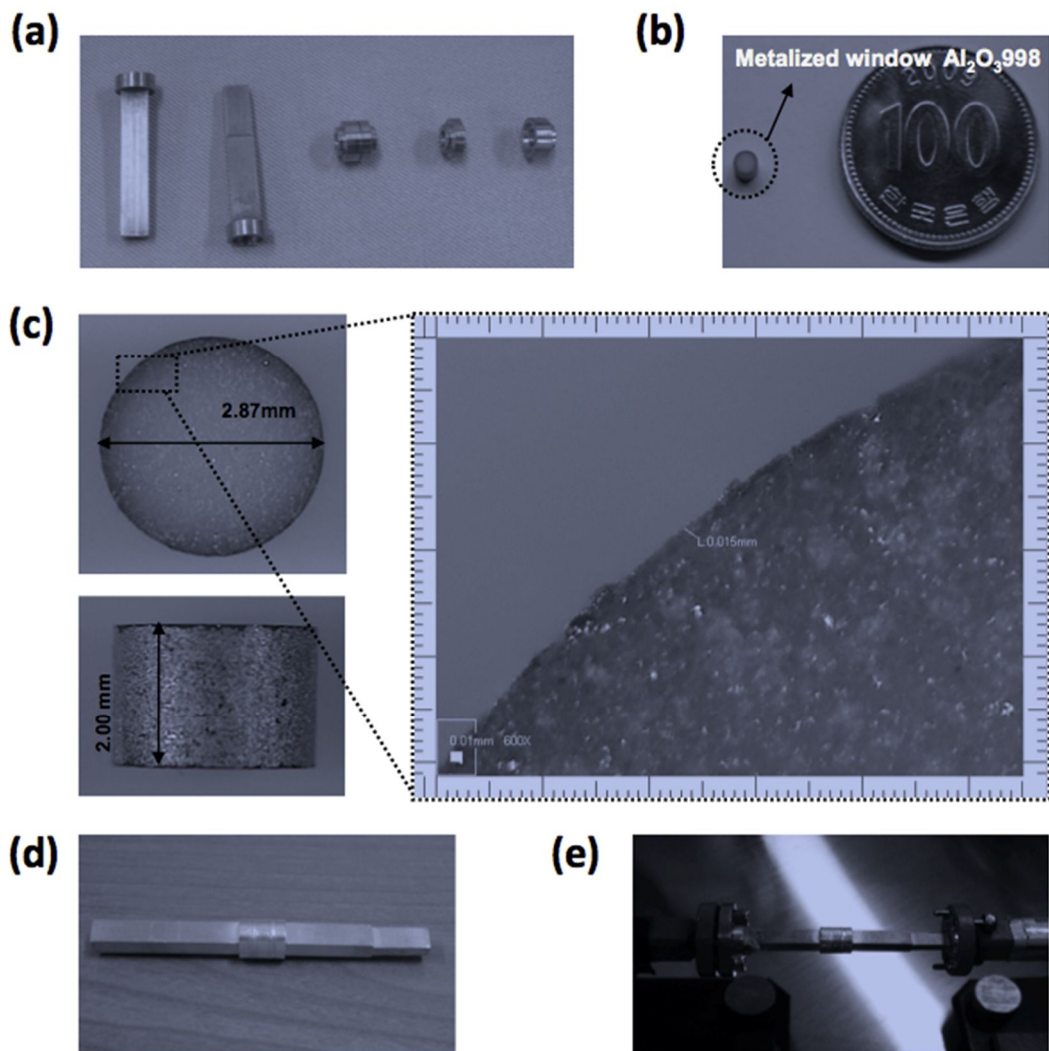


Fig. 2.46. (a) fabricated copper parts of 0.1THz window, (b), (c) fabricated alumina disk, (d) brazed 0.1THz window, (e) experimental setup of 0.1THz window coldtest

2.5.3. Cold test of 0.1THz vacuum window

Following the dimensions in table 2.4, we fabricated all the parts of 0.1THz window using conventional machining as shown at Fig. 2.46. The waveguides and pillbox parts are made of Oxygen free copper (OFC) and the dielectric window, 99.8% Al_2O_3 ceramic as mentioned before. Although the dielectric constant is given by the vendor, we measured it using by a simplified hemispherical open resonator technique, because it is directly related to effective volume, area, and length of the material, which affects transmission performance critically. Using the optical microscope, we measured all parts with $2\mu\text{m}$ resolution. The radial direction of tolerance is $+10\mu\text{m}$ whereas the longitudinal one is $+20\mu\text{m}$. Al_2O_3 ceramic disk is machined with great precision level, near $+5\mu\text{m}$ tolerance even including $15\mu\text{m}$ thickness of metallized layer, which is essential for brazing with OFC pillbox. After combining the ceramic inside pillbox first by furnace brazing, we finalize to assemble 0.1THz window by brazing the guides and pillbox all together.

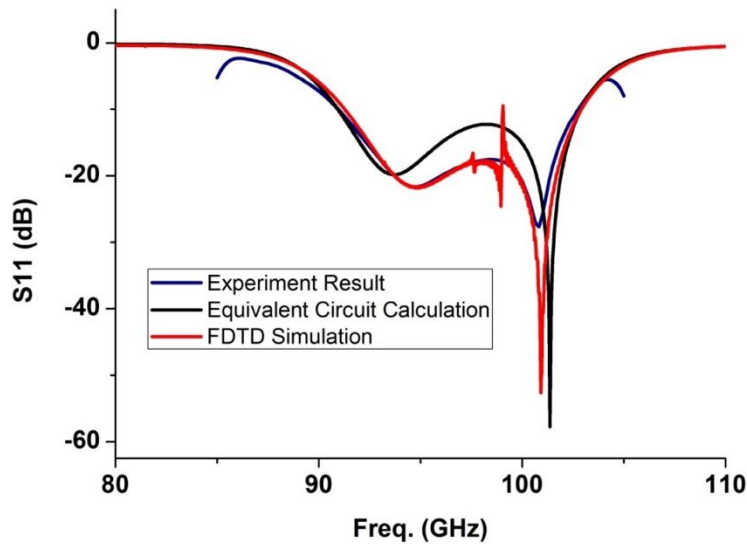


Fig. 2.47. Measurement of S11 parameter. FDTD simulation and equivalent circuit results are compared

To verify the performance of the window, standard WR-10 waveguide flanges are used at both ends of waveguide sections, then, we measured complex S parameters, S_{11} and S_{21} using W-band extended vector network analyzer (VNA). The measurement is shown at Fig. 2.48(a) with both analytical and numerical result applying the dimensional measurement. We can observe great accordance with each other and the measured pass band with $< -20\text{dB}$ return loss is $0.93\sim 0.101\text{THz}$ just as we designed, which is 8% of band center frequency.

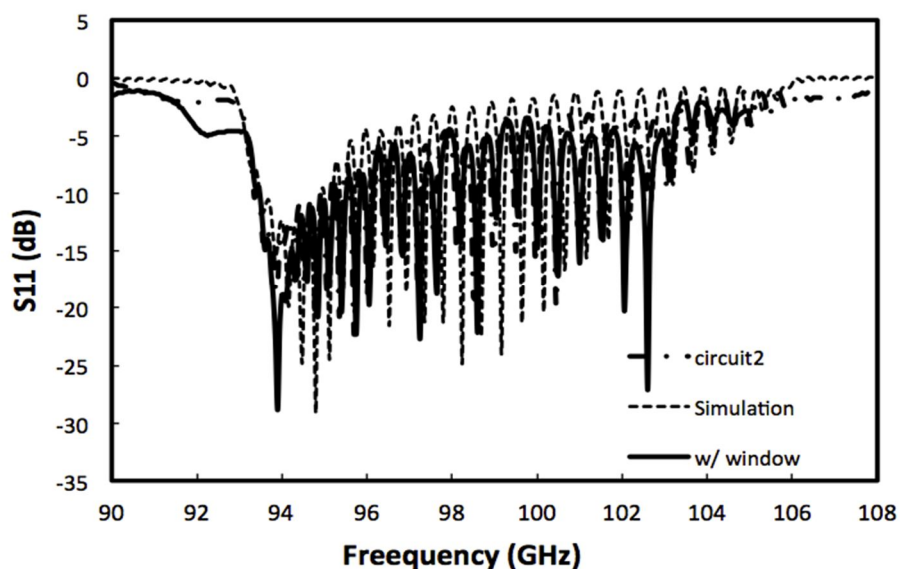


Fig. 2.48. Cold test measurement of 0.1 THz CCBWO circuit with and without window

2.6. Depressed collector

In VEDs, the electron beams passed through beam tunnel still have large amount of kinetic energy because the efficiency of the VEDs is at most 50%. The collector, therefore, is a very important part of the VEDs in safety point of view. In general collector used VEDs, the efficiency is given as output power over electron beam power and most of energy is lost by heat inevitably. If we apply repulsive potential from the collector to the circuit side, the electrons becomes slower and slower before they collide to the collectors. This kind of collector is defined as depressed collector and the efficiency of the device is changed to output power divided by (electron beam power – restored energy by depressed collector)

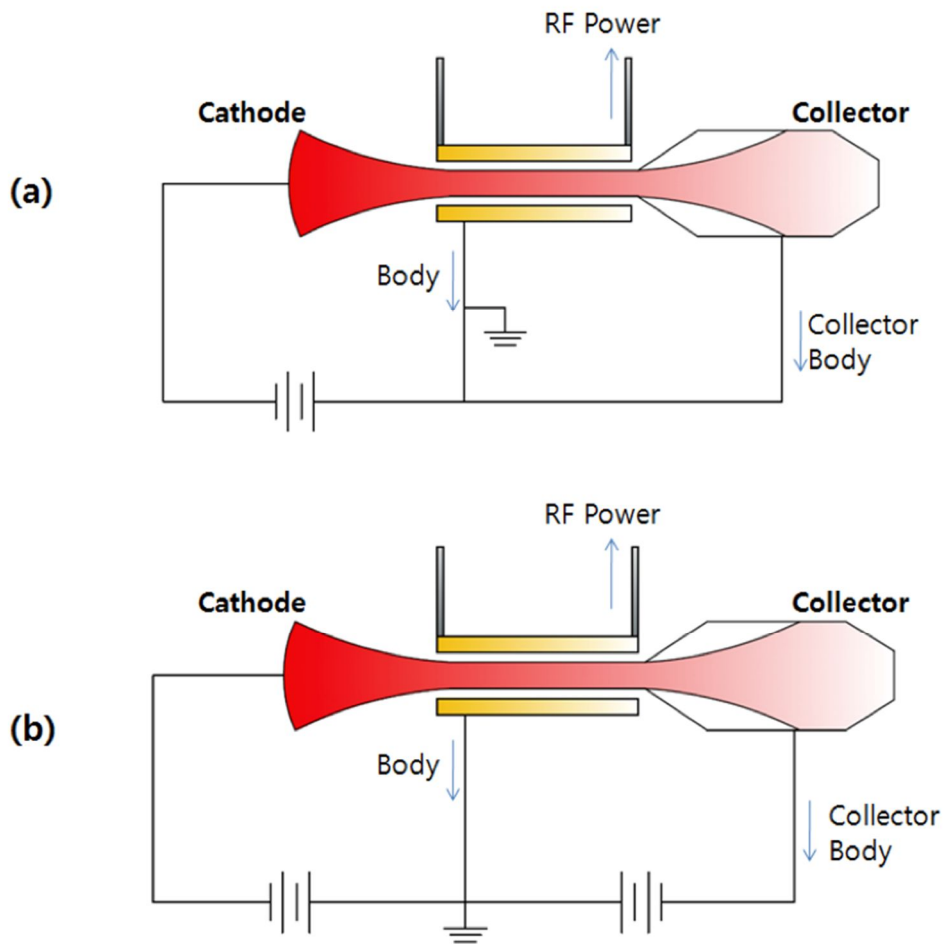


Fig. 2.49. Circuit diagram of (a) general collector (b) depressed collector

2.6.1. Design of depressed collector

We can design the depressed collector with respect to recovery efficiency. The beam power we're using is 600W. If we reduce the electron colliding heat below 150W like the power generated by high performance of CPU, the recovery efficiency should be over 75%. Therefore, we set the collector potential as -9kV and we have performed

EGUN tracking simulation as well as the thermal simulation using ANSYS Multiphysics.

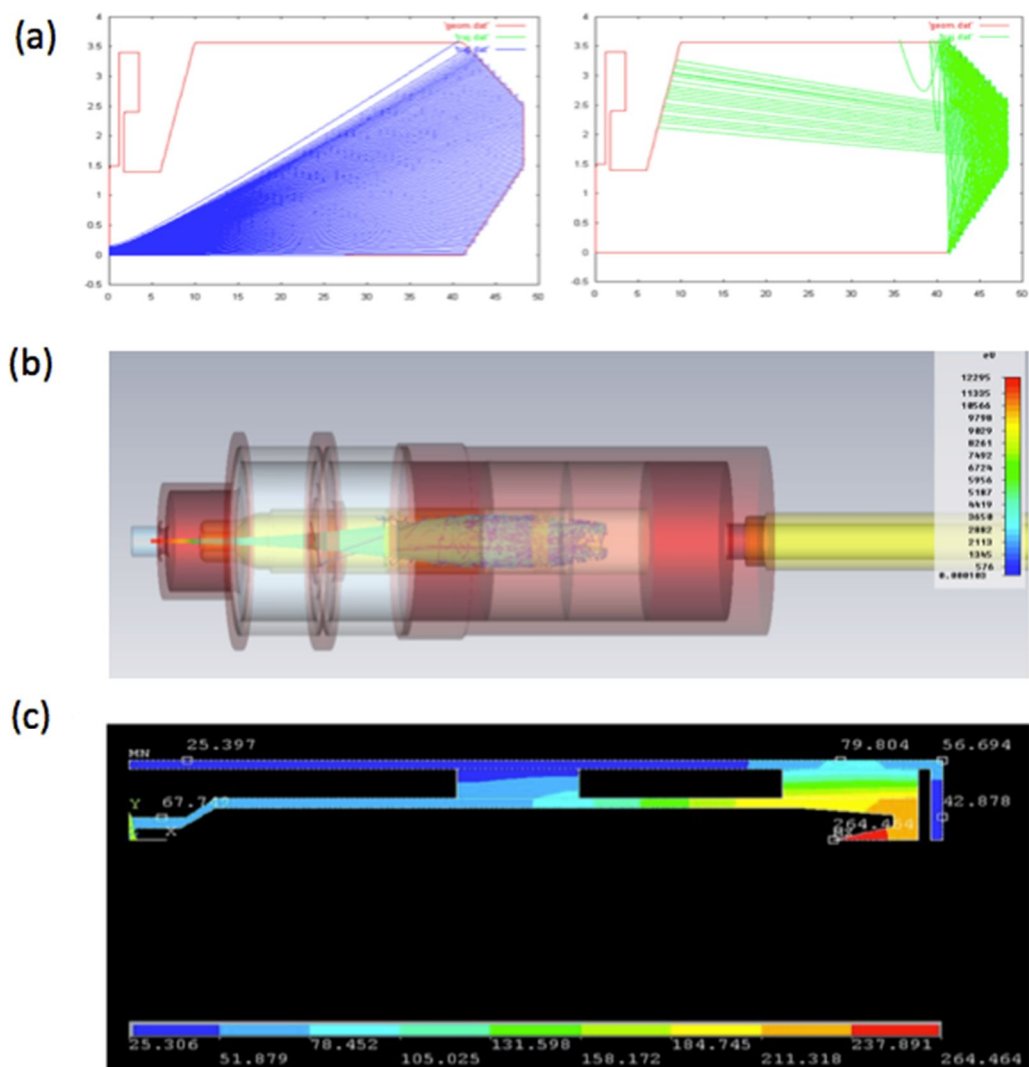


Fig. 2.50. (a) electron tracking simulation using EGUN, (b) CST particle studio, and (c) thermal analysis of -9kV depressed collector. Second plot in (a) represents secondary emission.

2.6.2. Fabrication of depressed collector

The mechanical design of the depressed collector is shown at Fig.2.51. Parts number 1 and 2 are electrically connected to the CCBWO circuit grounded and part 3, 6, 7, and 8 are located at -9kV region, whereas the others are grounded.

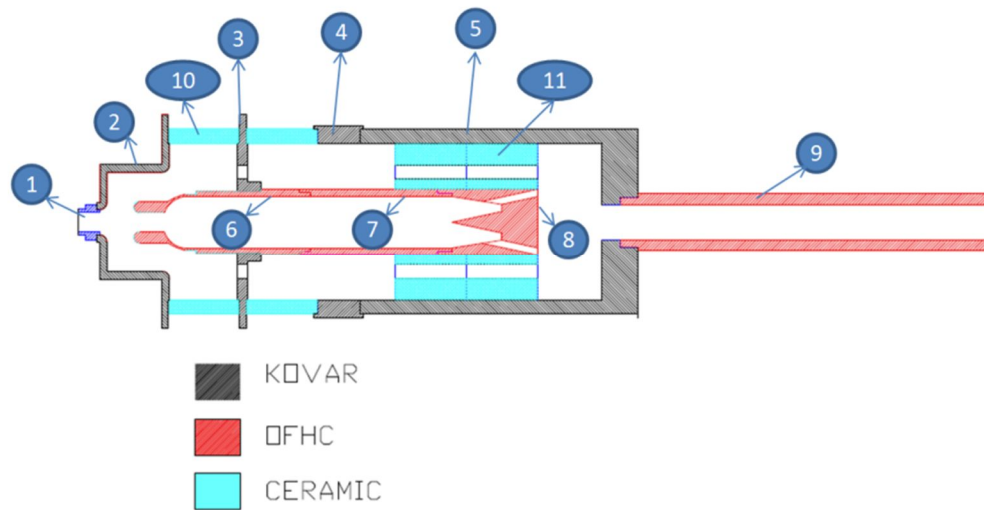


Fig. 2.51. Mechanical design of -9kV depressed collector



Outer part 1



Second flange



Outer part 1



Ceramic



First flange



Inner electrode

Fig. 2.52. Fabricated parts of depressed collector

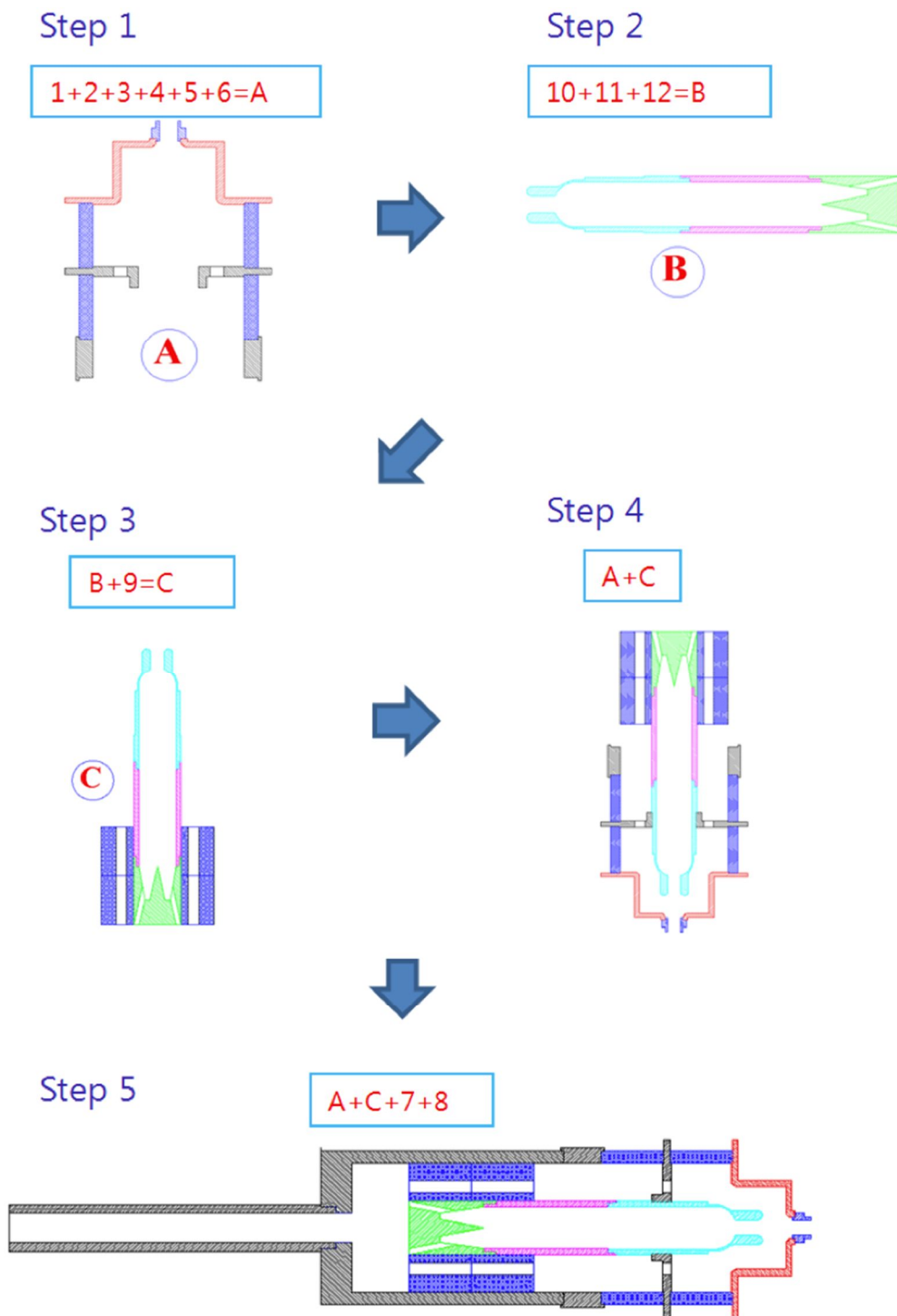


Fig. 2.53. Brazing step of -9kV depressed collector



Fig. 2.54. Completely brazed depressed collector

The brazing procedure is summarized as 3 steps shown at Fig.2.53. Outer parts of the collector and the inner parts should be brazed separately at first. Then all parts can be combined at one go. The finally brazed -9kV depressed collector is shown at Fig.2.54.

2.7. System assembly of 0.1THz CCBWO

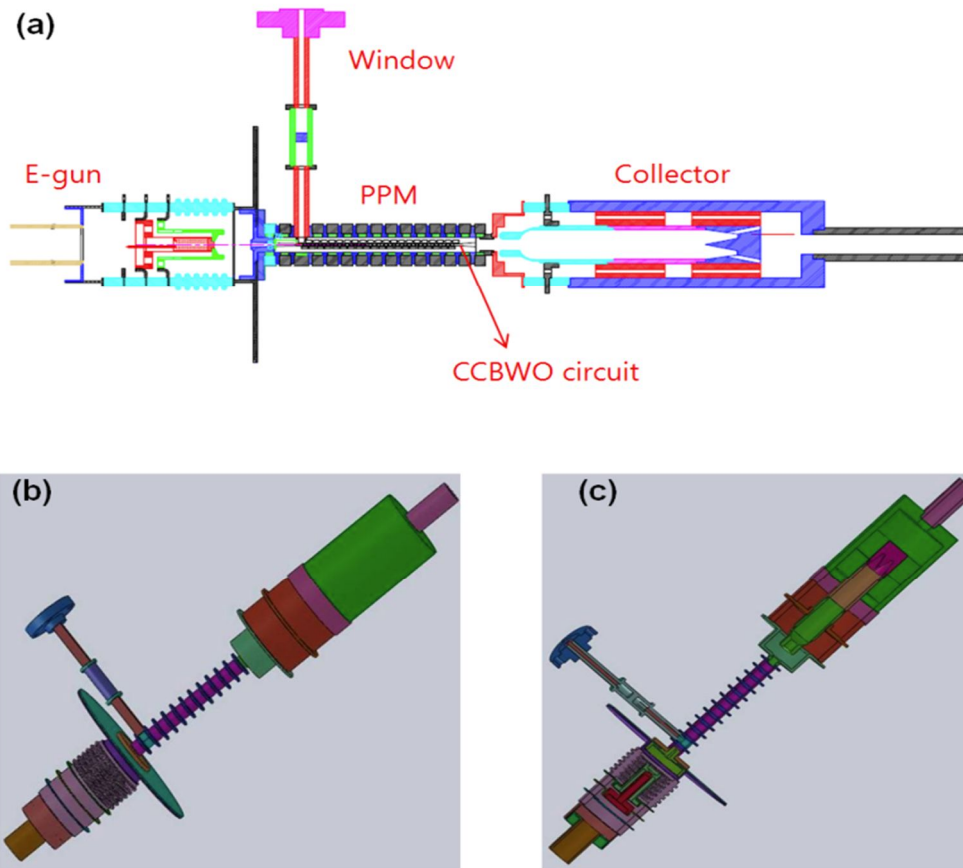


Fig. 2.55. Total assembly of 0.1THz CCBWO system



Fig. 2.56. Assembly of Circuit and PPM barrel

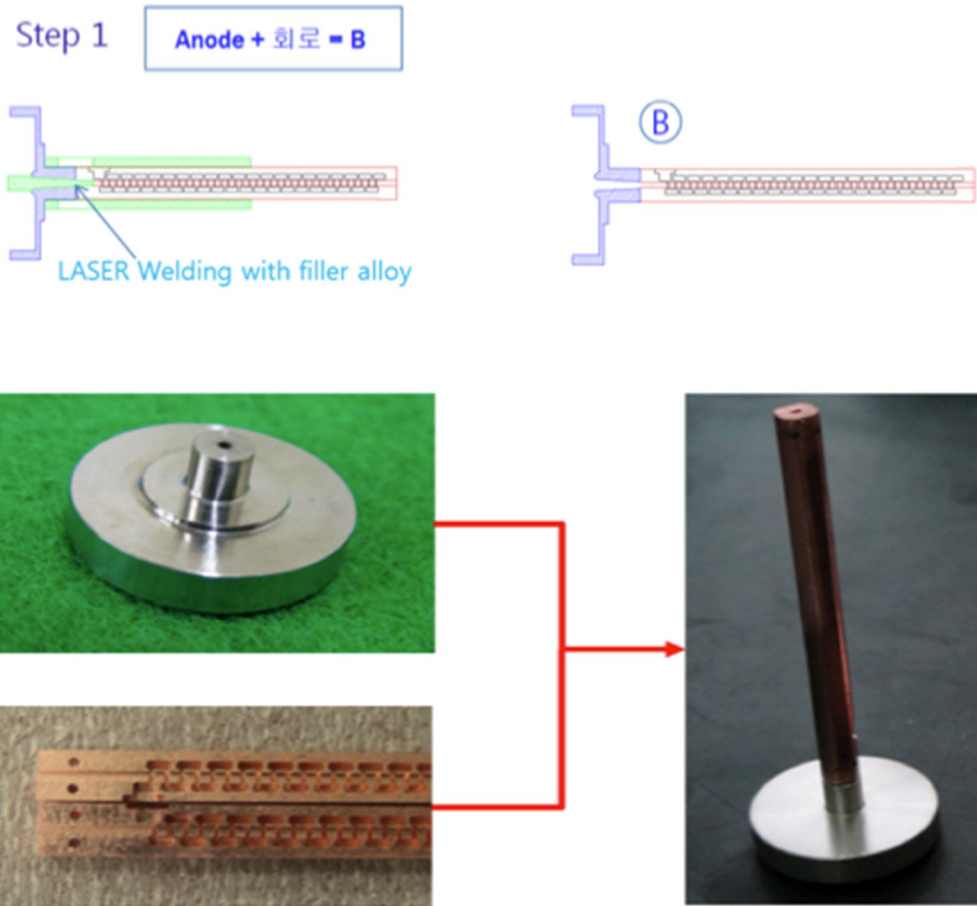


Fig. 2.57. Circuit and anode assembly

Step 2

Barrel + B + Anode seal = C

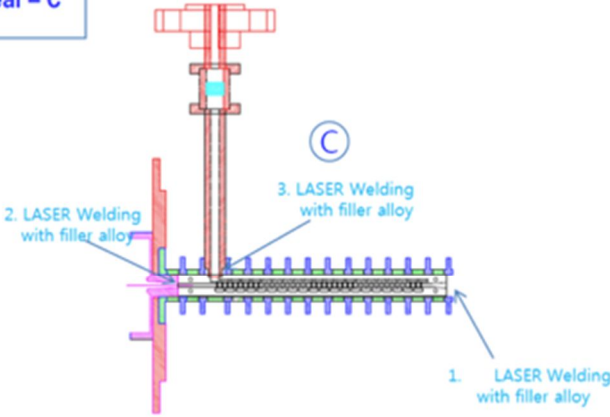
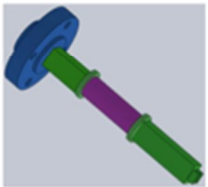


Fig. 2.58. Circuit and window assembly

Step 3

C + electron gun = D

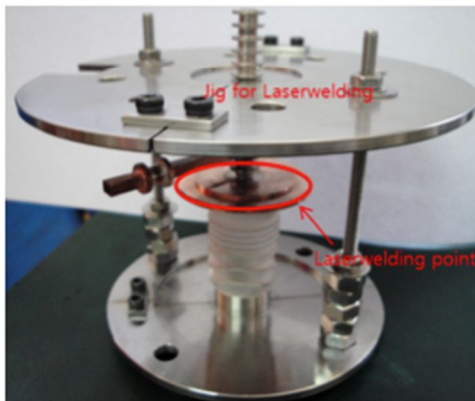
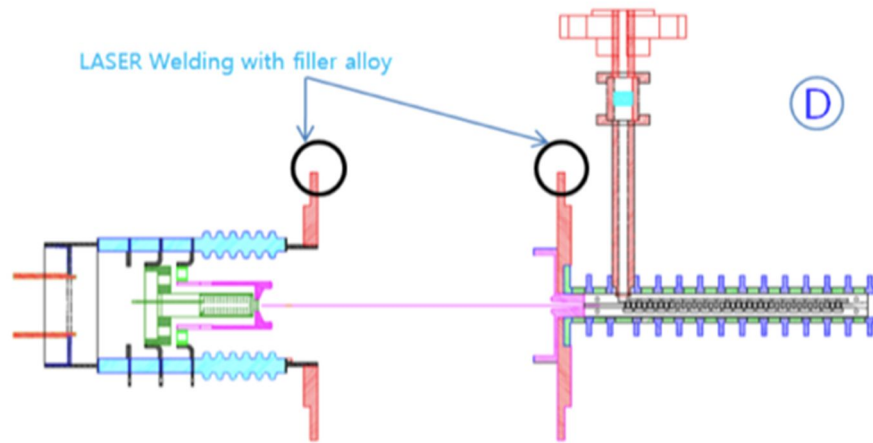


Fig. 2.59. Electron gun and circuit assembly

Step 4

D + Collector = E

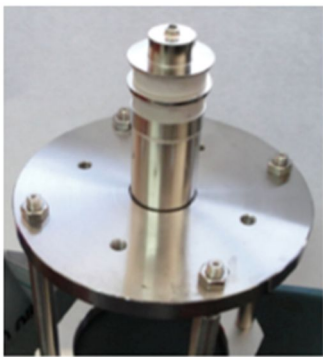
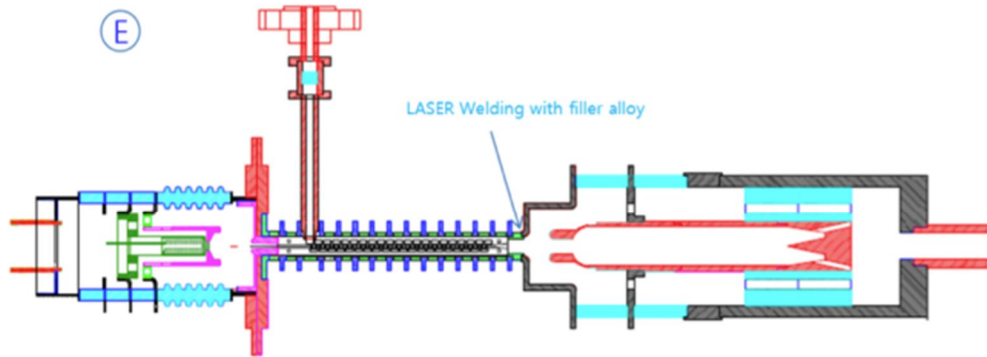


Fig. 2.60. Circuit and depressed collector assembly



CCBWO 본체

+



Ion Pump

=



Fig. 2.61. CCBWO body and ion pump connection

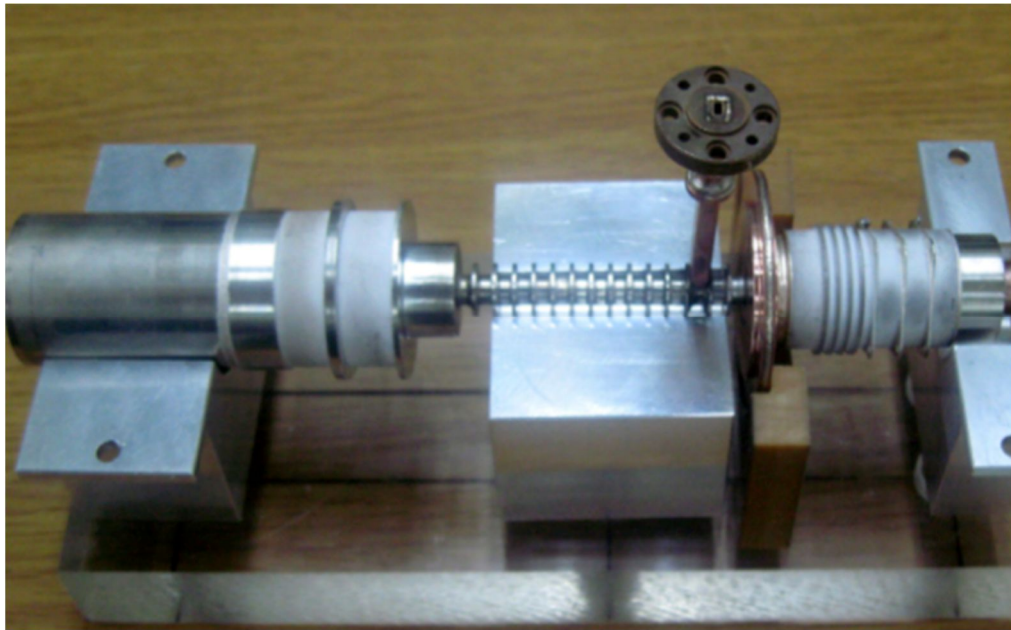


Fig. 2.62. Complete assembly of 0.1THz CCBWO

2.7.1. RF test of 0.1THz CCBWO

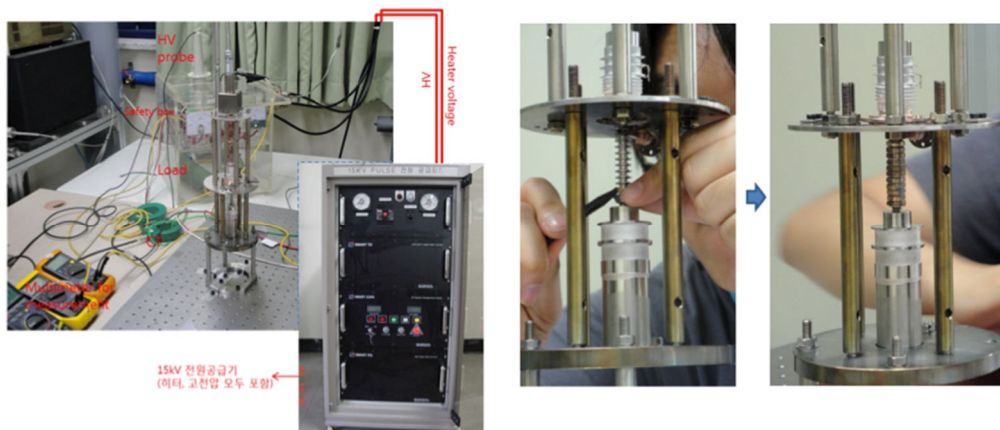


Fig. 2.63. Experimental setup for RF test

2.8. Conclusion

As a preliminary research on Terahertz VEDs, 0.1THz CCBWO system is developed. Applying both two step LIGA fabrication method and ultra-nano CNC machining, CCBWO circuits are fabricated precisely with less than 1 micrometer and the cold measurement excellently agree with FDTD numerical prediction. 12kV, 50mA electron guns is also designed and fabricated. Biasing 3V at BFE, 0.038 μ P is measured as we designed. PPM is fabricated as the focusing device of 0.1THz CCBWO. The experimental measurement is almost identical to the OPERA 3D simulation result. Wideband width of vacuum window is accomplished successfully and -9kV depressed collector is also manufactured well.

Whole 0.1THz CCBWO system is constructed and tested. Though minor leak occurs before RF test, all components of the system work well as designed even the beam test result match with design. Upgraded parts are prepared and will be assembled and tested.

Bibliography

- [1] D. B Lyon and A. J. Theiss, "Litton folded-waveguide high-power millimeter-wave TWTs," in Proc. IEDM 1994, pp. 918.
- [2] G. Dohler, D. Gallagher, and J. Richards, "Millimeter Wave Folded Waveguide TWTs," in Vac. Electronics Ann. Rev. Proc. 1993, pp. V.15.
- [3] G. Dohler, D. Gagne, D. Gallagher, and R Moats, "Serpentine Waveguide TWT," in Proc. IEDM 1987, pp. 485.
- [4] S. Bhattacharjee, J. H. Booske, C. L. Kory, D. W. van der Weide, S. Limbach, S. Gallagher, J. D. Welter, M. R. Lopez, R. M. Gilgenbach, R. L. Ives, M. E. Read, R. Divan, and D. C. Mancini, "Folded Waveguide Traveling-Wave Tube Sources for Terahertz Radiation," IEEE Trans. Plasma Sci., vol. 32, no. 3, pp. 1002-1014, June 2004.
- [5] L. Sadwick, R. J. Hwu, G. Scheitrum, "Microfabrication of vacuum compatible millimeter wave sources," in Proc. Int. Conf. Vac. Electronics 2003, pp. 360- 361.
- [6] Seong-Tae Han, Seok-Gy Jeon, Young-Min Shin, Kyu-Ha Jang, Jin-Kyu So, Jong-Hyun Kim, Suk-Sang Chang, and Gun-Sik Park, "Experimental Investigations on Miniaturized High-Frequency Vacuum Electron Devices," IEEE Trans. on Plasma Science, vol. 33, no. 2, pp. 679-684 (2005).
- [7] Seong-Tae Han, Kyu-Ha Jang, Jin-Kyu So, Jung-Il Kim, Young-Min Shin, Nikita M. Ryskin, Suk-Sang Chang, and Gun-Sik Park, "Low-voltage operation of Ka-band folded waveguide traveling wave tube", IEEE Trans. Plas. Sci. vol.33, no.1, pp.60-66.
- [8] CST Microwave studio. [Online]Available: <http://www.cst.com>

- [9] Bruce Goplen, Larry Ludeking, David Smith and Gary Warren, "User-configurable MAGIC for electromagnetic PIC calculations," *Comput. Phys. Commun.*, vol. 87, no1-2, pp. 54-86 (1995).
- [10] Young-Min Shin, "Study on high power millimeter/submillimeter wave generation from counter-streaming electron beams in two step LIGA fabricated circuits", Ph. D Thesis, Department of Phys., Seoul Nat'l Univ. (2006)
- [11] JR Pierce, "Rectilinear flow in electron beams", *J. Appl. Phys.* 11, 548 (1940).
- [12] OPERA 3D, copyright vector fields Inc., Oxford, UK [online]. Available: www.vectorfields.com
- [13] A. S. Gilmour, "Principle of Traveling Wave Tubes," chapter 6, Artech House, Boston, London, (1994).
- [14] Anurag Srivastava, "Experimental Study on High Current Density Electron Beams and its Interaction with Terahertz Wave in Micro-Fabricated Planar Coupled-Cavity Backward Wave Oscillator", Ph. D Thesis, Department of Physics & Astronomy, Seoul Nat'l Univ. (2010)
- [15] Gary B. Eastham, Kai Chang, "Analysis and closed-form solutions of circular and rectangular apertures in the transverse plane of a circular waveguide", *IEEE Trans. Micro. Tech.*, vol. 39, no. 4, pp. 718-723 (1991)
- [16] N. A. McDonald, "Simple approximations for the longitudinal magnetic polarizabilities of some small apertures", *IEEE Trans. Micro. Tech.*, vol. 36, no. 7, pp. 1141-1144 (1988)

Chapter 3.

Theoretical study on 0.22 THz sheet beam staggered Extended Interaction Oscillator (sEIO)

3.1. Introduction

Recently, Shin et al. suggested phase-shifted dual-vane arrays as a THz-amplifying circuit that excites the intense fundamental mode with symmetric longitudinal electric field components. [1-3] The one-dimensional grating structure used in their study offers the exact fabrication of the interaction circuits using a lithography-based micro-fabrication technique. Moreover, their phase-shifted double grating enlarges the effective range of the surface-confined modes so that the interaction area between the electron beam and the THz wave grows considerably compared to a circuit using a single grating, such as a backward wave oscillator (BWO). The strong beam wave interaction of these phase-shifted vane arrays is not only applicable to the amplification of THz waves with traveling waves but can also be adopted for THz oscillation based on standing-wave plasma coupling.

In this chapter, we suggest the design of a modified extended interaction oscillator (EIO) by adopting a half-period shifted double-grating resonator system. A finite-difference time-domain (FDTD) simulation and a particle-in-cell (PIC) simulation show

that the modified EIO is capable of interaction efficiency that exceeds 10% of at an operation frequency of 0.22 THz, whereas conventional types have interaction efficiency of less than 5%. Moreover, it is shown that the low aspect ratio of the circuit gap structure following from the TE mode-based interaction enables a shorter grating construction period, which lowers the operation voltage to 5 kV, whereas conventional EIOs operate at around 20 kV

3.2. Design of 0.22THz sEIO

3.2.1. sEIO – Powerfully modified EIO

The staggered EIO (sEIO) with half-period phase-shifted double-vane array structure is shown in Figs. 3.1(a) and 3.1(c). The main interaction region consists of double gratings at the top and bottom, but the top grating is shifted in the amount of a half period along the beam propagation direction. In each grating, vanes and gaps are arrayed with a period denoted by d , and the top and bottom gratings are separated by distance b . Two resonant cavities are located on each side of the beam tunnel to make the entire circuit a resonator with cavity width c and cavity height L . A rectangular beam tunnel with tunnel width l and tunnel height b is considered in the use of a sheet electron beam. The overall structure is similar to that of the Laddertron, a conventional type of sheet beam EIO, as shown at Figs. 3.1(b) and 3.1(d). [4] The main difference between these two types of EIOs is the symmetry between the top and bottom vane arrays. In the Laddertron, the symmetrically arrayed vanes on the top and bottom create multiple gaps in the middle of the two cavities. The gaps resonate with the same phase of the electric field in the circuit. As a result, the passing electrons experience high interaction with the longitudinal electric field at multiple gaps such that the coupling efficiency of the all

and the energy exchange between the electromagnetic wave and the electron beam becomes much stronger than those in a structure with a single resonating gap. However, unlike most other VEDs, the transverse magnetic (TM) mode of this double grating circuit is not the fundamental mode, at which the electric field is vertically polarized. In the fundamental mode, instead, the longitudinal field components arising at the surface of the gratings are distributed anti-symmetrically so that the field components in the beam propagation direction vanish in the beam-occupying region, as shown in Fig. 3.2(a). The higher order of TM mode has therefore been the only option for in-phase interaction between beam and wave in spite of the overmoded properties. The remarkable disadvantage when using the TM mode for sheet-beam types of VEDs is the

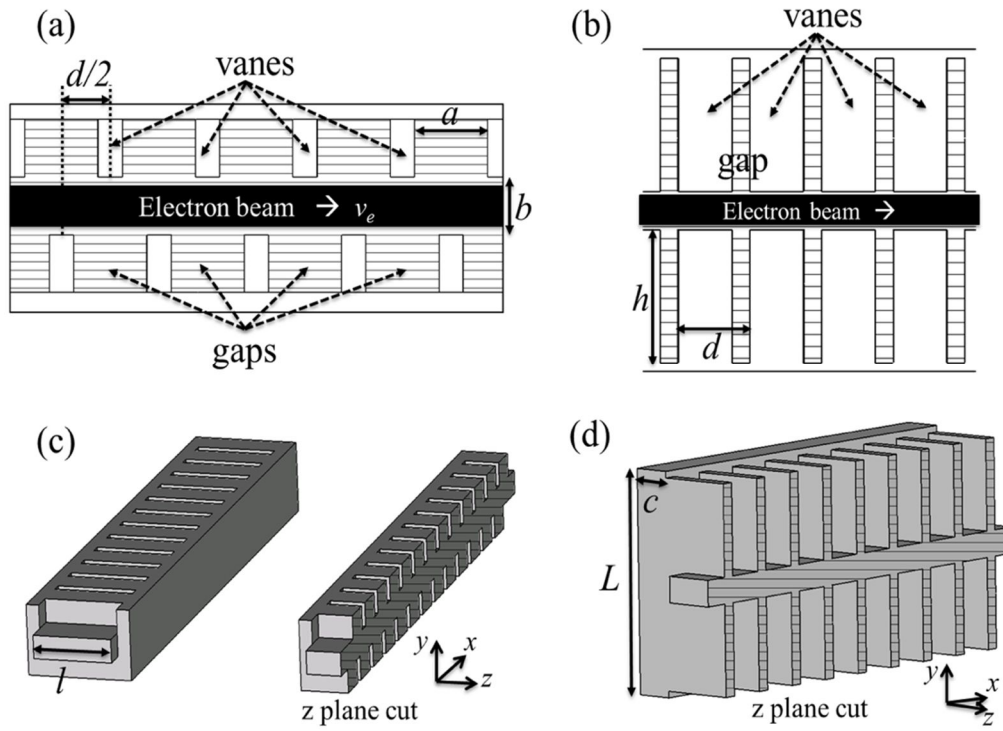


Fig. 3.1. Schematic side view of (a) the sEIO and (b) a conventional EIO, and the Laddertron and a comparison of the vacuum regions of (c) the sEIO and (d) the Laddertron.

undesirable transverse electric (TE) mode oscillation in a lower frequency band than that specified in the design. At least one TE mode exceeds the cutoff frequency of the circuit; thus, over certain amount of current, TE oscillation prevents the RF growth of the designed TM mode. [5-6] In contrast, the sEIO, shown in Fig.3.1(a), has a symmetric electric field along the beam propagation line, as shown in Figs. 3.2(b) and 3.2(d). A strong beam-acceleration field is distributed throughout the beam tunnel in the fundamental TE_{10} mode. Not only does the interaction intensity increase, but the risk of mode competition also vanishes in the circuit of the sEIO. The total circuit acts as a cavity with resonance in the TE_{10n} mode, where n is an integer. The frequency determination parameter in the result is the circuit width, and the effect of the circuit

height is negligible; i.e., the circuit height (or the grating depth) is freely controllable by the design scheme.

Another important benefit of the sEIO comes from this frequency independency of the grating depth. In general, the grating depth critically affects the frequency of grating-based VEDs in the operation of the TM mode. There exists a minimum limit of the depth between each vane. However, the sEIO works at a lower grating depth; therefore, as regards fabrication, the sEIO is much easier to realize the circuit working at the THz frequency. Table 1 shows the circuit dimensions of each EIO for the operation frequency of 0.22 THz. The grating period and the beam tunnel size are fixed to maintain the same input beam condition. The Laddertron has deeper gratings by fourfold, 2.5 times wider side cavities, and a wider gap by 1.5 times compared to those of the sEIO, whereas the gap length is three times shorter. Hence, a high aspect ratio of the grating structure of 7:1 is required, which inevitably demands a deeper etching technique. In general, increasing the grating period is recommended to avoid a grating circuit with a high aspect ratio. However, with an increase in the grating period, the necessary beam acceleration voltage increases for the beam-wave synchronization condition. Current EIOs and extended interaction klystrons (EIKs) have, therefore, a high electric potential of 15~30 kV and an aspect ratio feasible for the gap length; moreover, the aspect ratio for these devices are kept below 5:1, limited by the attainable gap depth. [7-8] In contrast, the sEIO can easily be designed so that it operates at a lower beam acceleration voltage because the frequency-dependence on the gap depth is not at all serious during operation in the TE mode. Though we consider a tenfold lower aspect ratio of 2:3 of the grating structure as compared to the Laddertron, the operation voltage can still be less than 6 kV, which is much lower than those of conventional EIOs.

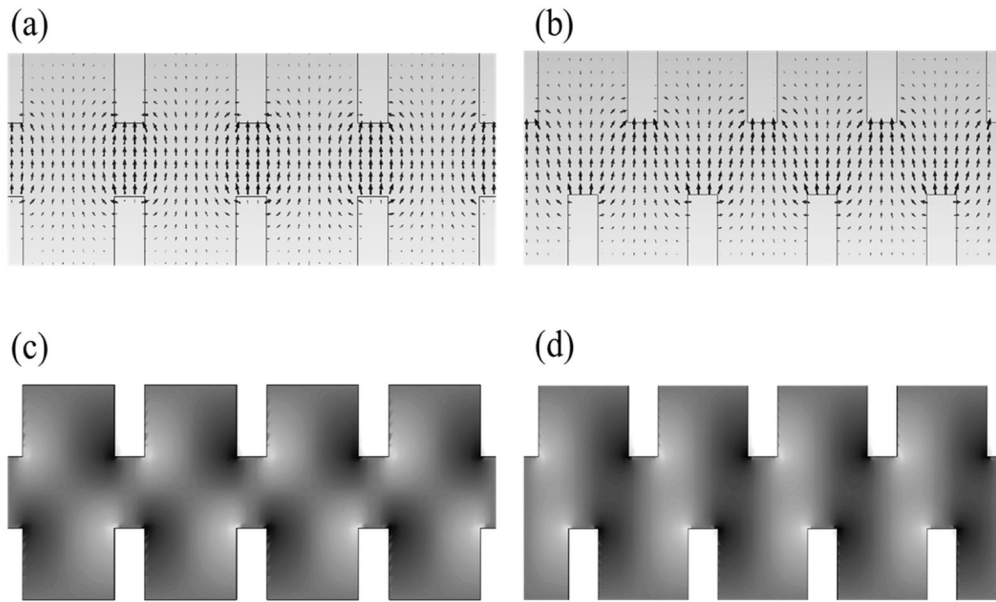


Fig. 3.2. 2D vector distribution of the E-field of the (a) Laddertron and (b) the sEIO, and 2D scalar distributions of E_z for the (c) the Laddertron, (d) the sEIO.

Table 3.1. Dimension parameters of 0.22 THz Laddertron and sEIO in μm .

	Laddertron	sEIO
Period	180	180
Gap length	45 (1/4 period)	135 (3/4 period)
Gap depth	350	90
Gap width	600	400
Beam tunnel	100×400	100×400
Side cavity height	1350	300
Side cavity width	150	65

3.3. Particle-In-Cell (PIC) numerical hot test

However, too low a voltage is not recommended to ensure a sufficient supply of energy considering the required output power of the THz source. We set the objective here of developing a 0.22 THz VED with output power that exceeds 100 W with efficiency of more than 15%, and with an operation voltage of less than 6 kV. A sheet electron beam $80\mu\text{m}\times 360\mu\text{m}$ in size is applied with a current of 140 mA.

First, the dispersion relation of the sEIO is studied to predict the sEIO properties. Fig. 3.3(a) shows a dispersion diagram of the 0.22 THz sEIO. From the synchronization condition, $k_e = k_x$, where k_e is the wavenumber of the electron and k_x is the longitudinal wavenumber of the wave at the circuit. In this condition, $k_e = \omega/v_e$ and $k_x = k_0 \pm 2n\pi/d$, where $\omega = 2\pi f$ is the angular frequency, v_e is the velocity of the electron beam, k_0 is the wavenumber at an acute angle with respect to the operating mode and the integer m is a spatial harmonic number. The dimensional parameters are obtained from the 2π -mode operation which I define as the operation when $k_0 = 0$. The period is determined to be $180\ \mu\text{m}$ from the dispersion relation to synchronize with an electron beam of 5 keV and the calculated parameters are identical to the results of the sEIO shown in Table 1. The relationship between the wavenumber (k_0) and the frequency (f) is found by an analytical calculation as well as a FDTD simulation using CST Microwave Studio. [7] Eigenmode solver is used with the periodic boundary condition at longitudinal direction and with perfect electric conducting boundary at others. The resonance frequencies are observed while varying the phase of the unit period to obtain the dispersion. One important benefit of the sEIO is the lower possibility of mode competition in spite of the use of a sheet electron beam. A sEIO operates in the fundamental mode, and the frequency coverage of the mode is nearly 0.3 THz. The minimum frequency of the next mode is thus very far away from the designated mode. However, under a realistic condition, the sEIO is an oscillator that applies a standing wave with a relatively small periodic

number. The dispersion relation can consequently exist in a discrete condition and the group velocity of each point becomes 0, as the group velocity of the 2π -mode. Therefore, competition not with a higher-order mode but with a special harmonic of a mode with the same order occurs. To minimize this destructive competition, the frequency difference of each discrete mode should be sufficiently large. The number of discrete operation points is determined from the number of gaps N ; i.e., more periods result in more modes. Several modes starting from the condition of are shown in Fig. 3.3(b) when $N = 9$ and 17. While four modes are available when $N = 9$, seven modes can be excited when $N = 17$ in the frequency range from 0.22 THz to 0.33 THz. The inset of Fig. 3.3(b) shows that the frequency difference of each mode decreases with an increase in the number of gaps, N .

The parameter most strongly affected by the discrete frequency gap is the range of the operation voltage. The realistic operation modes are the lowest order of those discrete modes near $k_x = 2\pi/d$, and the wavenumbers of those modes are slightly translated both negatively and positively via $\Delta k_x \sim 2\pi/Nd$. If the operation voltage falls within this wavenumber range, stable excitation of this desired mode is possible. In Fig. 3.4(a), it is explained that the available voltage range when is nearly twice that when $N = 17$. In detail, the available voltage range is inversely proportional to the number of gaps, as shown in the histogram in Fig. 3.4(b). Thus, the smaller the number of the gaps, the better the mode concentration. The number of gaps N is, however, critically related to the shunt impedance R/Q , which is the figure of merit of the resonant structure doing work on the electron beam. In general, the shunt impedance R/Q is defined as [8]

$$R/Q = \frac{\left(\int_{-\infty}^{\infty} |E_x| dx \right)^2}{2\omega U}, \quad (3.1)$$

where E_x is the electric field in the beam propagation direction, ω is the angular frequency, and U is the stored energy in the resonator. As expressed by Eq. (3.1), the shunt impedance would increase as the circuit length - proportional to number of gaps - increases. Thus, N should at least be larger than a certain value to induce high interaction between the electron and the THz wave. The output power and interaction efficiency with respect to the number of gaps N is analyzed using a PIC simulation code - MAGIC 3D under the condition discussed in the beginning of this section. [9] As shown in Fig. 3.5(a), the THz wave will oscillate over at least seven gaps, and the output power and interaction efficiency both increase as N increases, whereas the interaction falls off when the number of gaps exceeds 17. Conclusively, insufficient shunt impedance causes a lower limit, but the higher limit results from mode competition as the acceleration voltage surpasses the available voltage range.

A similar tendency is observed for the voltage sweep. It starts to show THz oscillation over a threshold acceleration voltage of 4.1 kV, and the output power and the efficiency drastically increase until a sudden drop occurs at a voltage level of 5.2 kV, as shown in Fig. 3.5(b). The phase spaces in Fig. 3.5(c) explain the behavior of the electron beam when out of the available voltage range. The electron beam is bunched at the beginning of the circuit and is released nearly at the center dissipating energy, after which it is bunched again at the end of the circuit, i.e., mode competition with a spatial harmonic prevents the desired mode excitation. The FFT result in the circuit center region is shown in Fig. 3.5(d) confirming the existence of complex mode competition by the various peaks near 0.25 THz, 0.29 THz, and 0.33 THz, for instance, which are the exact frequencies of the spatial harmonics when $m = 1, 2,$ and $3,$ respectively. Therefore, the chosen number of gaps and the operation voltage should be within the available region to avoid the unnecessary, but critical, mode competition.

Other parameters that affect the performance of the sEIO are described in Fig. 3.6. The current can be an issue, as we set a lower operation voltage but high output

power. In the sEIO, however, the high efficiency caused by the strong longitudinal field formation enables higher power of the EIO with the same or less current. As shown in Fig. 3.6(a), it starts to oscillate at 40 mA; the interaction efficiency exceeds 15% before the current value reaches 100 mA. Output power of 200 W is possible at a current of 300 mA. The external Q is also important because it determines the coupling efficiency of THz radiation from the circuit. From the definition of the quality factor $Q = \omega U/P$, the energy generated from plasma-THz wave coupling is slightly larger than the out-coupled energy at the coupler located at the center of the side cavity in an optimum condition. Fig. 3.6(b) illustrates the tendency of the output power with respect to the external Q factor controlled by the coupler size change. Before the incident drop, the performance is maximized, as it is with respect to the number of gaps.

The optimized sEIO design is finalized with these parameters for a 90% condition relative to the maximum performance, considering stable operation. The synthesized performance is summarized in Table 3.2 and in Fig. 3.7. It is well seen that the strong bunching is formed at the center of the circuit and that stable desired mode is interacting with the electron beam from the phase spaces as seen in Fig. 3.7(a) that contrasts the results of Fig. 3.5(c). A sheet electron beam with the aspect ratio of 1:4 at the beam current 140 mA is accelerated with a voltage 5.2 kV and an output power of 122 W with efficiency of 16.5% operating at the frequency 0.217 THz is achieved as seen at Fig. 3.7(b). This output power is virtually 100 times greater than those of existing 0.22 THz EIOs and 2-3 times, than similar frequency of EIKs. Moreover, the interaction efficiency of the sEIO is 3~10 times larger than them with approximately 25% of the acceleration voltage. The designed gap depth of the circuit is 100 μm , which is only half of the period, and the gap length is 150 μm , three quarter of the period. Therefore, the aspect ratio of each gap is less than 1:1, which consequently leads to easier fabrication than previously designed EIO with deeper gaps and a higher aspect ratio of the circuit structure.

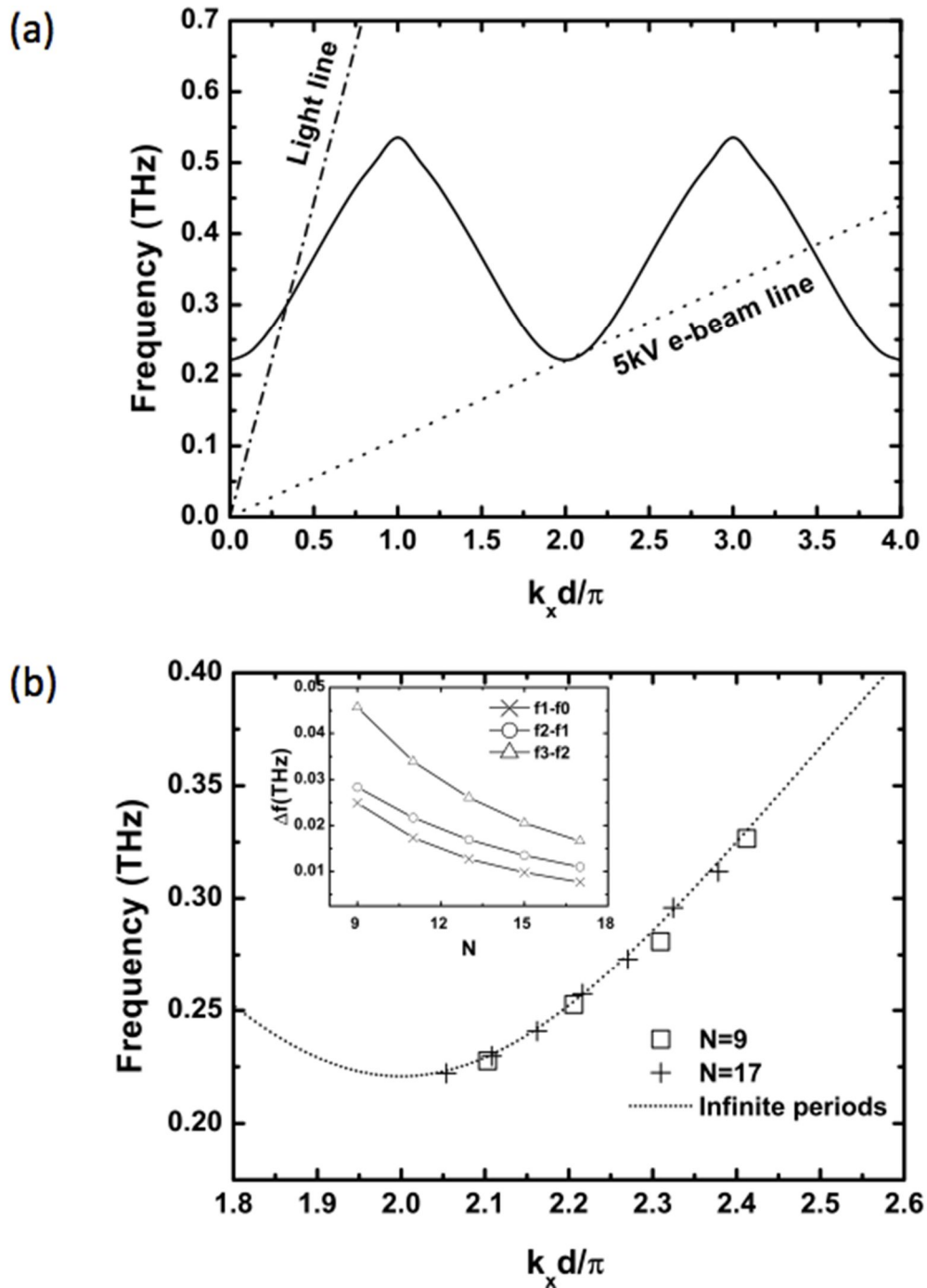


Fig. 3.3. (a) Dispersion diagram of the sEIO and (b) discrete dispersions at first three

orders. The inset denotes the frequency difference between each mode with respect to the number of periods.

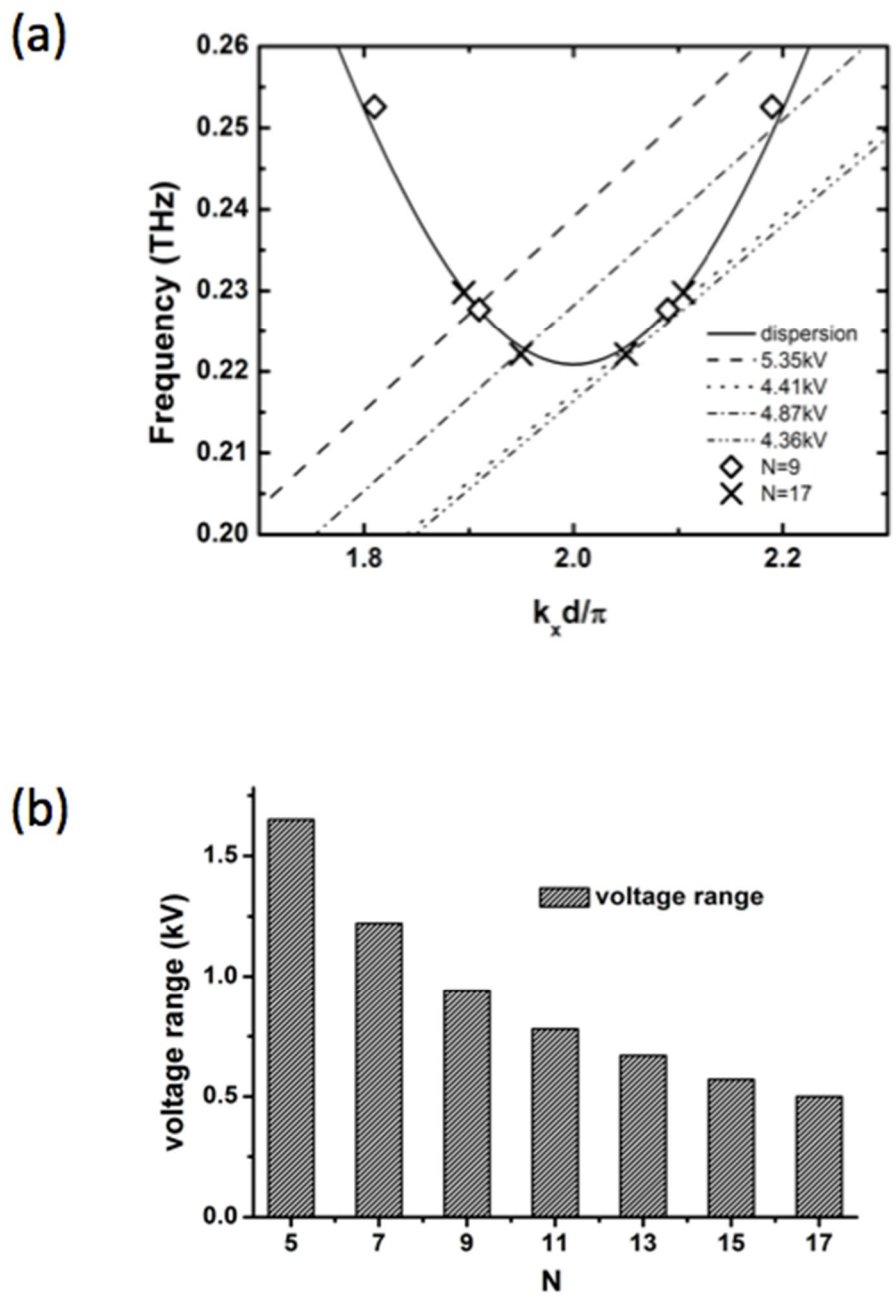


Fig. 3.4. (a) Beam lines and dispersion relation at $N = 9$ and 17 to sync at the zeroth order mode of the sEIO, and (b) the subsequent available voltage range with respect to the number of gaps N .

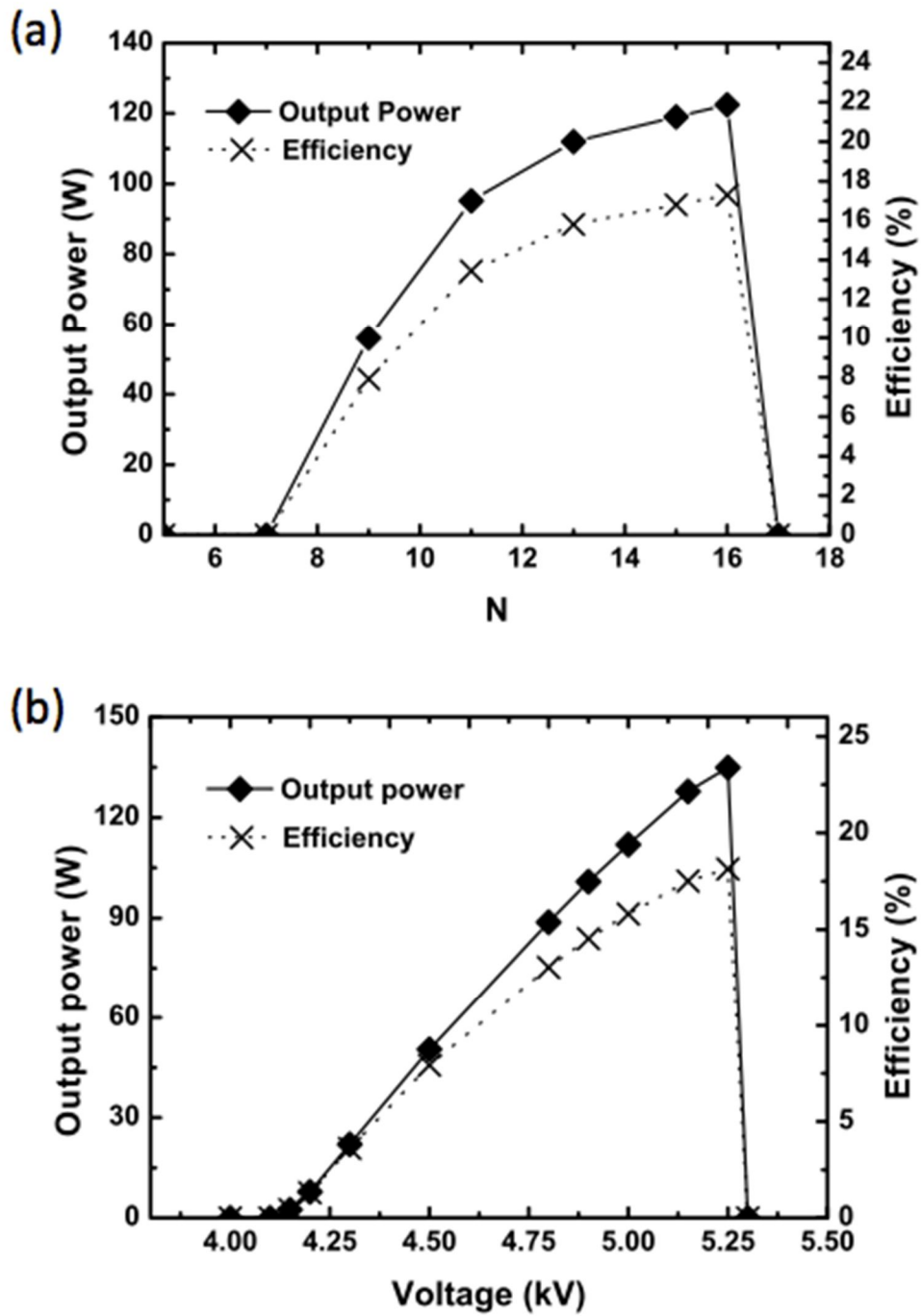


Fig. 3.5. Output power and interaction efficiency of the 0.22 THz sEIO with respect to (a) the number of gaps N, (b) the beam acceleration voltage

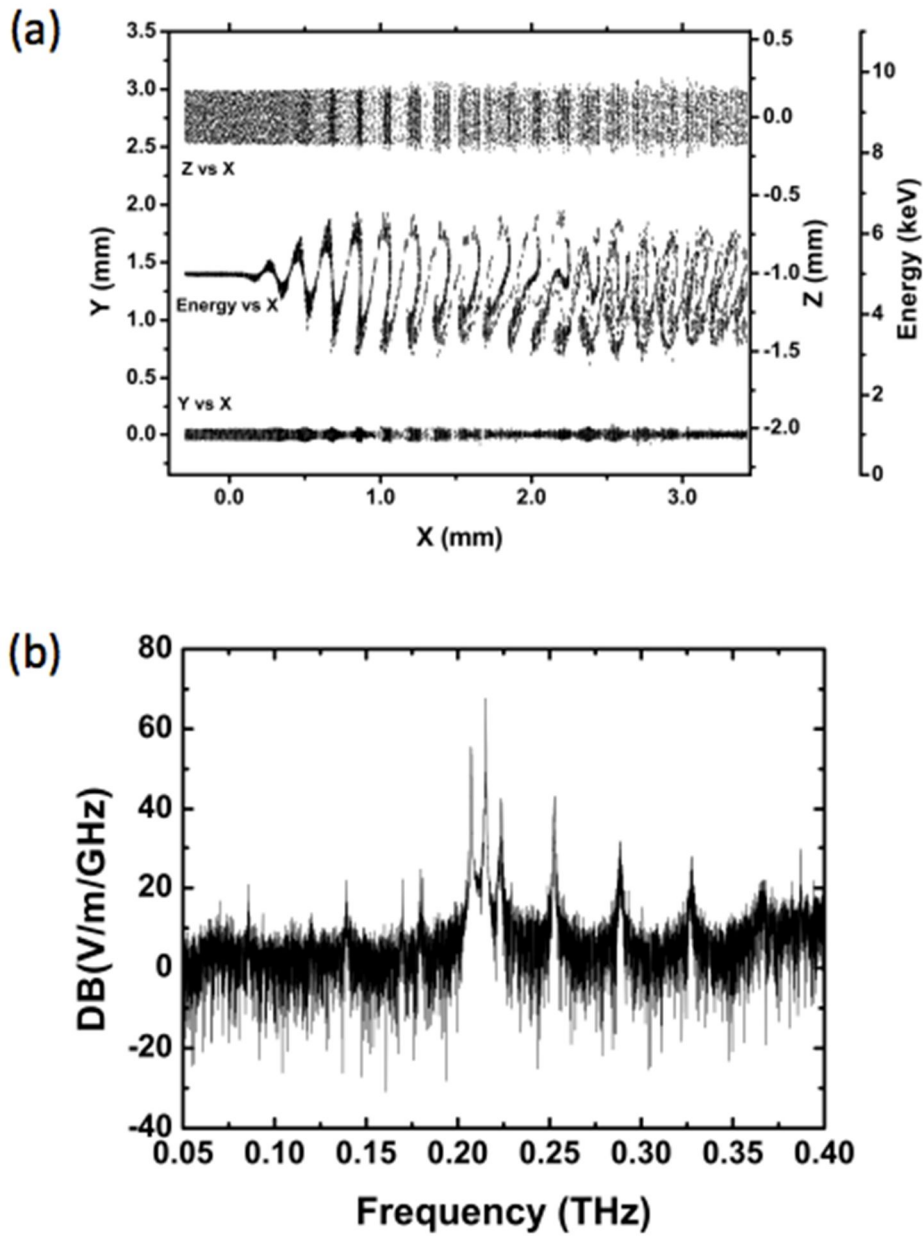


Fig. 3.6. (a) the phase spaces: Z vs X (top), energy vs X (middle), Y vs X (bottom), and (b) FFT results at $N=17$, $V=5.2$ kV analyzed using PIC code MAGIC 3D.

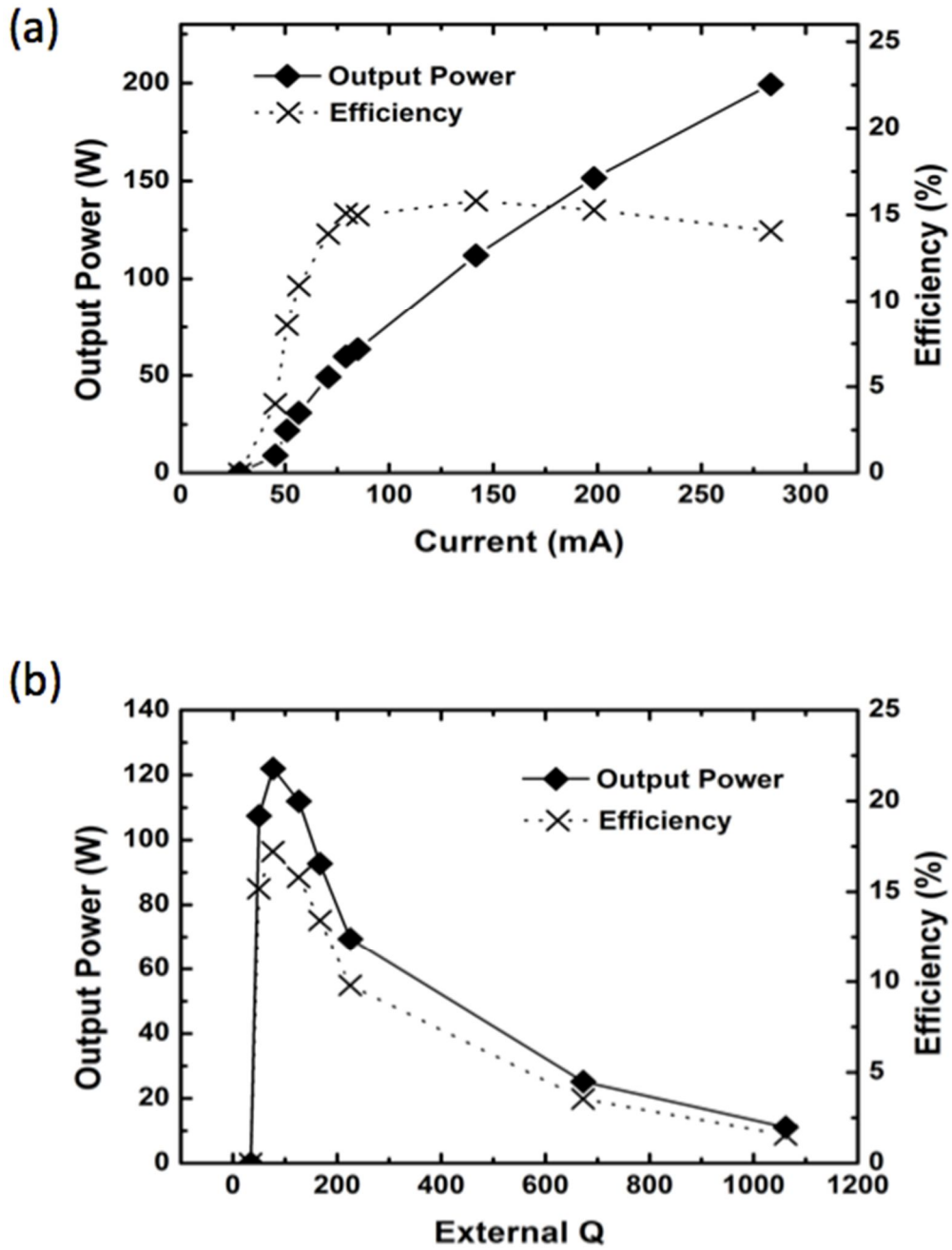


Fig. 3.7. Parametric analysis of the output power and interaction efficiency of the 0.22THz sEIO with respect to (a) the beam current and (b) the external Q factor.

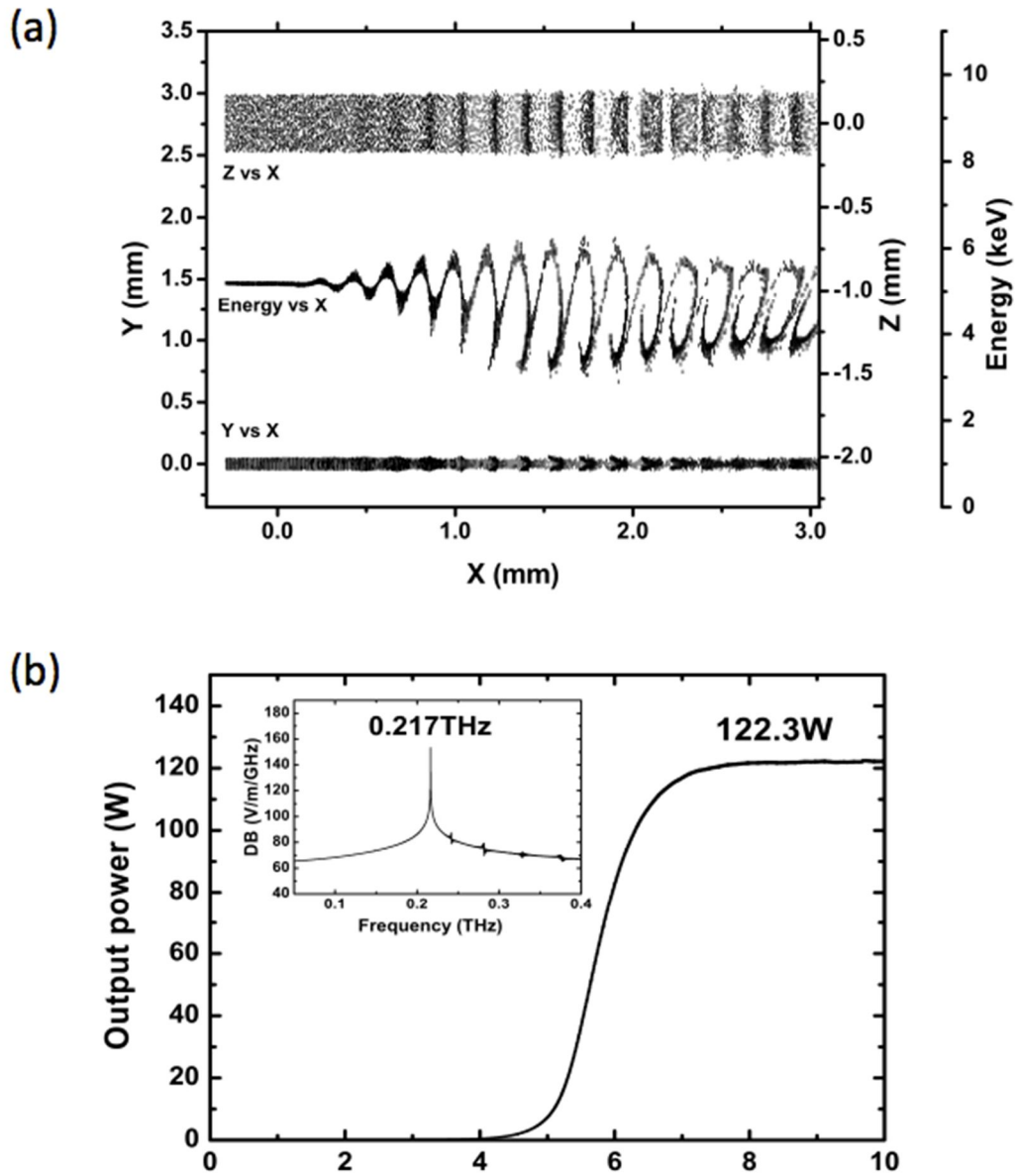


Fig. 3.8. Electron beam and THz coupling of the finalized 0.22 THz sEIO as obtained from the MAGIC 3D simulation: (a) phase space of Z vs X (top), energy vs X (middle), Y vs X (bottom), and (b) field power versus time with the inset showing the FFT result

3.4. Conclusion

High-efficiency THz oscillation is achieved with phase-shifted double-vane arrays as a resonator. The phase shift enables the use of the fundamental TE mode as an operation mode with a strong and periodic longitudinal electric field component by the coupling of surface modes from differently staggered double gratings in the π phase. The fundamental mode operation results in higher interaction intensity of plasma-THz wave coupling, and the TE-mode operation removes the high aspect ratio of the circuit fabrication condition, resulting in easier fabrication of the circuit as well as low voltage operation for THz generation using convection electrons. The PIC code reveals that the sEIO has output power of over 100 W and interaction efficiency that exceeds 15% at an acceleration voltage of only 5 kV. Thus, the sEIO has 3~100 times greater output power and 3~10 times higher interaction efficiency with 3-4 times less voltage compared to conventional EIO devices.

Bibliography

- [1] Y. Shin, and L. Barnett: Proc IEEE Int. Vacuum Electronics Conf. 2008, p.54.
- [2] Y. Shin, and L.R. Barnett: Appl. Phys. Lett. **92** (2008) 091501.
- [3] Y. Shin, A. Baig, L.R. Barnett, N.C. Luhmann, J. Pasour, and P. Larsen: Proc. IEEE Trans. Electron Devices **58** (2011) 3213.
- [4] K. Fujisawa: IEEE Trans. Electron Devices **11** (1964) 381.
- [5] D. Yu, and P. Wilson: Proc. IEEE Particle Accelerator Conf. 1993, p. 2681.
- [6] G. Scheitrum, G. Caryotakis, A. Burke, A. Jensen, E. Jongewaard, M. Neubauer, R. Phillips, and R. Steele: Proc. IEEE Int. Vacuum Electron Sources, 2006: p. 481.
- [7] CST Studio Suite 2008 [<http://www.cst.com>].
- [8] G. Caryotakis: SLAC-PUB-10620 (2005), 1.
- [9] B. Goplen, L. Ludeking, D. Smithe, and G. Warren: Comput. Phys. Commun. **87** (1995) 54

Chapter 4

Conclusion

In this dissertation, 0.1 THz coupled cavities backward wave oscillator (CCBWO) is proposed and studied as preliminary research on terahertz VEDs, applying two-step LIGA as well as ultra nano CNC machining. The circuits are fabricated with less tolerance than a micron and the cold measurements are in excellent agreement with numerical simulation. All other components of the 0.1THz CCBWO system such as 12kV, 50mA electron gun, 2800gauss of PPM, 8% of band center frequency transmitting vacuum window, and -9kV depressed collector are designed, fabricated, and experimented and all the results match strongly to the design. All parts are assembled together and with the bias voltage at beam focusing electrode, desired perveance is observed in the beam test.

0.22THz staggered extended interaction oscillator is also investigated, focusing on the strong interaction even with relatively low voltage. In the half π phase shifted double grating resonator, The large fraction of the fundamental TE mode is longitudinally polarized, and it excites the intense plasma-terahertz wave coupling at the shallow grating, which enables highly efficient RF generation at a relatively low operating voltage. A particle-in-cell (PIC) simulation predicts that the half-period phase-staggered grating resonator generates 0.22 THz wave with output power exceeding 100 W and interaction efficiency of more than 15 % at a low beam acceleration voltage of 5.2 kV

List of Publications

1. Matlabjon Sattorov, **Ohjoon Kwon**, et al., “Thermal analysis of a strapped magnetron”, IEEE Trans. Elec. Dev. 58, p2784 (201)
2. Ranjan K. Barik, **Ohjoon Kwon**, et al., “A novel approach to synthesis of Scandia-doped tungsten nano-particles for high-current-density cathode applications”, Int. J. Ref. Met. HM, 38 (2013)
3. Ranjan K. Barik, **Ohjoon Kwon**, et al., “Development of alloy-film coated dispenser cathode for terahertz vacuum electron devices application”, App. Surf. Sci. 276, 1 (2013)
4. Matlabjon Sattorov, **Ohjoon Kwon**, et al., “Improved efficiency of backward-wave oscillator with an inclined electron beam”, IEEE Trans. Elec. Dev. 60, p458 (2013)
5. Anirban Bera,, **Ohjoon Kwon**, et al., “Surface-coupling of Cerenkov radiation from a modified metallic metamaterial slab via Brillouin-band folding”, Opt. Exp. 22 (2014)
6. **Ohjoon Kwon**, et al., “Efficient terahertz oscillation using a half-period staggered grating resonator”, JJAP 53, 066201 (2014)
7. Matlabjon Sattorov, **Ohjoon Kwon**, et al., “Automodulation Processes in Clinotrons With Low-Focusing Magnetic Field”, IEEE Trans. Elec. Dev. 62, p1617 (2015)
8. Eduard Khutoryan, **Ohjoon Kwon**, et al., “Theory of Multimode Resonant Backward-Wave Oscillator With an Inclined Electron Beam”, IEEE Trans. Elec. Dev. 62, p1628 (2015)
9. Sun-Hong Min, **Ohjoon Kwon**, et al., “Characteristics of a transient axial mode from the formation of anode plasma in a gigawatt-class L-band magnetically insulated transmission line oscillator (MILO)”, Phys. Plas. 23, 063120 (2016)
10. **Ohjoon Kwon**, et al., “Wide Bandwidth of Anti-Reflective Window for Terahertz Vacuum Electronic Devices”, IEEE. Trans. THz. Sci. Tech. (on process)

International Conference proceedings and abstracts (46)

1. S. Kim, I.-K. Baek, **O. Kwon**, A. Bera, R. Bhattacharya, M. Sattorov, S.-H. Min, G.-S. Park. "Enhanced radiation in a modified metallic metamaterial driven by pre-bunched electrons." In Proc. IVEC, Beijing, China, April 27-29, 2015.
2. R. Bhattacharya, I.-K. Baek, J. S. Lee, R. K. Barik, S. Kim, D. Hong, **O. Kwon**, M. Sattorov, Y. H. Kim, G.-S. Park. "Investigation of emission capability of reduced graphene oxide film cathode for terahertz vacuum electron devices." in *Proc. 40th Int. Conf. IRMMW-THz*, Hong Kong, China, Aug. 23-28, 2015.
3. S. Kim, I.-K. Baek, **O. Kwon**, A. Bera, R. Bhattacharya, M. Sattorov, S.-H. Min, G.-S. Park. "Electromagnetic field enhancement in metallic metamaterials: a potential for compact terahertz free-electron lasers." in *Proc. 40th Int. Conf. IRMMW-THz*, Hong Kong, China, Aug. 23-28, 2015.
4. R. Bhattacharya, I. K. Baek, J. S. Lee, S. Kim, A. Kumar, O. Kwon, S.-H. Min, A. Bera, R. K. Barik, **M. Sattorov**, and G.-S. Park. "Calculation of thermal transport of heat due to field emission current inside a reduced grapheme oxide film. in *Proc. 6th Int. THz-Bio Workshop*, April 9-10, 2015, SNU, Seoul, Korea, p. P-15
5. M. Sattorov, **K. Ohjoon**, M. Sun-Hong, P. Gun-Sik, G. Scheitrum, M. P. Perkins, *et al.*, "Suppression of TE mode oscillation in PPM-focused S-band sheet beam klystrons," in *Vacuum Electronics Conference, IEEE International*, 2014, pp. 25-26.
6. A. Bera, M. A. Sattorov, **O. J. Kwon**, R. K. Barik, S. H. Min, and G. S. Park, "Cherenkov-like radiation from metallic metamaterials," in *Vacuum Electronics Conference (IVEC), 2013 IEEE 14th International*, 2013, pp. 1-2.
7. **O. Kwon**, M. A. Sattorov, *et al.*, "Development on sub-THz vacuum electronic devices (VEDs)", in *Vacuum Electronics Conference, IEEE International*, 2013
8. S. H. Min, **O. Kwon**, *et al.*, "Power Estimation of Electromagnetic Coupling Effectiveness by a X-band Backward Wave Oscillator with Mode Conversion", 14th IEEE International Vacuum Electronics Conference, 2013
9. R. K. Barik, A. Bera, A. K. Tanwar, I. K. Baek, K. Eom, M. A. Sattorov, **O. J. Kwon**, *et al.*, "Sol-gel synthesis of Sc₂O₃ doped W nano-particle for cathode application," in *Vacuum Electronics Conference (IVEC), 2013 IEEE 14th International*, 2013, pp. 1-2.
10. M. Sattorov, **Ohjoon Kwon**, *et al.*, "325 MHz superconducting spoke cavity design for RISP." in *Proc. ICABU*, Daejeon, South Korea, Nov. 11-13, 2013
11. K. Seontae, **K. Ohjoon**, B. In-Keun, E. Kihoon, A. Bera, M. Sun-Hong, *et al.*, "Bending transmission of human hair at terahertz frequency regime," in *Infrared*,

- Millimeter, and Terahertz Waves (IRMMW-THz), 2012 37th International Conference on*, 2012, pp. 1-2.
12. M. Sattorov, **O. Kwon**, S.-H. Min, I.-K. Baek, and G.-S. Park, "EM Design of superconducting cavities for RISP." in Proc. Inf. Conf. ICABU (Int. Conf. on Accelerators and Beam Utilizations), Gyeongju, South Korea, Nov. 8-9, 2012.
 13. R. K. Barik, A. K. Tanwar, I. K. Baek, E. Kihoon, A. Bera, M. A. Sattorov, **O. J. Kwon**, *et al.*, "Effect of surface roughness of high current density nano-particle cathode for terahertz vacuum devices application," in *Vacuum Electronics Conference (IVEC), 2012 IEEE Thirteenth International*, 2012, pp. 369-370.
 14. M. Sattorov, E. Khutoryan, K. Lukin, P. Gun-Sik, A. Bera, R. Barik, **K. Ohjoon**, *et al.*, "Experimental study on 0.1 THz Clinotron," in *Vacuum Electronics Conference (IVEC), 2012 IEEE Thirteenth International*, 2012, pp. 453-454.
 15. M. A. Sattorov, E. Khutoryan, K. Lukin, G. S. Park, and **O. Kwon**, "Automodulation processes in THz resonant backward wave oscillator with low focusing magnetic field," in *Infrared, Millimeter, and Terahertz Waves (IRMMW-THz), 2012 37th International Conference on*, 2012, pp. 1-2.
 16. R. K. Barik, A. K. Tanwar, I. K. Baek, K. Eom, A. Bera, M. A. Sattorov, **K. Ohjoon**, *et al.*, "Study of dispenser cathode development for terahertz vacuum devices application," in *Infrared, Millimeter, and Terahertz Waves (IRMMW-THz), 2012 37th International Conference on*, 2012, pp. 1-3.
 17. Matlabjon Sattorov, Eduard Khutoryan, Konstantin Lukin, Gun-Sik Park, Anirban Bera, Ranjan Barik, **Ohjoon Kwon**, Sun-Hong Min, Ashok Sharma, Anil Tanwar. "Experimental study on 0.1 THz Clinotron". IEEE IVEC-IVESC 2012
 18. A. Bera, R. K. Barik, M. Sun-Hong, **O. Kwon**, B. InKuen, K. Seontae, *et al.*, "Enhanced Smith-Purcell radiation in frequency independent dielectric grating," in *Vacuum Electronics Conference (IVEC), 2012 IEEE Thirteenth International*, 2012, pp. 157-158.
 19. **Ohjoon Kwon**, *et al.*, "Sheet Beam Wideband Terahertz Extended Interaction Oscillator using Phase shifted Coupling with Staggered Periodicity", in *Vacuum Electronics Conference (IVEC), 2012 IEEE Thirteenth International*, 2012
 20. S. H. Min, **O. J. Kwon**, M. A. Sattorov, J. K. Soc, I. K. Baek, S. T. Kim, K. H. Eom, A. Bera, R. K. Barik, Y. M. Shin and G. S. Park, "Studies on High Power THz Radiation using Nanosecond Pulse in Oversized Relativistic Backward Wave Oscillator", IEEE IVEC-IVESC 2012
 21. A. Bera, R. K. Barik, S. H. Min, **O. J. Kwon**, I. K. Baek, S. Kim, *et al.*, "Generation

- of THz radiation: Metallic metamaterial grating versus lamellar grating," in *Infrared, Millimeter, and Terahertz Waves (IRMMW-THz), 2012 37th International Conference on*, 2012
22. A. Bera, M. A. Sattorov, **O. J. Kwon**, R. K. Barik, S.-H. Min, G.-S. Park, "Smith-Purcell radiation from metallic metamaterial grating." in *Proc. 3rd Int. THz-Bio Workshop*, Feb. 8-9, 2012, SNU, Seoul, Korea, p. P-1.
 23. R. K. Barik, A. K. Tanwar, I. K. Baek, K. Eom, A. Bera, M. A. Sattorov, S.-H. Min, **O. J. Kwon**, G.-S. Park, "Development of high current density scandate cathode for terahertz vacuum devices application." in *Proc. 3rd Int. THz-Bio Workshop*, Feb. 8-9, 2012, SNU, Seoul, Korea, p. P-2.
 24. M. A. Sattorov, E. Khutoryan, K. Lukin, G.-S. Park, A. Bera, R. Barik, **O.-J. Kwon**, S.-H. Min, A. Sharma, A. Tanwar, "Experimental analysis on 0.1 THz clinotron." in *Proc. 3rd Int. THz-Bio Workshop*, Feb. 8-9, 2012, SNU, Seoul, Korea, p. P-3.
 25. M. A. Sattorov, E. Khutoryan, K. Lukin, G.-S. Park, A. Bera, R. Barik, **O.-J. Kwon**, S.-H. Min, A. Sharma, A. Tanwar, "Automodulation processes in BWO with inclined electron beam at low focusing magnetic fields." in *Proc. 3rd Int. THz-Bio Workshop*, Feb. 8-9, 2012, SNU, Seoul, Korea, p. P-4.
 26. **O. Kwon**, J.-K. So, M. Sattorov, R. K. Barik, A. Bera, A. K. Tanwar, I.-K. Baek, S.-H. Min, J.-H. Kim, S.-S. Chang, G.-S. Park, "Microfabricated sub-terahertz vacuum electronic devices." in *Proc. 3rd Int. THz-Bio Workshop*, Feb. 8-9, 2012, SNU, Seoul, Korea, p. P-5.
 27. S.-H. Min, **O. Kwon**, M. Sattorov, I. K. Baek, K.-H. Eom, H. Son, D.-H. Choi, S.-H. Bak, S. Kim, A. Bera, R. Barik, K.-T. Kim, G.-H. Park, W.-Y. Park, J.-Y. Lee, S.-J. Cho, O. S. Kwon, G.-S. Park, "Biological effects by AC ns pulsed electromagnetic fields (EMF) at cm & mm waves exposures and DC ns pulsed electric fields (nsPEF)." in *Proc. 3rd Int. THz-Bio Workshop*, Feb. 8-9, 2012, SNU, Seoul, Korea, p. P-25.
 28. **O. Kwon**, S. H. Pak, J. K. So, I. K. Baik, S. H. Min, and G. Park, "Experimental confirmation of Bethe's diffraction theory," in *Infrared, Millimeter and Terahertz Waves (IRMMW-THz), 2011 36th International Conference on*, 2011
 29. R. K. Barik, A. K. Tanwar, A. Bera, **K. Ohjoon**, M. A. Sattorov, and G. S. Park, "Investigation of emission mechanism of scandium doped nano particle dispenser cathode for THz vacuum electron devices," in *Infrared, Millimeter and Terahertz Waves (IRMMW-THz), 2011 36th International Conference on*, 2011
 30. S. H. Min, **O. J. Kwon**, M. A. Sattorov, J. K. So, S. H. Park, I. K. Baek, *et al.*,

- "Studies on high power THz radiation using nanosecond pulse in oversized Relativistic Backward Wave Oscillator," in *Infrared, Millimeter and Terahertz Waves (IRMMW-THz), 2011 36th International Conference on*, 2011
31. A. Srivastava, **K. Oh-joon**, A. Bera, B. In-Keun, and P. Gun-Sik, "Dielectric measurement of low loss-tangent dielectric near 100 GHz by a simplified hemispherical open resonator technique," in *Infrared Millimeter and Terahertz Waves (IRMMW-THz), 2010 35th International Conference on*, 2010
 32. A. Bera, **K. Ohjoon**, R. K. Barik, A. Tanwar, M. A. Sattorov, and P. Gun-Sik, "Design of depressed collector for 94 GHz CCBWO," in *Vacuum Electronics Conference (IVEC), 2011 IEEE International*, 2011, pp. 135-136.
 33. G. S. Park, S. H. Min, M. A. Sattorov, **O. J. Kwon**, R. K. Barik, A. Bera. "High power terahertz activities at SNU", 8th International Workshop. Strong microwave and terahertz waves: sources and applications. Nizhniy Novgorod, Russia, 2011 R. K. Barik, A. K. Tanwar, A. Bera, **O. Kwon**, M. A. Sattorov, G.-S. Park, "High current density nano-particle dispenser cathode for THz vacuum electron devices." in *Proc. 2nd Int. THz-Bio Workshop*, Jan. 19-20, 2011, SNU, Seoul, Korea, p. 47 (P-1).
 34. A. Bera, **O. Kwon**, R. K. Barik, M. A. Sattorov, G.-S. Park, "Thermal issues in THz vacuum electron devices." in *Proc. 2nd Int. THz-Bio Workshop*, Jan. 19-20, 2011, SNU, Seoul, Korea, p. 48 (P-2).
 35. M. A. Sattorov, A. Bera, R. K. Barik, **O. Kwon**, G.-S. Park, K. A. Lukin, A. S. Tishchenko, "Thermal velocity effects in sheet-beam for THz devices." in *Proc. 2nd Int. THz-Bio Workshop*, Jan. 19-20, 2011, SNU, Seoul, Korea, p. 52 (P-5).
 36. **O. Kwon**, J.-K. So, M. Sattorov, R. K. Barik, A. Bera, A. K. Tanwar, S.-H. Park, I.-K. Baek, J.-H. Kim, S.-S. Chang, G.-S. Park, "CW/pulsed sub-THz wave system for biomedical applications." in *Proc. 2nd Int. THz-Bio Workshop*, Jan. 19-20, 2011, SNU, Seoul, Korea, p. 59 (P-9).
 37. S.-H. Min, M. Sattorov, J.-K. So, **O. Kwon**, S.-H. Park, D.-H. Choi, S.-Y. Yun, S.-J. Cho, O.-S. Kwon, K.-T. Kim, Y.-Y. Park, H.-J. Kee, G.-S. Park, "GW-ns millimeter-wave relativistic backward oscillator (RBWO) for biomedical applications." in *Proc. 2nd Int. THz-Bio Workshop*, Jan. 19-20, 2011, SNU, Seoul, Korea, p. 70 (P-16).
 38. **K. Ohjoon**, S. Jin-Kyu, A. Srivastava, M. Sattorov, R. K. Barik, A. Bera, *et al.*, "Micro-fabricated millimeter wave vacuum electronic devices," in *Infrared Millimeter and Terahertz Waves (IRMMW-THz), 2010 35th International Conference on*, 2010
 39. M. Sattorov, J. K. So, S. H. Park, **O. J. Kwon**, A. Srivastava, G. S. Park, K. A. Lukin,

- M. V. Mil'cho, J.Y. Kim, J.W. Yang, J.H. Choi, "Particle-in-cell simulation of 0.3 THz Clinotron", in *Infrared Millimeter and Terahertz Waves (IRMMW-THz), 2010 35th International Conference on*, 2010
40. A. Srivastava, **K. Oh-joon**, M. Sattorov, A. Sharma, A. Tanwar, and P. Gun-Sik, "Broadband THz vacuum window using impedance matching approach," in *Infrared Millimeter and Terahertz Waves (IRMMW-THz), 2010 35th International Conference on*, 2010
 41. J. S. Kyoung, M. A. Seo, H. R. Park, **O. Kwon**, G. S. Park, O. K. Suwal, *et al.*, "Terahertz transmission through nanogaps using both pulsed and CW sources," in *Infrared, Millimeter, and Terahertz Waves, 2009. IRMMW-THz 2009. 34th International Conference on*, 2009
 42. A. Srivastava, J. K. So, M. A. Sattorov, **O. J. Kwon**, G. S. Park, C. W. Baik, *et al.*, "100GHz LIGA-fabricated coupled-cavity device," in *Vacuum Electronics Conference, 2009. IVEC '09. IEEE International*, 2009, pp. 102-103.
 43. A. Srivastava, J. K. So, K. H. Jang, **O. J. Kwon**, M. A. Sattorov, C. W. Baik, J. H. Kim, S. S. Chang, and G.-S. Park, "0.1 THz microfabricated dual-inline grating like coupled-cavity device." in *Proc. 34th Int. Conf. IRMMW-THz*, Busan, Korea, Sep. 21-25, 2009.
 44. **K. Oh-joon**, K. Dae-won, K. Hee-yeon, W. Jong-hyo, J. Young-do, K. Yong-Hyup, *et al.*, "CW Terahertz imaging of paraffin-embedded epithelia cell of rat," in *Vacuum Electronics Conference, 2008. IVEC 2008. IEEE International*, 2008, pp. 386-387.
 45. **O. Kwon**, Y. D. Joo, H. J. Choi, D. S. Kim, Y. H. Kim, J. I. Kim, *et al.*, "Terahertz imaging of paraffin-embedded epithelial cell of rat using pulsed and CW THz systems," in *Infrared, Millimeter and Terahertz Waves, 2008. IRMMW-THz 2008. 33rd International Conference on*, 2008
 46. S. J. Chang, S. M. Ahn, **O. J. Kwon**, M. A. Seo, D. S. Kim, W. H. Jhe, *et al.*, "Studies on interfacial water adsorbed on mica at room temperature using terahertz spectroscopy," in *Infrared, Millimeter and Terahertz Waves, 2008. IRMMW-THz 2008. 33rd International Conference on*, 2008

Domestic Conference proceedings and abstracts (13)

1. 민선홍 (발표자), 권오준, 백인근, 김선태, 박건식, 이상훈, 윤영준, 이우상, 이민우, 소준호, "Effectiveness analysis experiments for electromagnetic coupled electronics by mode-converted relativistic backward wave oscillator" 제 4 회 고에너지.국방소재 학술대회 - 03 고에너지 EMP 분과, November 11 (2014)
2. G.-S. Park, on behalf of lab. Team (M. A. Sattorov, A. Bera, R. K. Barik, H. S. Yoon, O. J. Kwon, S. H. Min) "Design of the SSR2 and RF power coupler", *RISP Workshop*, Daejeon, Korea, May 19-21, 2013.
3. BAEK IN-KEUN, EOM KIHOOON, KIM SEONTAE, KWON OHJOON, PARK GUN-SIK, "Sub-THz Reflectometry: Possible Analyzing Tool for Skin Conditions" The Korean Physical Society, October 24-26 (2012)
4. 김 선태, 권 오준, 백 인근, 엄기훈, 민 선홍, BERA ANIRBAN, "Bending transmission of human hair at terahertz frequency regime" The Korean Physical Society, October 24-26 (2012)
5. KIM tae young, 권 오준, 박 건식, "Wide bandwidth of RF window for W-band vacuum electronic devices" The Korean Physical Society, October 24-26 (2012)
6. BAEK In Keun, KWON Ohjoon, KIM Seontae, EOM Kihoon, PARK Gun-Sik, "Does Helically Shaped Sweat Ducts Act as Array of Low-Q Antenna?" The Korean Physical Society, April 25-27 (2012)
7. KIM Seontae, KWON Oh-Joon, BAEK In-Keun, EOM Ki-Hoon, BERA Anirban, MIN Sun-Hong, PARK Gun-Sik, "A Simulation Study Of Hair-guided Terahertz Wave Propagation" The Korean Physical Society, April 25-27 (2012)
8. 권오준, 박승호, 서민아, 박건식, 김대식, "Transmission of Terahertz Wave Through a Single Subwavelength Circular Hole", The Korean Physical Society, April 23-24 (2009)
9. O. Kwon, D.W. Kim, H.Y. Kim, J.H. Won, Y.D. Joo, Y.H. Kim, D.S. Kim and G. S. Park, "CW Terahertz Imaging of Paraffin-embedded Epithelial Cell of Rat", The Korean Physical Society, Apr 17-28 (2008)
10. O. Kwon, Y.D. Joo, H.J. Choi, D.S. Kim, Y.H. Kim, J.I. Kim, S.G. Jeon, Y.S. Jin and G.S. Park, "Terahertz Imaging of Paraffin-embedded Epithelial Cell of Rat using Pulsed and CW THz Systems", 3rd Asian Summer School on Laser-Plasma Acceleration, July 21-25 (2008)

11. **O. Kwon**, S.H. Park, M.A. Seo, D.S. Kim and G. S. Park, "Transmission of Terahertz Wave Through a Single Subwavelength Circular Hole", The Korean Physical Society, Oct 23-24 (2008)
12. **O. J. Kwon**, D. W. Kim, H.Y. Kim, J.H. Won, Y.D. Joo and G.S Park, "CW Imaging using Terahertz radiation Source", KPS, October 18-19 (2007)
13. Jong-Hyo Won, **Oh-Jun Kwon**, and Gun-Sik Park, "Effect of Multiple Antenna on Operation of High-Power Magnetron", KPS, October 18-19 (2007)
14. Gun-sik Park, Jin-Kyu So, Kyu-ha Jang, Jong-Hyo Won, Hoi-Chun Jung, Anurag Srivastava, Sun-Hong Min, Matlabjohn Sattarov, Sang-ho Shin, **Ojun Kwon**, Ravinder Chutani, Zhenhwa Wu, Seung-ho Park and Young-Do Joo, "Compact High-Power CW THz Radiation Sources using Vacuum Electron Beam", The 3rd Workshop on THz Technology, November 2 (2007)

국문 초록

생물, 의약 분야, 재료, 통신, 보안, 고용량 데이터 전송 등 테라헤르츠파는 수많은 연구 영역에서 그 가치를 인정받고 빠른 속도로 해당 기술과 과학이 발전하고 있다. 테라헤르츠 발생원에 대해서 많은 연구가 진행되고 있는데, 강력한 대류전자를 에너지원으로 사용하는 진공 전자 장치 분야에서도 최근의 발전된 미세가공 기술을 기반으로 하여 초소형 진공 전자 장치가 구현 가능해지고 새로운 더욱 강력한 전자빔과 회로간의 상호작용이 알려지고 있는 바 고출력임과 동시에 지속적으로 방사 가능한 테라헤르츠 진공 전자 장치의 개발에 학계의 이목이 주목되고 있다.

본 논문에서는 이런 요구를 충족시킬 수 있는 방안으로서 0.1 테라헤르츠에 동작하는 연속 공동 후진파 발생장치를 제안하였다. 정밀한 작업이 요구되는 회로를 2 단계 리가 공정과 초고정밀 컴퓨터 기계 가공을 통해 1 마이크로미터 미만의 공차범위에서 제작하였고, 콜드 실험을 통해 그 성능이 유한차분 시간 영역법을 통해 계산된 결과와 완벽히 일치되었음을 보였다. 이 논문에서는 회로만이 아니라 0.1 테라헤르츠 연속 공동 후진파 발생장치의 모든 다른 부품들, 즉, 12 킬로볼트, 50 밀리암페어의 전자총, 2800 가우스의 자기장을 전자빔에 지속적으로 걸어주는 주기적 영구자석 장치, -9 킬로볼트 전자빔 완화 집적 장치, 중심 주파수 대비 8 퍼센트의 주파수 폭으로

전자기파를 투과하는 진공 윈도우 등을 모두 설계, 제작, 및 실험을 통해 그 결과들이 모두 설계와 일치함을 보였다. 거기에 더해서 모든 부품들을 적합한 공정으로 조립하여 하나의 완성된 장치를 만들고, 전자총에 전압을 걸어 초기 전압, 전류를 측정하였고, 전자빔 집적 전극에 추가적인 바이어스 전압을 3 볼트 걸었을 때 설계값과 동일한 퍼비언스 값을 얻어냈다.

미세 공정 보다 전자빔과 회로간의 상호작용에 초점을 맞춘 0.22 테라헤르츠 엇갈린 확장형 상호작용 발생원에 대한 연구도 제안했다. 상대적으로 낮은 전압으로 작동가능한 이 장치는 마주보는 직사각형 격자 구조를 서로 반 주기 엇갈리게 하여, 회로의 기본모드인 TE₁₀ 모드가 빔 진행방향으로 편광되어 격자구조 상에서 강력한 플라즈마 테라헤르츠 상호작용을 일으킴으로서 높은 효율의 테라헤르츠가 상대적으로 낮은 전자빔 에너지에서도 발생이 가능하게 설계되었다. PIC 전산모사를 통해 설계된 회로가 0.22 테라헤르츠에서 동작하며, 전자빔 전압 5.2 킬로볼트일 때 15 퍼센트 이상이 효율로 100 와트를 상회하는 출력을 내는 것을 확인했다.

학번: 2008-30116